

**RESEARCH ARTICLE**

WILEY

Activity of the south Tibetan detachment system: Constraints from leucogranite ages in the eastern Himalayas

Lin-Kui Zhang^{1,2} | Guang-Ming Li² | Hua-Wen Cao² | Zhi Zhang² |
 Sui-Liang Dong² | Wei Liang² | Jian-Gang Fu² | Yong Huang² |
 Xiang-Biao Xia² | Zuo-Wen Dai² | Qiu-Ming Pei³ | Shou-Ting Zhang¹

¹School of Earth Sciences and Resources, China University of Geosciences, Beijing, China

²Chengdu Center, China Geological Survey, Chengdu, China

³Faculty of Geosciences and Environmental Engineering, Southwest Jiaotong University, Chengdu, China

Correspondence

Hua-Wen Cao, Chengdu Center, China Geological Survey, Chengdu, China.
 Email: caohuawen1988@126.com

Funding information

National Key R&D Program of China, Grant/Award Numbers: 2018YFC0604103, 2016YFC0600308; National Natural Science Foundation of China, Grant/Award Numbers: 41802095, 91955208; China Geological Survey, Grant/Award Number: DD20190147

Peer Review

The peer review history for this article is available at <https://publons.com/publon/10.1002/gj.3756>.

Handling Editor: M. Santosh

Himalayan leucogranites are widely distributed in the North Himalayan gneiss dome (NHGD) and at the top of the Greater Himalayan Crystalline Complex (GHC) and are generally controlled by detachment faults. The ages of these prekinematic, synkinematic, and postkinematic leucogranites can be used to limit the activity of detachment structures (such as the South Tibetan Detachment System, STDS). Research on the STDS activity time in the eastern Himalayas is relatively sparse. In this study, the zircon and monazite U–Th–Pb geochronology of synkinematic and postkinematic leucogranites, which are affected by the STDS and NHGD, in four areas (Lhozhag, Kuju, Xiaozhan, and Cuonadong) in Shannan City, Tibet, China, was measured. The results show that the oldest synkinematic two-mica granite from Lhozhag, which is affected by the STDS, is 24–25 Ma, so the time of STDS activity is at or slightly earlier than 25 Ma. The youngest synkinematic leucogranite is the garnet-bearing muscovite granite in Cuonadong at 18.4 Ma. The oldest undeformed postkinematic leucogranite (not affected by the STDS) is the muscovite granite in Xiaozhan at 17.4 Ma. Therefore, the end of STDS activity can be limited to 18.4–17.4 Ma. The STDS includes three forms: detachment fault in the NHGD (northern extension of the STDS), the inner STDS between the GHC and Tethyan Himalayan Sequence, and the outer STDS at the bottoms of synformal klippen. In this paper, the active time limits of the above three kinds of detachment zones are comprehensively summarized. Based on this work, the northward extension (ductile deformation) time of the STDS in the region is considered to be 28–17 Ma. The exhumation of the GHC is mainly controlled by in-sequence shearing: first, the South Tibet Thrust system (predecessor of the STDS) at the top of the GHC thrust southward at 45–28 Ma, then the High Himalayan Discontinuity fault in the middle of the GHC forms south-vergent ductile thrusts at 28–17 Ma, and finally, the Main Central Thrust at the bottom of the GHC thrust southward at 17–9 Ma.

KEYWORDS

eastern Himalaya, exhumation of Greater Himalayan Crystalline Complex, in-sequence thrust, South Tibetan Detachment System, zircon and monazite U–Pb dating

1 | INTRODUCTION

The South Tibetan Detachment System (STDS) can be divided into a detachment fault in the North Himalayan Gneiss Dome (NHGD; northern continuation of the STDS; Larson, Godin, Davis, & Davis, 2010), an inner STDS or the *strict sense* STDS (between the Greater Himalaya Crystalline Complex [GHC] and Tethyan Himalayan Sequence [THS]; Burchfiel et al., 1992), and an outer STDS (at the base of a synformal klippe; Kellett, Grujic, & Erdmann, 2009) in a broad sense. Himalayan leucogranites are widely distributed in the interior of the NHGD and at the top of the GHC (Guo & Wilson, 2012), controlled by the extensional detachment fault at the edge of the dome (Jessup, Langille, Diedesch, & Cottle, 2019) and the STDS at the bottom of the THS (Kellett, Cottle, & Larson, 2019), respectively. The crystallization ages of prekinematic (cut by the STDS), synkinematic (sheared parallel to the STDS fabrics), and postkinematic (cut across the STDS) leucogranites can be used to limit the activities of these detachment faults (STDS; Leloup et al., 2010; Searle, 2013; Weinberg, 2016; Iaccarino et al., 2017; Liu et al., 2017; Goscombe, Gray, & Foster, 2018; Spencer et al., 2019; Spencer, Kirkland, Prave, Strachan, & Pease, 2019; Spencer, Kirkland, Roberts, Evans, & Liebmann, 2020; Ji et al., 2020). The time of STDS activity is one of the important factors to resolve the Himalayan orogenic process (Burchfiel et al., 1992), especially the exhumation and denudation model for the GHC and the dome-forming model (Chambers, Parrish,

Argles, Harris, & Horstwood, 2011; Godin, Grujic, Law, & Searle, 2006; Webb et al., 2017).

The ages of foliated synkinematic leucogranite sills in the shear zone are equivalent to the STDS activity age, and undeformed postkinematic leucogranites can limit the latest time of ductile shear (Wang et al., 2016). Therefore, the dating of deformed and undeformed leucogranites is one of the important ways to study the Himalayan orogenic process (Goscombe et al., 2018; Harris & Massey, 1994). Compared with the Middle and Western Himalaya, the Eastern Himalaya (east of 89°E) has received lesser attention, especially in China's Tsona County, where previous studies on the STDS are almost non-existent (Yin & Harrison, 2000). Based on a regional geological survey at a scale of 1:50,000, nine synkinematic and postkinematic leucogranites in four regions (Lhozhaq [LZ], Kuju [KJ], Xiaozhan [XZ], and Cuonadong [CND]) affected by the STDS were collected in this study. Seven zircon U-Pb and six monazite U-Th-Pb geochronologies were tested to determine the ages of the leucogranites and to ultimately define the active time of north-south extension (STDS). This paper summarizes the previous results for the above three parts of the STDS in the Himalayas in detail. On this basis, it is believed that there were two stages of STDS activity in the Himalayas. In the early stage (45–28 Ma), south-vergent thrusting of the STDS (a predecessor of the STDS, namely, the South Tibet Thrust System) occurred, and in the late stage (28–17 Ma), the northward extension of the STDS occurred.

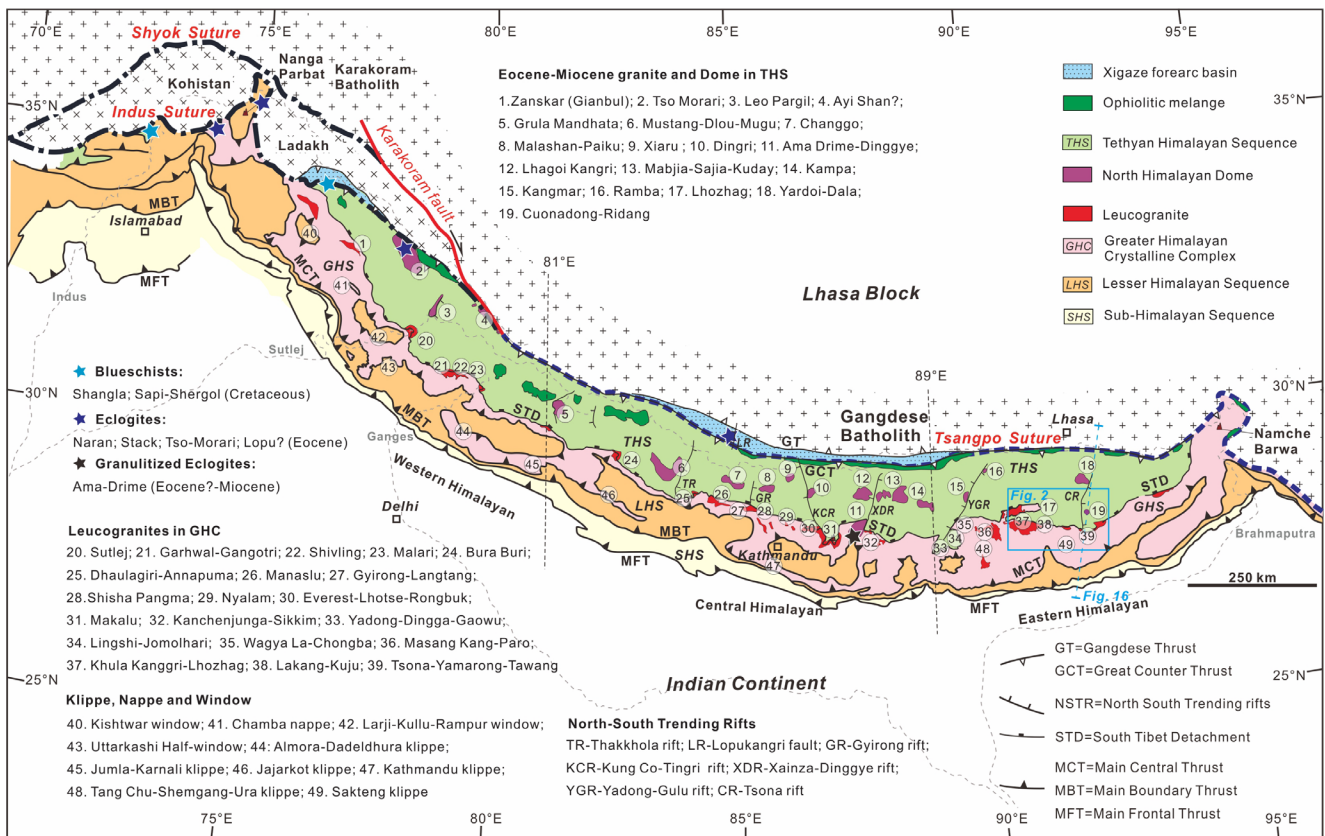


FIGURE 1 Sketch map of the Himalayan orogenic belt showing the distribution of Leucogranite, gneiss domes, and South Tibetan Detachment System (Burg & Bouilhol, 2019) [Color figure can be viewed at wileyonlinelibrary.com]

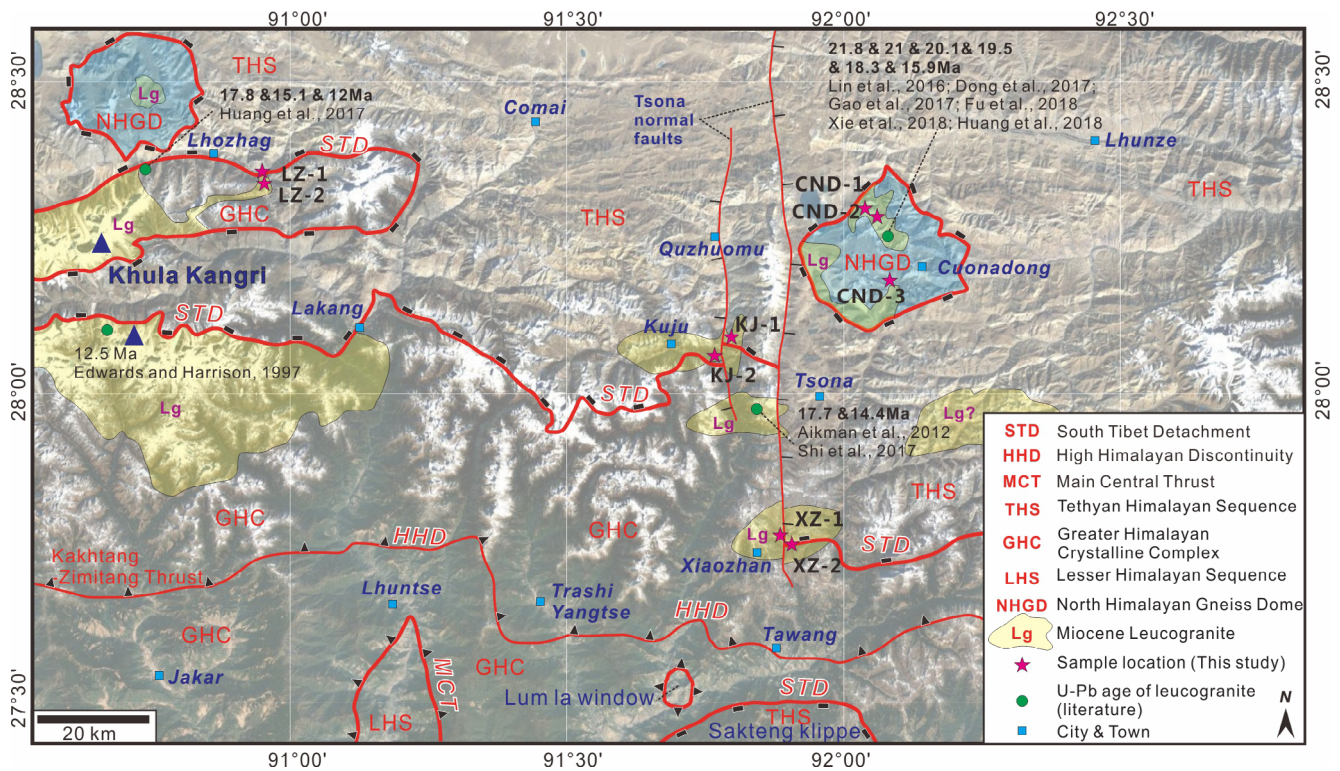


FIGURE 2 Geological sketch showing the South Tibetan Detachment System in Lhozhag (LZ), Kuju (KJ), Xiaozhan (XZ), and Cuonadong dome (CND). Remote sensing satellite map revised from Google Earth. The age of the leucogranites from Huang et al. (2017), Edwards and Harrison et al. (1997), Aikman et al. (2012), Wang et al. (2016), Shi et al. (2017), Lin et al. (2016), Dong et al. (2017), Gao et al. (2017), Fu et al. (2018), Xie et al. (2018), and Huang et al. (2018) [Color figure can be viewed at wileyonlinelibrary.com]

2 | REGIONAL GEOLOGICAL SETTING

The Himalayan orogenic belt belongs to the southernmost part of the Qinghai–Tibetan Plateau, with an east–west length of more than 2,000 km. This belt is the result of collision between the Indian Plate and the Eurasian Plate since the Cenozoic (Cao et al., 2019; Zhang et al., 2020). Its south side is limited by the Main Boundary Thrust Fault, and its north side is confined by the Indus–Yarlung Zangbo River suture zone (IYZS) and Gangdese magmatic rock (Lhasa Block). From south to north in Himalaya, it consists of four tectonic units, namely, the sub-Himalaya, Lesser Himalaya (LHS), GHC, and THS. The THS is clamped by the IYZS to the north and the STDS to the south (Figure 1).

The THS is mainly composed of Palaeozoic–Mesozoic–Eocene shallow metamorphosed marine sediments and Oligocene continental sediments, among which the Triassic, Jurassic, and Cretaceous sedimentary rocks are the best developed, and the main lithologies are sandstone, siltstone, limestone, and shale (Cao et al., 2018). During the collision of India and Asia, the crust of the Tethyan Himalaya was compressed and thickened, forming the Tethyan Himalayan fault-fold belt.

Early Cretaceous (135–130 Ma) bimodal magmatic rocks (Huang et al., 2019) are widely developed in the Tethyan Himalaya and are called the Cuomei igneous province. The lithologies mainly include diabase and gabbro intrusive bodies and acid extrusive rock, which

represent the separation of the Indian landmass from Gondwana and its northward drift.

The beaded NHGD, which is parallel to the orogenic belt, is a typical feature of the Tethyan Himalayan orogenic belt. Early to middle Palaeozoic (530–470 Ma) granitic gneisses (orthogneiss) developed in the core of NHGD (Gao et al., 2019; Zhang et al., 2019), and Eocene to Miocene (44–7 Ma) highly fractionated leucogranites intruded them (Dai et al., 2020).

A large number of Pb–Zn, Sb–Pb–Zn, Au, and Au–Sb deposits have developed in the Tethyan Himalaya belt, which is called the Tethyan-Himalayan Sb–Au–Pb–Zn polymetallic metallogenic belt. Its spatial distribution is mainly controlled by the STDS, north–south-trending rifts (NSTR) and the dome structure. However, the latest research and geological surveys show that the Tethyan-Himalayan region is not only an antimony–gold–lead–zinc metallogenic area (Cao et al., 2019) but also an important Sn–W rare metal enrichment area (Cao et al., 2020 submitted).

The STDS is the largest normal fault system in the world (Burchfiel et al., 1992). In this fault system, the low-grade metamorphosed THS (slate, phyllite, etc.) is directly superposed on the high-grade metamorphosed GHC (kyanite and sillimanite phase metamorphism) thus forming one of the most important geological boundaries of the Himalayan orogenic belt. Kinematically, the upper side of the STDS slides northward relative to the lower side. In terms of structural assemblage, most studies suggest that the STDS is composed of

two parts: the mylonitized ductile shear zone at the bottom and the brittle normal fault at the top. The STDS is a ductile shear zone with a width of several kilometres. The shear zone is mainly composed of mylonite gneiss, schist, and deformed leucogranite sills and is intruded by undeformed leucogranite dykes.

A large number of leucogranites intruded during the northward extension ductile shear activity of the STDS and after the end of STDS activity, producing deformed and undeformed leucogranites, respectively. By dating these deformed (synkinematic) and undeformed (postkinematic) leucogranites, it can be inferred that (a) the latest time of STDS activity (the time of extensional activity) is equivalent to or slightly earlier than that of strongly deformed synkinematic granites and (b) the final time of STDS activity (the age of ductile shear) is earlier than that of undeformed postkinematic granites.

3 | SAMPLES AND ANALYTICAL METHODS

3.1 | Samples

In this study, nine synkinematic and postkinematic leucogranites (Figure 2, Table 1) in four areas (LZ, KJ, XZ, and CND) affected by the STDS and dome structures were collected.

Two kinds of leucogranite have mainly developed in the eastern LZ County: One kind is deformed leucogranite (LZ-1; Figure 3a), which is deformed along schist foliation and has obvious distortion and ductile deformation; the other kind is undeformed muscovite leucogranite (LZ-2; Figure 3c), which is in intrusive contact with metamorphic rocks. The microscopic characteristics of the two kinds of leucogranite are consistent with those observed in the field. The deformed leucogranite was distorted together with the schist and developed obviously recrystallized quartz, and biotite and muscovite are in directional arrangement (Figure 3b). Under the microscope, the mineral deformation characteristics of undeformed muscovite leucogranite are not obvious (Figure 3d).

Leucogranites are also widely developed in KJ village in eastern LZ County. Consistent with the above rocks, one kind is lenticular garnet-bearing, tourmaline-muscovite granite, and granite pegmatite (KJ-1) and deformed along with schist (Figure 4a), and the other kind is leucogranite (KJ-2) without ductile deformation (Figure 4c).

The STDS extends from west to east and is dislocated by the Tsona rift (NSTR) east of KJ village. The STDS is exposed in the XZ area southeast of KJ village (Figure 2). A large number of leucogranites have developed in the XZ area; one kind is tourmaline two-mica granite (XZ-1) strongly deformed along with schist (Figure 5a), while the other kind is muscovite granite (XZ-2) lacking ductile deformation and having intrusive contacts with metamorphic rocks (Figure 5b).

TABLE 1 Summary of the lithology, sample location, zircon, and monazite ages of leucogranites from Lhozgag, Kuju, Xiaozhan, and Cuonadong

Number	Location	Sample no.	Occurrence	Lithology	GPS position	Zircon age (2σ) ^a	Monazite age (2σ) ^b
1	Lhozgag	LZ-1	Deformed dyke	Two-mica granite	E 90°54'47.75", N 28°22'04.44"	24.6 ± 0.2 Ma (n = 13, MSWD = 0.9)	24.4 ± 0.1 Ma (n = 11, MSWD = 1)
2		LZ-2	Undeformed dyke	Garnet-bearing muscovite granite	E 90°54'47.31", N 28°22'01.59"	13.6 ± 0.1 Ma (n = 14, MSWD = 1.4)	13.6 ± 0.1 Ma (n = 14, MSWD = 0.3)
3	Kuju	KJ-1	Deformed boudin	Muscovite granite	E 91°48'22.85", N 28°05'05.54"	23.4 ± 0.2 Ma (n = 14, MSWD = 1.9)	23.9 ± 0.1 Ma (n = 31, MSWD = 1.9)
4		KJ-2	Undeformed main body	Tourmaline-bearing muscovite granite	E 91°48'15.35", N 28°03'36.05"	16.5 ± 0.1 Ma (n = 12, MSWD = 1.5)	16.9 ± 0.1 Ma (n = 27, MSWD = 0.6)
5	Xiaozhan	XZ-1	Deformed boudin	Tourmaline two-mica granite	E 91°50'17.42", N 27°48'25.01"		20 ± 0.1 Ma (n = 11, MSWD = 1.4)
6		XZ-2	Undeformed dyke	Muscovite granite	E 91°50'48.93", N 27°48'26.18"		17.4 ± 0.1 Ma (n = 16, MSWD = 2.3)
7	Cuonadong	CND-1	Deformed boudin	Garnet-bearing two- mica granite	E 91°59'57.16", N 28°14'35.35"	23.7 ± 0.2 Ma (n = 20, MSWD = 1.3)	
8		CND-2	Deformed boudin	Garnet-bearing muscovite granite	E 92°03'06.57", N 28°15'18.22"	18.4 ± 0.1 Ma (n = 20, MSWD = 2)	
9		CND-3	Undeformed main body	Garnet-bearing muscovite granite	E 92°04'42.05", N 28°11'25.17"	16.8 ± 0.2 Ma (n = 9, MSWD = 0.6)	

^aWeighted average age of zircon ²⁰⁶Pb/²³⁸U date.

^bWeighted average age of monazite ²⁰⁸Pb/²³²Th date.

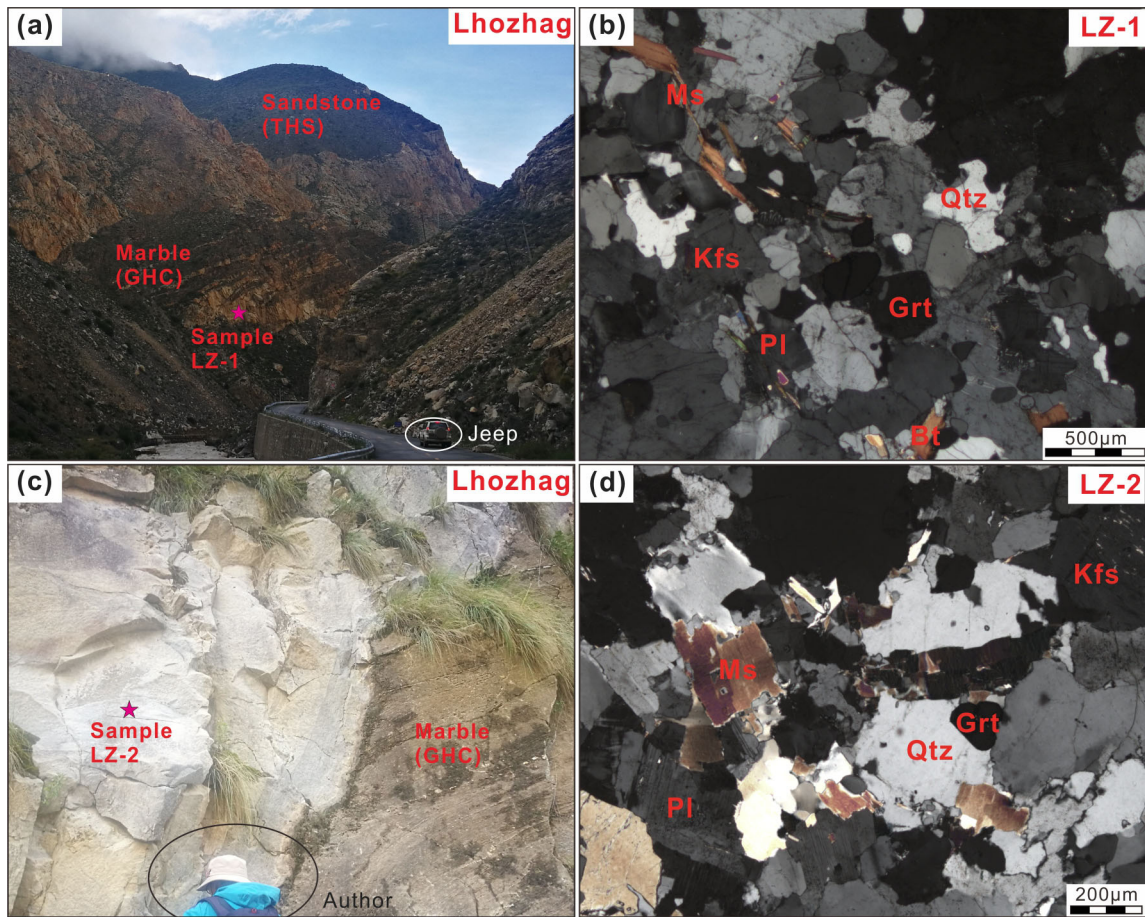


FIGURE 3 (a and b) Photographs showing the geology and mineralogical features of the deformed leucogranites (sample LZ-1) from Lhozhag. (c and d) showing the geology and mineralogical features of the undeformed leucogranites (sample LZ-2) from Lhozhag. Bt-biotite, Grt-garnet, Kfs-potassium feldspar, Ms-muscovite, Pl-plagioclase, and Qtz-quartz, Tur-tourmaline [Color figure can be viewed at wileyonlinelibrary.com]

In addition, the undeformed garnet-bearing muscovite granite was cut by NSTR in the later stage due to the action of the Tsona rift fracture, resulting in brittle deformation (Figure 5b).

The CND dome is a dome newly discovered by the authors in recent years, which is consistent with the structural characteristics of the NHGD. The CND dome mainly consists of three parts from exterior to interior: (a) Rim: Mesozoic low-grade sediments, (b) Mantle: Palaeozoic high-grade schist, marble, and Miocene leucogranite sills, and (c) Core: Miocene leucogranite and Cambrian orthogneiss. These three parts are separated by an upper brittle detachment fault and a lower ductile detachment fault. The lower ductile detachment fault of the CND dome is consistent with the STDS and belongs to the northern extension of the STDS. The movement of the lower detachment fault of the CND dome resulted in the intense deformation of leucogranite within the mantle (shear zone) of the dome, forming lenticular or σ -shaped structures (Figure 6a,c). In addition, a set of post dome granites (Figure 6e) has developed in the core of the dome, which is not deformed or affected by the activity of the detachment fault. The strongly deformed leucogranites are mainly a set of garnet-bearing two-mica granite (CND-1) and garnet-bearing muscovite

granite (CND-2). It is found that quartz has undulose extinction and recrystallized vermicular structure (Figure 6b,d). The undeformed leucogranites (CND-3) are mainly a set of muscovite granite (Figure 6f) with a small amount of tourmaline, and the features of its deformation or recrystallization are not obvious under the microscope.

3.2 | Laser ablation–inductively coupled plasma–mass spectrometry zircon and monazite U–Pb dating

Conventional electromagnetic and heavy fluid separation methods were used to separate zircon and monazite grains from the nine leucogranites. Selected zircon and monazite grains were mounted on epoxy resin, polished to expose the grains, and photographed under transmitted and reflected light, followed by cathodoluminescence (CL) and backscattered electron imaging.

U–Pb dating and trace element analysis of zircon and monazite were conducted by laser ablation–inductively coupled plasma–mass spectrometry (LA–ICP–MS) at the Wuhan Sample Solution Analytical Technology Co., Ltd., Wuhan, China. Detailed operating conditions for

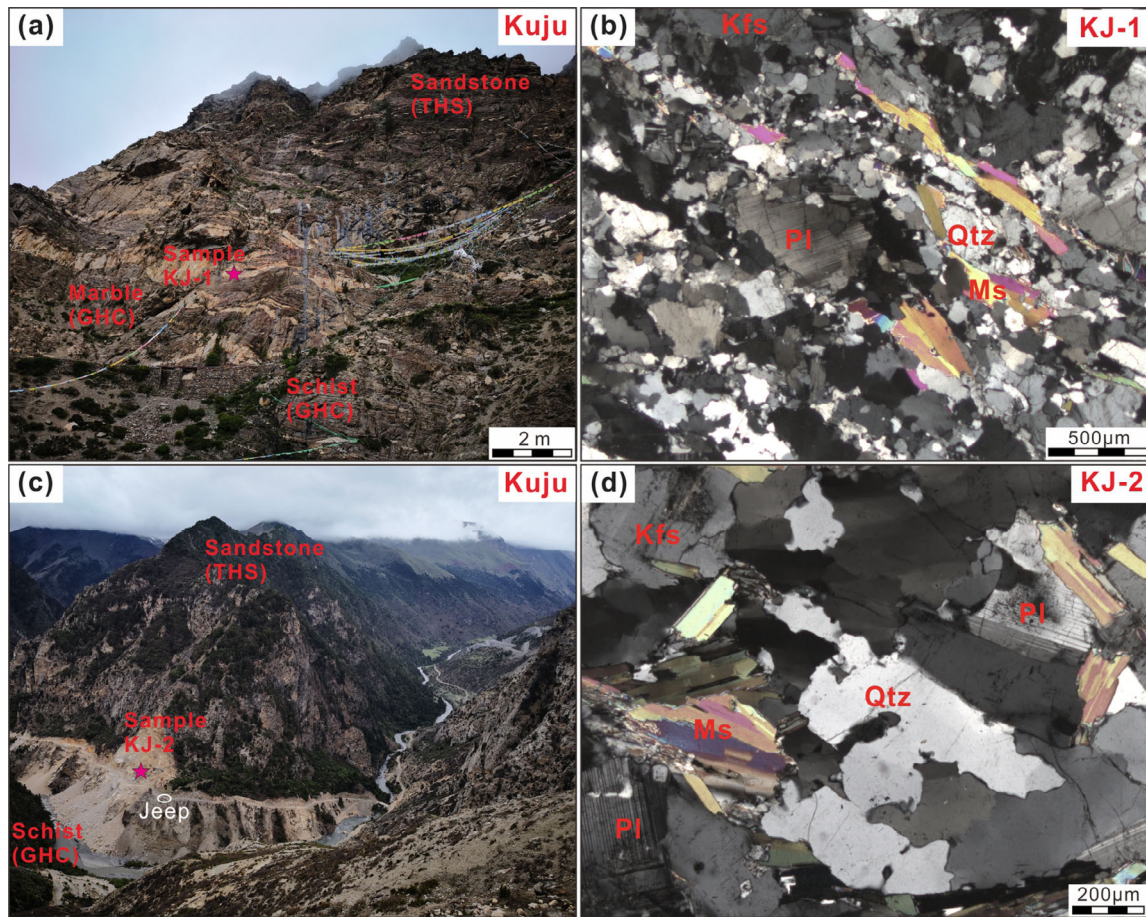


FIGURE 4 (a and b) Photographs showing the geology and mineralogical features of the deformed leucogranites (sample KJ-1) in Kuju. (c and d) showing the geology and mineralogical features of the undeformed leucogranites (sample KJ-2) in Kuju [Color figure can be viewed at wileyonlinelibrary.com]

the laser ablation system and the ICP-MS instrument and data reduction were the same as those described by Zong et al. (2017). Laser sampling was performed using a GeoLasPro laser ablation system that consists of a COMPexPro 102 ArF excimer laser (wavelength of 193 nm and maximum energy of 200 mJ) and a MicroLas optical system. An Agilent 7700e ICP-MS instrument was used to acquire ion signal intensities. Helium was applied as a carrier gas. Argon was used as the make-up gas and mixed with the carrier gas via a T-connector before entering the ICP. A “wire” signal-smoothing device was included in this laser ablation system (Hu et al., 2015).

The spot size and frequency of the laser were set to 24 μm and 5 Hz, respectively, for zircon dating. Zircon 91500 and glass NIST610 were used as external standards for zircon U–Pb dating and trace element calibration, respectively. The spot size and frequency of the laser were set to 16 μm and 2 Hz, respectively, for monazite dating. Monazite standard 44069 and glass NIST610 were used as external standards for monazite U–Pb dating and trace element calibration, respectively.

Each analysis incorporated a background acquisition of approximately 20–30 s followed by 50 s of data acquisition from the sample. The Excel-based program ICPMSDataCal was used to perform offline selection and integration of background and analysed signals and

time-drift correction and quantitative calibration for trace element analysis and U–Pb dating (Liu et al., 2010). Concordia diagrams and weighted mean calculations were constructed using Isoplot/Ex_ver3.75 (Ludwig, 2012). The ages are weighted means with 2 sigma (2σ) errors calculated at 95% confidence levels. The zircon and monazite in situ LA-ICP-MS U–Pb dating results of the leucogranites are presented in Tables S1 and S2.

4 | ANALYTICAL RESULTS

4.1 | Zircon U–Pb geochronology

Cenozoic zircons of the deformed and undeformed leucogranites from LZ, KJ, and CND dome in the eastern Himalaya have lower Th/U ratios (usually less than 0.1; Figure 7a) and high Th and U contents (Th + U values usually approximately 3,000–10,000 ppm; Figure 7b). The spots are characterized by high Th and U contents, but the nearly constant $^{206}\text{Pb}/^{238}\text{U}$ ages with large variations in Th + U concentrations (Figure 7b) indicate that the zircon U–Pb system was not strongly affected by high U content (Zeng et al., 2015).

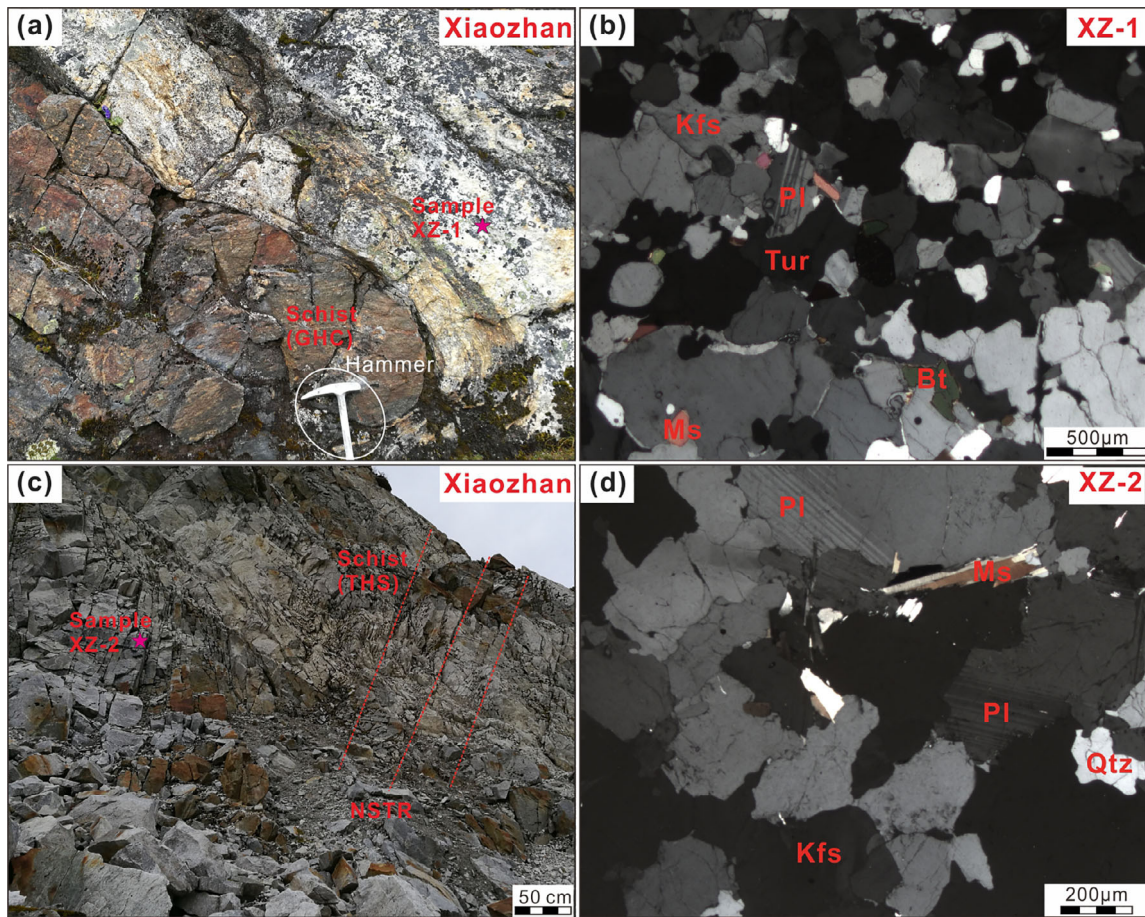


FIGURE 5 (a and b) Photographs showing the geology and mineralogical features of the deformed leucogranites (sample XZ-1) in Xiaozhan. (c and d) showing the geology and mineralogical features of the undeformed leucogranites (sample XZ-2) in Xiaozhan [Color figure can be viewed at wileyonlinelibrary.com]

4.1.1 | LZ leucogranites

Most of the zircon crystals extracted from the LZ (samples LZ-1 and LZ-2) leucogranites are euhedral to subhedral prisms, 80–200 μm in length with aspect ratios of 2:1 to 3:1. CL images reveal that most grains display core–rim textures (Figure 8a,d). The cores are commonly irregular and display brighter oscillatory zoning, and the rims show homogeneous dark bands with weak oscillatory growth zoning.

Seventeen analyses focused on the dark CL rims and two on the light cores for the deformed two-mica granite (LZ-1). The rim has two groups of peak values of $^{206}\text{Pb}/^{238}\text{U}$ ages, except for one with an age of 18.9 Ma (Figure 8b). The older three analyses range from 30.1 to 30.6 Ma, and the other 13 spots yield approximately uniform $^{206}\text{Pb}/^{238}\text{U}$ ages from 24.1 to 24.9 Ma with a mean age of 24.6 Ma ($n = 13$, mean square weighted deviation [MSWD] = 0.9; Figure 8c). The two analyses on cores (inherited zircons) yield 470.9 and 480.5 Ma. We interpret the spots clustering at approximately 24.6 Ma on the U–Pb concordia diagram as reflecting the crystallization time for the deformed granite, and the 18.9 Ma age represents the timing of metamorphism.

Sixteen analyses focused on the dark CL rims and one on the light core for the undeformed garnet-bearing muscovite granite (LZ-2). The 14 rim spots yield $^{206}\text{Pb}/^{238}\text{U}$ ages from 13.3 to 14 Ma and two spots with ages of 17.7 and 17.4 Ma (Figure 8e). The younger 14 analyses define a weighted mean age of 13.6 Ma ($n = 14$, MSWD = 1.4; Figure 8f), which are taken to represent the time of crystallization for the undeformed granite. One analysis on a core yields 289.7 Ma for the inherited zircon.

4.1.2 | KJ leucogranites

All the zircons from KJ leucogranites display euhedral to subhedral crystals and sponge-like textures and are stout prisms, 50–150 μm long and 50–100 μm wide (Figure 9a,d). In spite of the low Th/U ratios ranging from 0.004 to 0.39 (average at 0.04; Figure 7a), the well-developed oscillatory zoning suggests a magmatic origin and growth from granitic melts (Zeng et al., 2015).

A total of 14 spots were analysed for the deformed leucogranite (KJ-1) and form a tight cluster on the concordia curve (Figure 9b), yielding concordant $^{206}\text{Pb}/^{238}\text{U}$ ages from 23.1 to 24.2 Ma with a

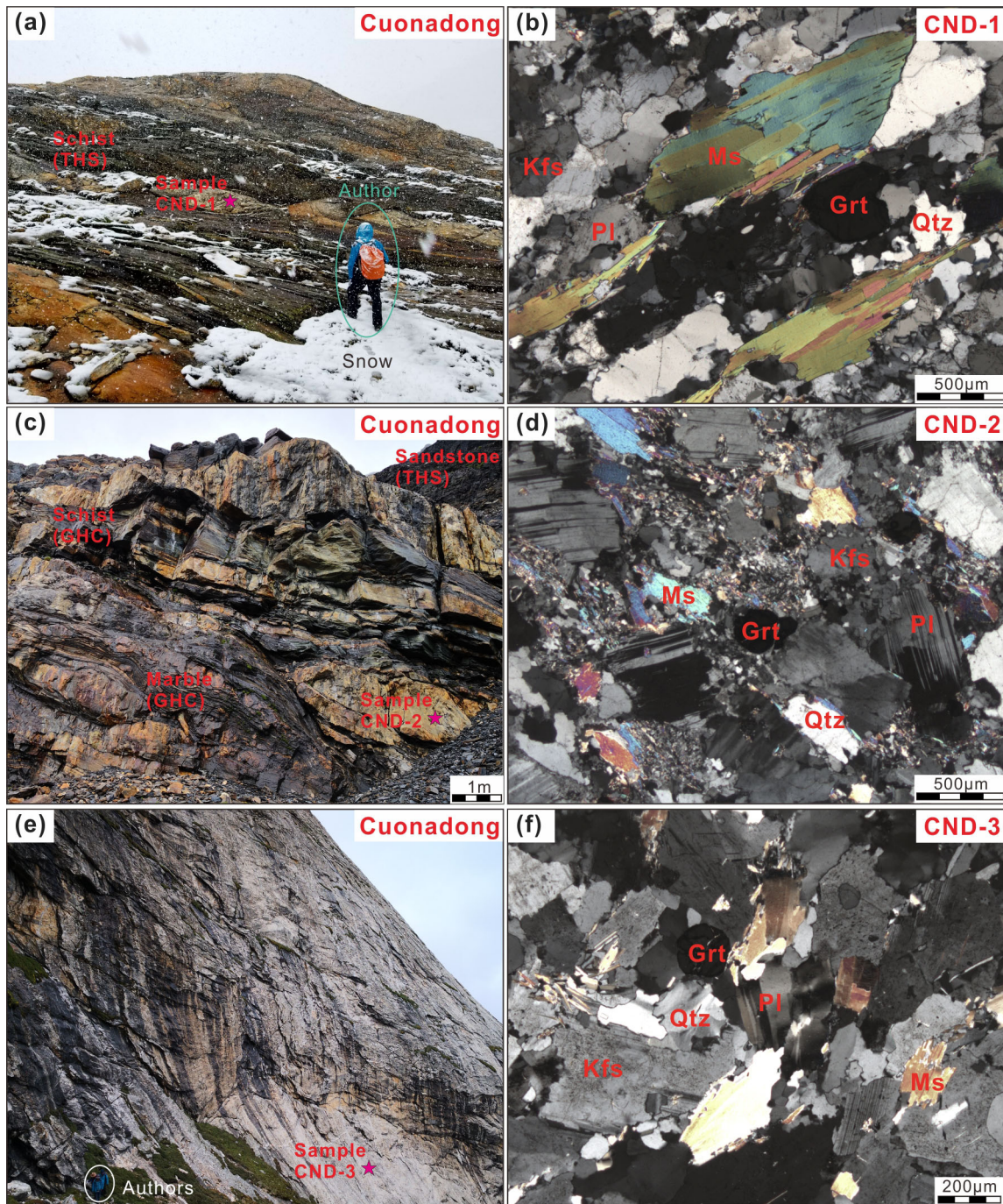


FIGURE 6 (a and b) Photographs showing the geology and mineralogical features of the deformed leucogranites (sample CND-1) in Cuonadong. (c and d) showing the geology and mineralogical features of the deformed leucogranites (sample CND-2) in Cuonadong. (e and f) showing the geology and mineralogical features of the undeformed leucogranites (sample CND-3) in Cuonadong [Color figure can be viewed at wileyonlinelibrary.com]

weighted mean age of 23.4 ± 0.2 Ma ($n = 14$, MSWD = 1.9; Figure 9c). A total of 12 spots were analysed for the undeformed leucogranite (KJ-2) and form a tight cluster on the concordia curve (Figure 9e), yielding concordant $^{206}\text{Pb}/^{238}\text{U}$ ages from 16.2 to 16.9 Ma with a weighted mean age of 16.5 ± 0.1 Ma ($n = 12$, MSWD = 1.5; Figure 9f). Thus, we interpret the weighted mean ages of 23.4 and 16.5 Ma as the crystallization ages of the deformed muscovite leucogranite and undeformed tourmaline-bearing muscovite granite, respectively.

4.1.3 | CND leucogranites

Zircon grains separated from CND leucogranites are euhedral to subhedral, long prisms and 100–300 μm long with aspect ratios of 2:1 to 3:1. Most of the zircon grains have core–rim structures (Figure 10a,d,g), with light and irregular cores and dark grey and oscillatory overgrowth rims. The LA-ICP-MS spots on the sponge-like and oscillatory overgrowth zoning domains have the

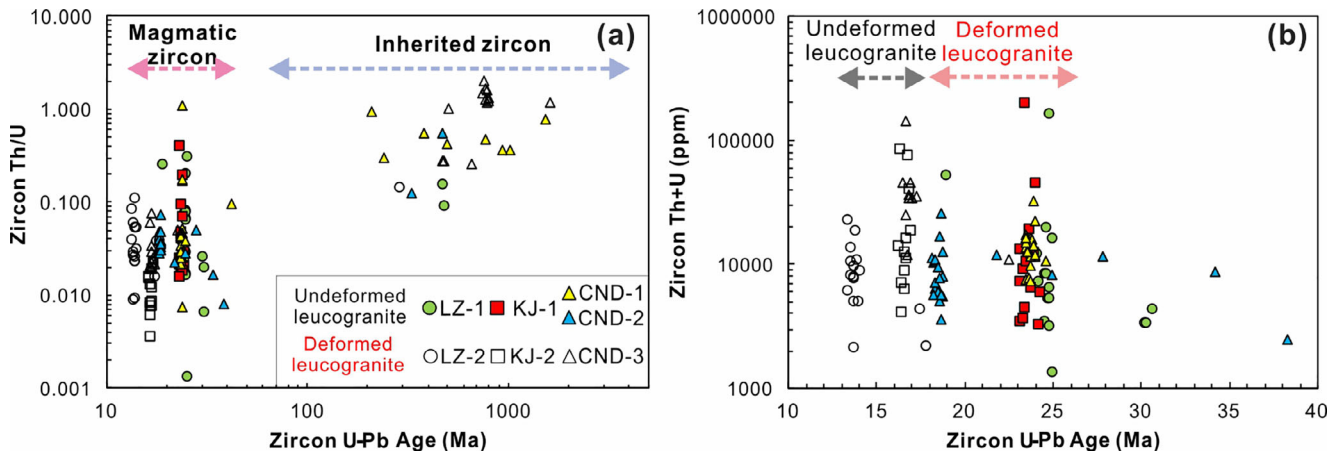


FIGURE 7 Variation of zircon U–Pb ages with Th/U and Th + U values of the deformed and undeformed leucogranites from Lhozhaq (LZ-1 and LZ-2), Kuju (KJ-1 and KJ-2) and Cuonadong dome (CND-1, CND-2, and CND-3) [Color figure can be viewed at wileyonlinelibrary.com]

same ages, which suggests that all zircon rims are magmatic (Figure 10).

There were twenty-one analyses on zircon rims of deformed garnet-bearing two-mica granite (CND-1). Except for one spot with an age of 42.1 Ma, the other 20 spots on the zircon rims form a tight cluster on the concordia curve (Figure 10b), yielding concordant $^{206}\text{Pb}/^{238}\text{U}$ ages from 23.4 to 24.6 Ma with a weighted mean age of 23.7 ± 0.2 Ma ($n = 20$, MSWD = 1.3; Figure 10c). Eight analyses on the cores yield $^{206}\text{Pb}/^{238}\text{U}$ ages of 210.7–1,547 Ma.

Five spots on zircon rims of deformed garnet-bearing muscovite granite (CND-2) yield relatively concordant $^{206}\text{Pb}/^{238}\text{U}$ ages ranging from 38.3 to 24.9 Ma. However, 20 analyses are clustered at approximately 18 Ma on the concordia curve (Figure 10e) and yield a weighted mean age of 18.4 ± 0.1 Ma ($n = 20$, MSWD = 2; Figure 10f). In addition, two cores give ages of 470.3 and 329.2 Ma.

Undeformed garnet-bearing muscovite granite (CND-3) has abundant inherited zircon cores. Thirteen spots on zircon core range from 472.1 to 1,616.8 Ma. It is worth noting that seven spots cluster around 786 Ma ($n = 7$, MSWD = 2.6; Figure 10h). Except for one spot with an age of 22.4 Ma, the other nine spots on the zircon rims form a tight cluster on the concordia curve (Figure 10h), yielding a weighted mean age of 16.8 ± 0.2 Ma ($n = 9$, MSWD = 0.6; Figure 10a).

We interpret the weighted mean ages of 23.7, 18.4, and 16.8 Ma as the crystallization times of the deformed two-mica granite (CND-1), the muscovite granite (CND-2), and the undeformed muscovite granite (CND-3), respectively.

4.2 | Monazite U–Pb geochronology

Most monazite grains are euhedral to subhedral with grain sizes of 80–200 μm . In backscattered electron images, they are homogeneous, and a few of them show weak oscillatory overgrowth or patchy zoning (Figures 11, 12, and 13). Young monazite (Cenozoic) usually contains high ^{232}Th and ^{208}Pb , low amounts of radiogenic ^{207}Pb , and excess ^{206}Pb ; as a result, $^{208}\text{Pb}/^{232}\text{Th}$ dates are more precise than

$^{206}\text{Pb}/^{238}\text{U}$ and $^{207}\text{Pb}/^{235}\text{U}$ ages (Cottle, Searle, Jessup, Crowley, & Law, 2015). In this study, we take monazite $^{208}\text{Pb}/^{232}\text{Th}$ ages as the best estimates of the crystallization ages of the leucogranites. Except for monazite grains in the undeformed garnet-bearing muscovite granite (LZ-2) from LZ, no inherited ages are identified. Notably, the monazite $^{208}\text{Pb}/^{232}\text{Th}$ ages are similar to the zircon $^{206}\text{Pb}/^{238}\text{U}$ ages of their counterpart leucogranites.

4.2.1 | LZ leucogranites

Eleven analyses on monazite from deformed two-mica granite (LZ-1) in LZ define a weighted mean $^{208}\text{Pb}/^{232}\text{Th}$ age of 24.4 ± 0.1 Ma ($n = 11$, MSWD = 1; Figure 11d). There were 20 measurements on monazite grains from undeformed garnet-bearing muscovite granite (LZ-2). Six spots yield $^{208}\text{Pb}/^{232}\text{Th}$ ages of 14.8–26.2 Ma (Figure 11f), but the other 14 analyses yield a weighted mean $^{208}\text{Pb}/^{232}\text{Th}$ age of 13.6 ± 0.1 Ma ($n = 14$, MSWD = 3; Figure 11h).

4.2.2 | KJ leucogranites

The $^{208}\text{Pb}/^{232}\text{Th}$ dates and $^{206}\text{Pb}/^{238}\text{U}$ ages from the KJ leucogranites are concordant and define a tighter cluster on the concordia curve (Figure 12b,f). Thirty-one spots on monazite from deformed muscovite granite (KJ-1) yield a $^{208}\text{Pb}/^{232}\text{Th}$ weighted average age of 23.9 ± 0.1 Ma ($n = 31$, MSWD = 1.9; Figure 12d). Twenty-seven spots on monazite from undeformed tourmaline-bearing muscovite granite (KJ-2) yield a $^{208}\text{Pb}/^{232}\text{Th}$ weighted average age of 16.9 ± 0.1 Ma ($n = 27$, MSWD = 0.6; Figure 12h).

4.2.3 | XZ leucogranites

Monazite grains from the XZ deformed tourmaline two-mica granite (XZ-1) yield homogeneous $^{208}\text{Pb}/^{232}\text{Th}$ dates with a weighted average

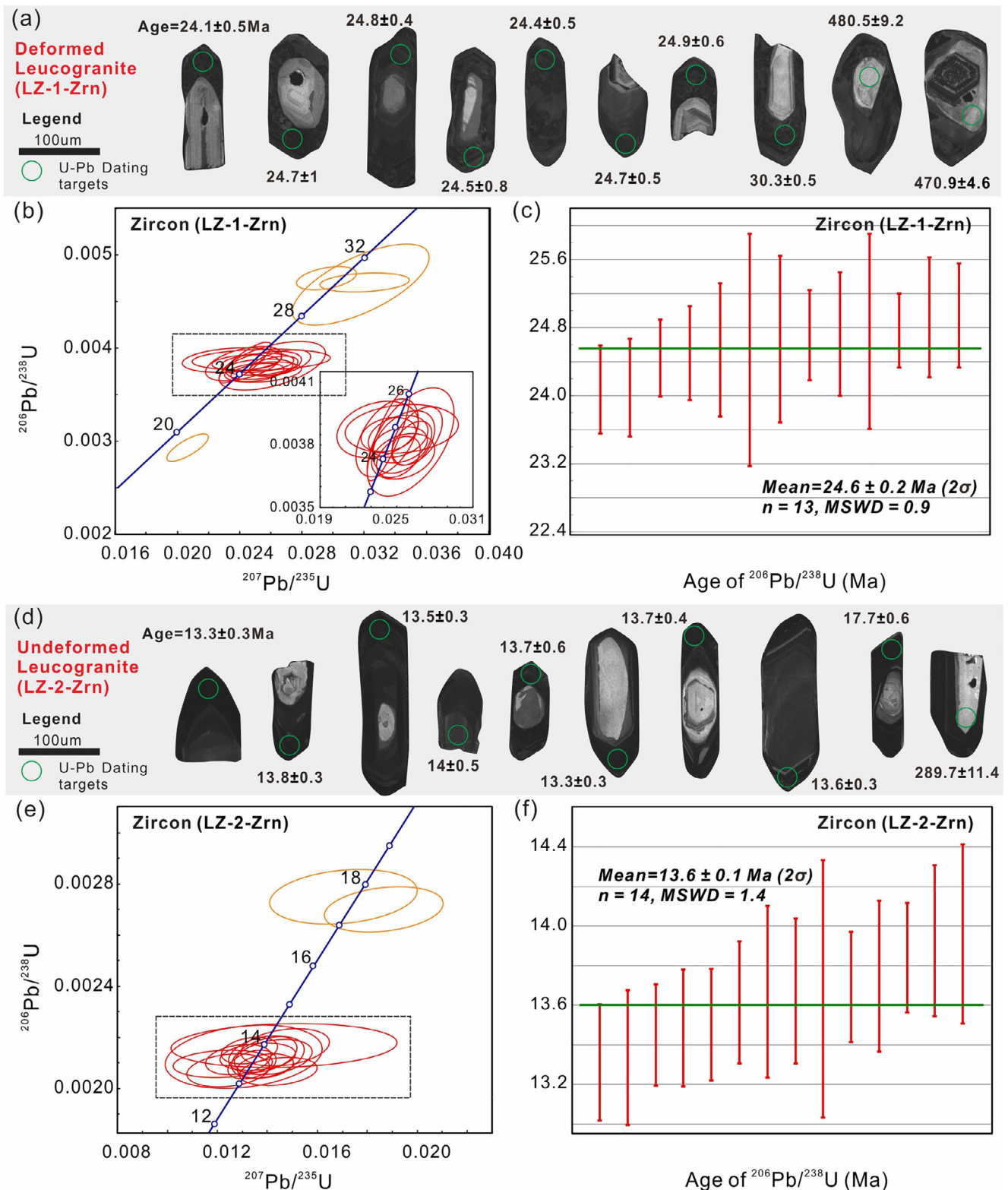


FIGURE 8 Cathodoluminescence (CL) images of representative zircon grains (a and d), zircon laser ablation–inductively coupled plasma–mass spectrometry U–Pb concordia diagrams (b and e) and weighted mean model ages of $^{206}\text{Pb}/^{238}\text{U}$ (c and f) for the deformed leucogranite (sample LZ-1) and undeformed leucogranite (sample LZ-2) from Lhozhag [Color figure can be viewed at [wileyonlinelibrary.com](https://onlinelibrary.wiley.com)]

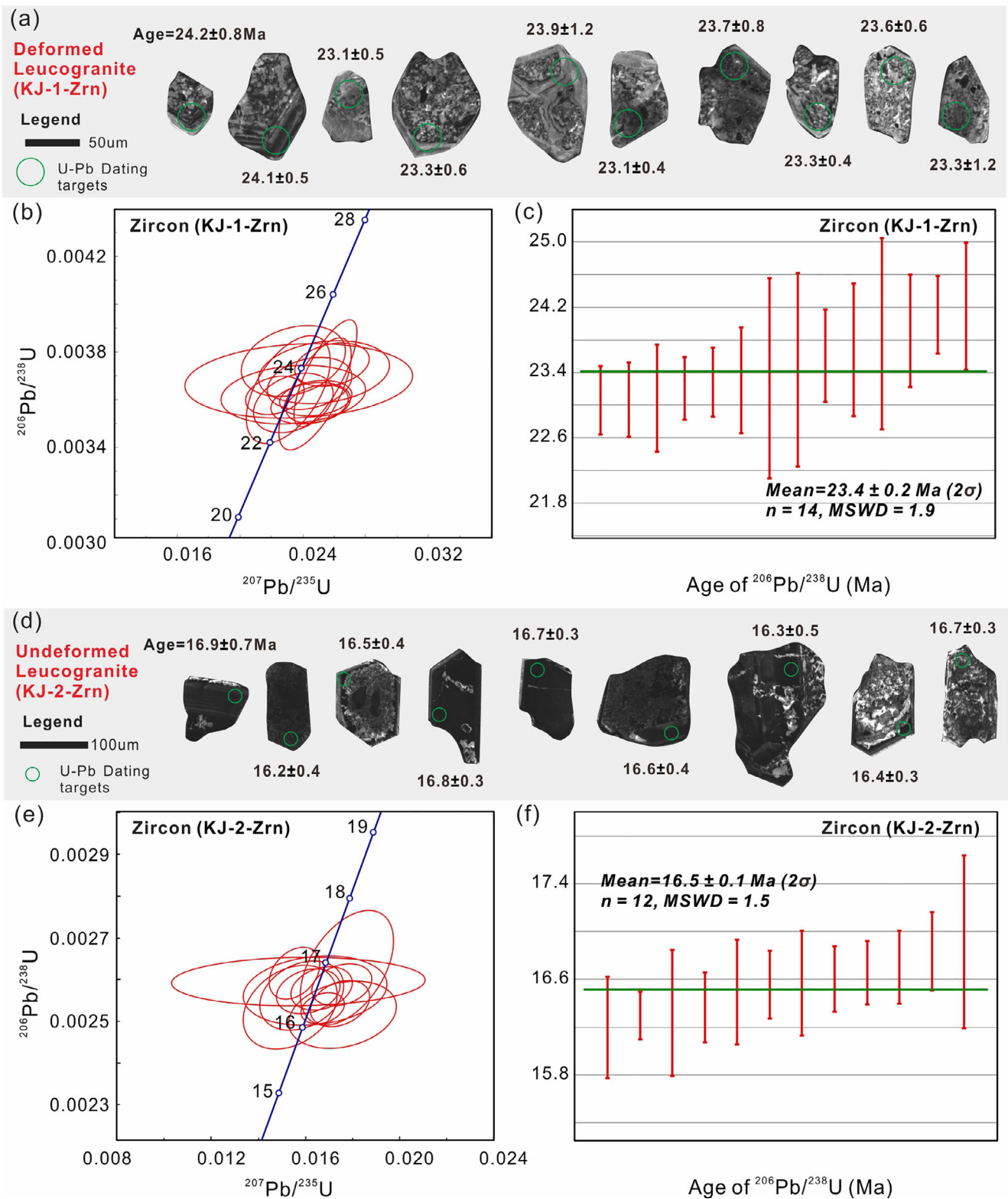


FIGURE 9 Cathodoluminescence (CL) images of representative zircon grains (a and d), zircon laser ablation–inductively coupled plasma–mass spectrometry U–Pb concordia diagrams (b and e) and weighted mean model ages of $^{206}\text{Pb}/^{238}\text{U}$ (c and f) for the deformed leucogranite (sample KJ-1) and undeformed leucogranite (sample KJ-2) from Kuju [Color figure can be viewed at wileyonlinelibrary.com]

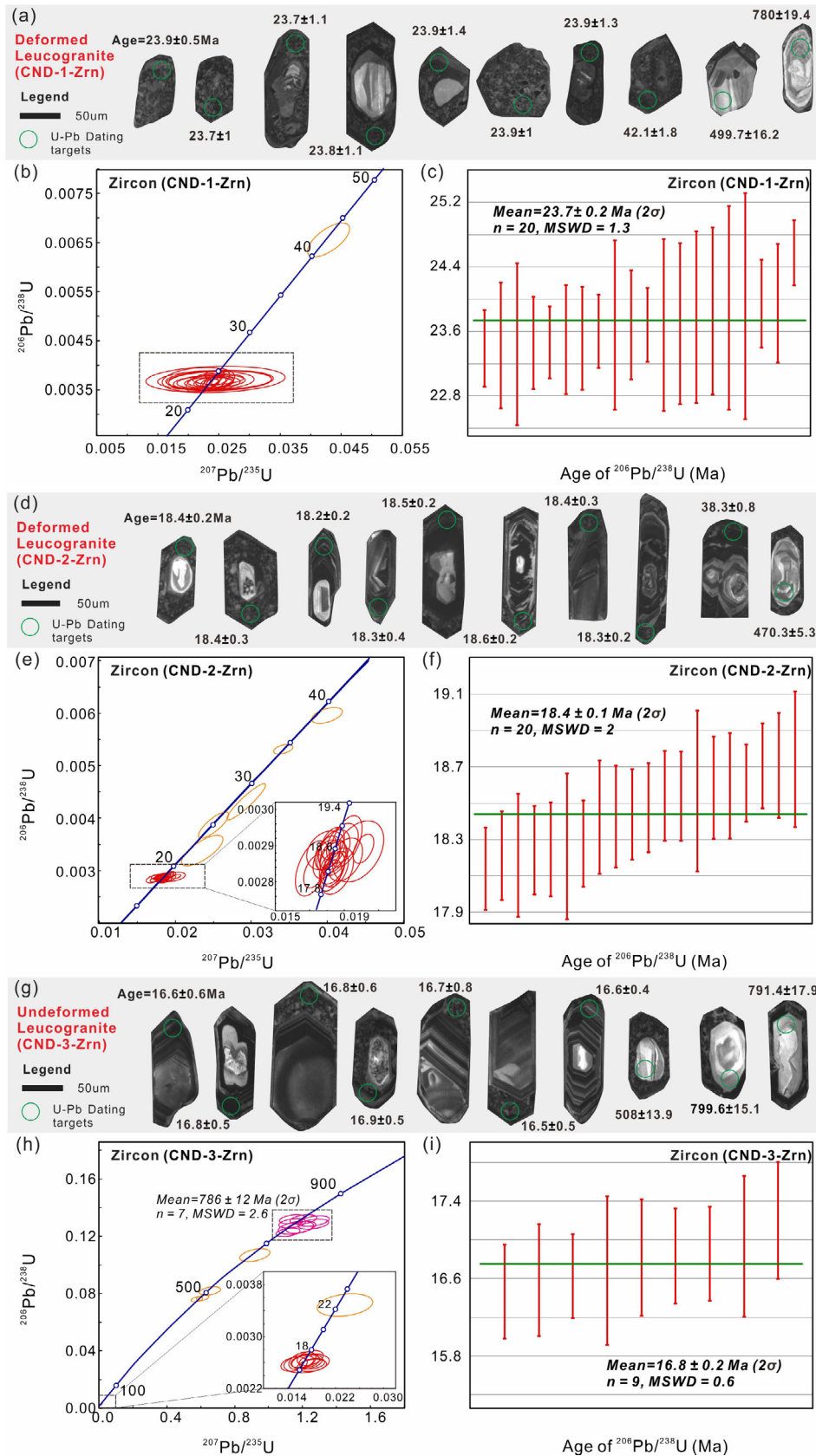


FIGURE 10 Cathodoluminescence (CL) images of representative zircon grains (a, d, and g), zircon laser ablation–inductively coupled plasma–mass spectrometry U–Pb concordia diagrams (b, e, and h) and weighted mean model ages of $^{206}\text{Pb}/^{238}\text{U}$ (c, f, and i) for the deformed leucogranites (samples CND-1 and CND-2) and undeformed leucogranite (sample CND-3) from Cuonadong [Color figure can be viewed at wileyonlinelibrary.com]

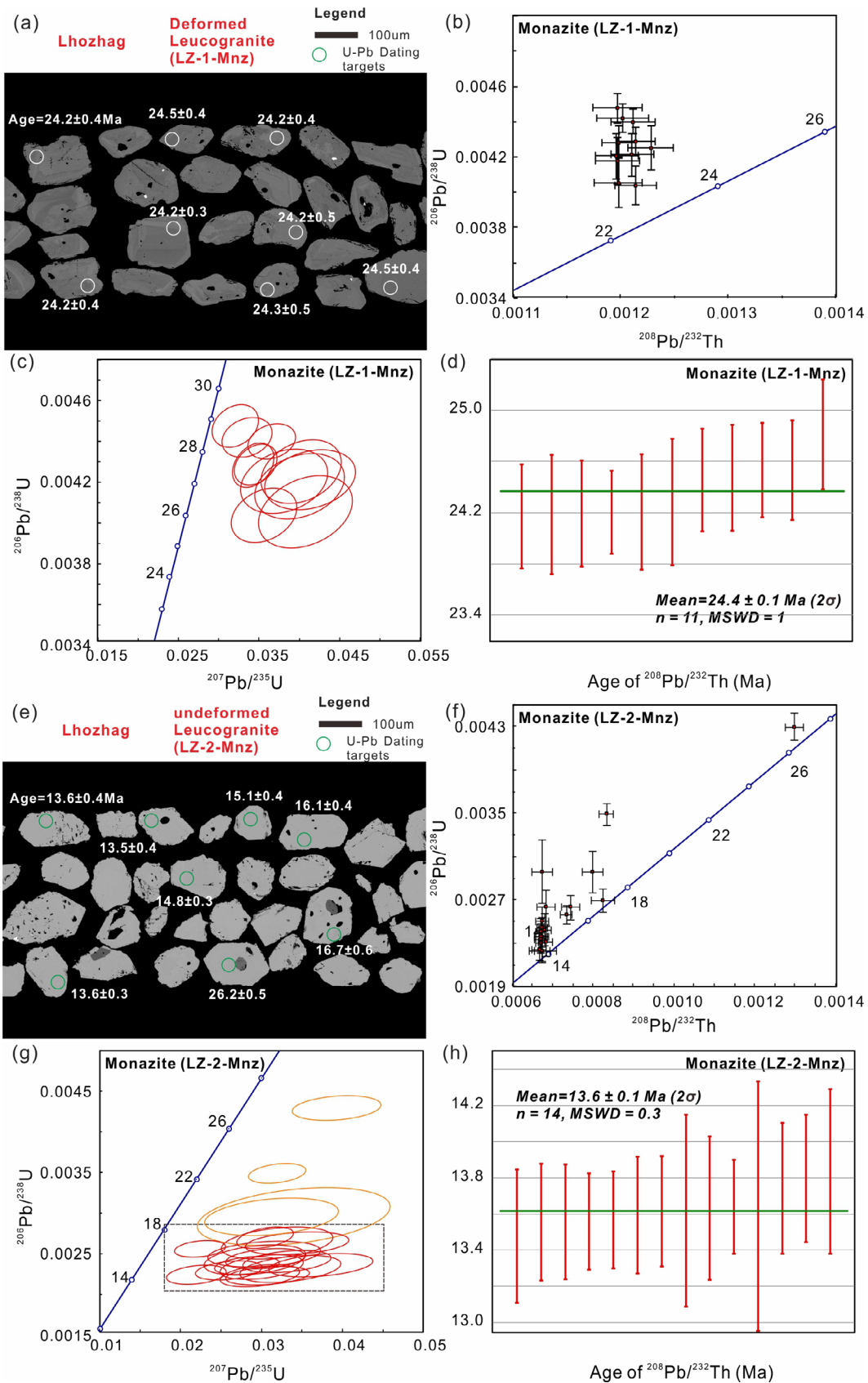


FIGURE 11 Backscattered electron (BSE) images of representative monazite grains (a and e), monazite laser ablation–inductively coupled plasma–mass spectrometry Th–Pb concordia diagrams (b and f), U–Pb concordia diagrams (c and g) and weighted mean model ages of $^{208}\text{Pb}/^{232}\text{Th}$ (d and h) for the deformed leucogranite (sample LZ-1) and undeformed leucogranite (sample LZ-2) from Lhozhag [Color figure can be viewed at wileyonlinelibrary.com]

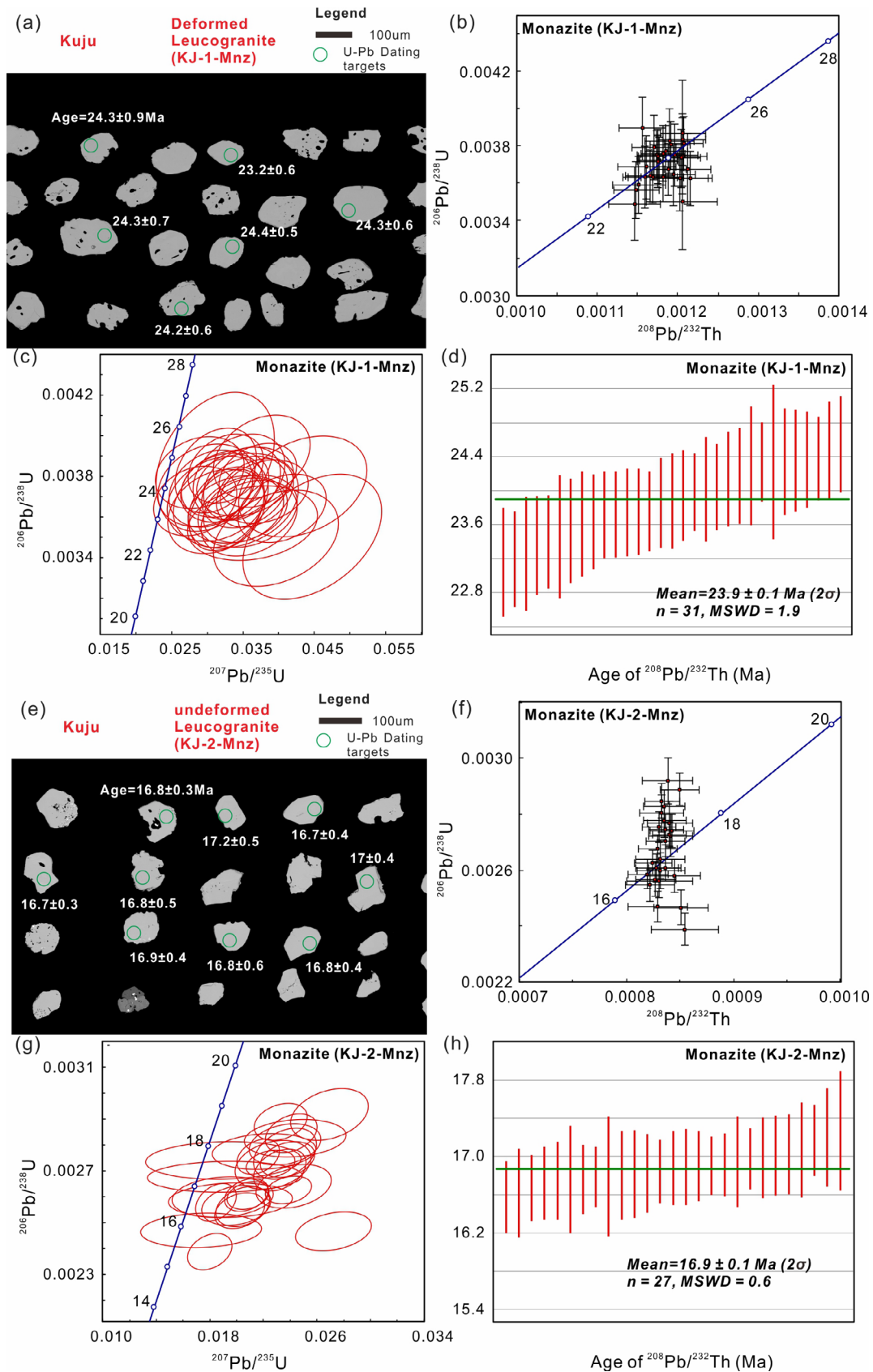


FIGURE 12 Backscattered electron (BSE) images of representative monazite grains (a and e), monazite laser ablation–inductively coupled plasma–mass spectrometry Th–Pb concordia diagrams (b and f), U–Pb concordia diagrams (c and g) and weighted mean model ages of $^{208}\text{Pb}/^{232}\text{Th}$ (d and h) for the deformed leucogranite (sample KJ-1) and undeformed leucogranite (sample KJ-2) from Kuju [Color figure can be viewed at wileyonlinelibrary.com]

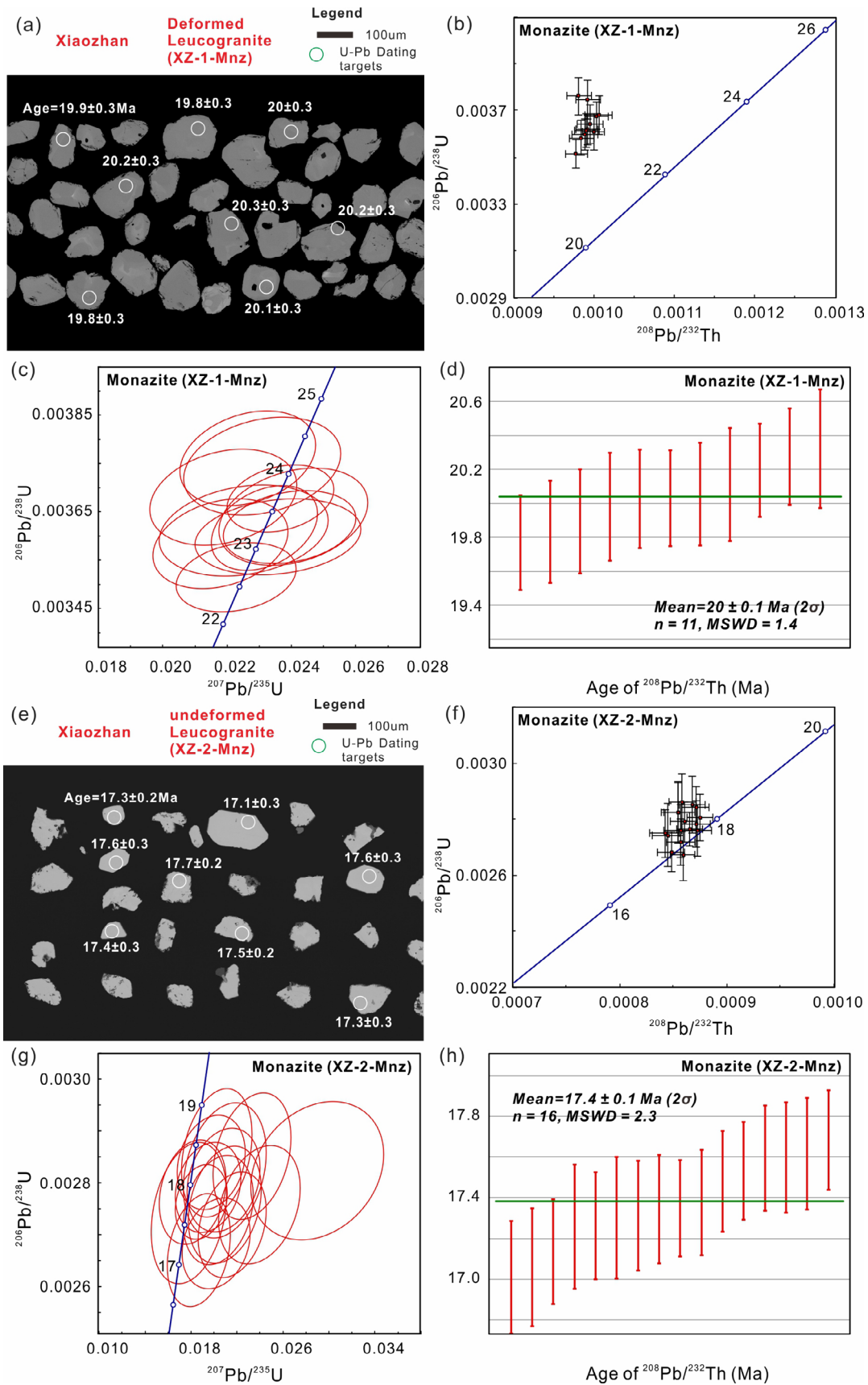


FIGURE 13 Backscattered electron (BSE) images of representative monazite grains (a and e), monazite LA-ICP-MS Th-Pb concordia diagrams (b and f), U-Pb concordia diagrams (c and g) and weighted mean model ages of $^{208}\text{Pb}/^{232}\text{Th}$ (d and h) for the deformed leucogranite (sample XZ-1) and undeformed leucogranite (sample XZ-2) from Xiaozhan [Color figure can be viewed at wileyonlinelibrary.com]

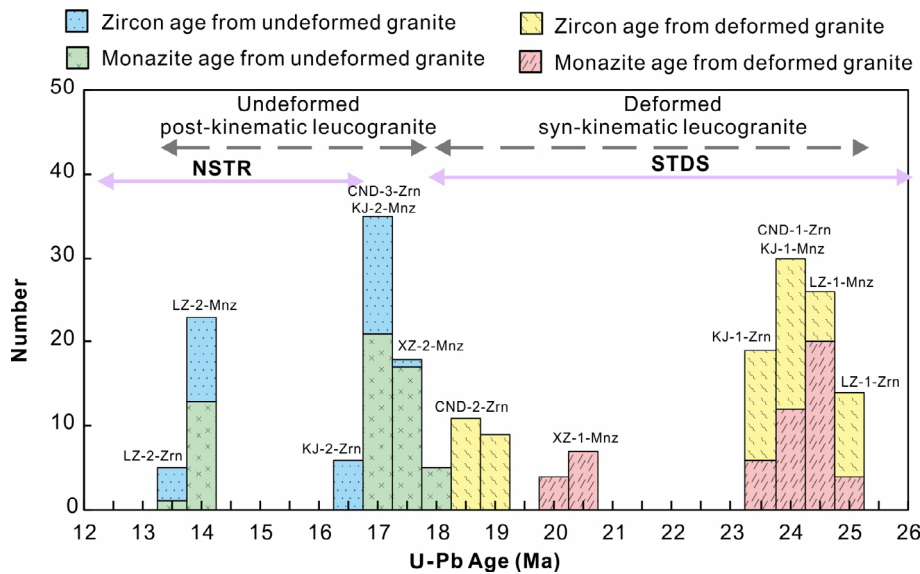


FIGURE 14 Histogram showing the number of U-Pb ages of the deformed and undeformed leucogranites from Lhozhag (LZ), Kuju (KJ), Xiaozhan (XZ) and Cuonadong dome (CND). Zrn, zircon, Mnz, monazite [Color figure can be viewed at wileyonlinelibrary.com]

age of 20 ± 0.1 Ma ($n = 11$, MSWD = 1.4; Figure 13d). Monazite grains from the XZ undeformed muscovite granite (XZ-2) yield homogeneous $^{208}\text{Pb}/^{232}\text{Th}$ dates with a weighted average age of 17.4 ± 0.1 Ma ($n = 16$, MSWD = 2.3; Figure 13h).

5 | DISCUSSION

5.1 | Ages of leucogranites and the cessation of STDS activity in the eastern Himalaya

The zircon and monazite U-Th-Pb ages of deformed two-mica granite (LZ-1) in LZ are 24.6 (Figure 8c) and 24.4 Ma (Figure 11d), respectively. The zircon and monazite U-Th-Pb ages of nondeformed garnet-bearing muscovite granite (LZ-2) are 13.6 Ma (Figures 8f and 11h). According to the ages and structural characteristics of leucogranites in the LZ area, it can be inferred that the starting time of STDS activity in the LZ area was equivalent to or slightly earlier than 25 Ma, and the end of STDS activity was between 25 and 14 Ma.

The zircon and monazite U-Th-Pb ages of the deformed muscovite granite (KJ-1) in the KJ area are 23.4 (Figure 9c) and 23.9 Ma (Figure 12d), respectively. The zircon and monazite U-Th-Pb ages of the undeformed tourmaline-bearing muscovite granite (KJ-2) are 16.5 (Figure 9f) and 16.9 Ma (Figure 12h), respectively. Therefore, it is speculated that the duration of STDS activity at KJ village was ~24–17 Ma. Meanwhile, the tourmaline-bearing muscovite granite (KJ-2) without ductile deformation developed brittle deformation under the influence of Tsona rift (NSTR; Figure 2), so the development time of NSTR was later than 17 Ma.

The U-Th-Pb ages of monazites from two kinds of granites in the XZ area indicate that the intrusive ages of metamorphosed tourmaline two-mica granite (XZ-1) and undeformed muscovite granite (XZ-2) are 20 and 17.4 Ma, respectively. The end of STDS activity in the XZ area was between 20 and 17 Ma. In addition, the fault activity of Tsona rift (NSTR) cut the late muscovite granite (XZ-2; Figures 2 and 5c), so the starting time of NSTR is consistent with the conclusion for the above-

mentioned in KJ area, which is later than the age of the muscovite granite (XZ-2), that is, later than 17 Ma.

The zircon U-Pb ages of deformed two-mica granite (CND-1) and muscovite granite (CND-2) are mainly approximately 23.7 and 18.4 Ma (Figure 10c,f), respectively, while the main zircon U-Pb age of undeformed muscovite granite (CND-3) is approximately 16.8 Ma (Figure 10a). It can be inferred that the detachment shear zone in the CND dome was still active at 18.4 Ma but that ductile deformation ended before 16.8 Ma. Therefore, the end of the activity of the lower ductile detachment fault (the northern extension of the STDS) was between 18.4 and 16.8 Ma.

In summary, the study of leucogranites in four areas of the eastern Himalayas leads to the following three conclusions: (a) the oldest synkinematic leucogranites affected by the STDS are two-mica granites (LZ-1) from LZ, with ages of 24 to 25 Ma, so the starting time of STDS activity was no later than (or earlier than) 25 Ma (Figure 14). (b) The youngest synkinematic leucogranite affected by the STDS is the garnet-bearing muscovite granite (CND-2) in the CND dome, with an age of 18.4 Ma; the oldest postkinematic undeformed leucogranite (not affected by the STDS) is the muscovite granite (XZ-2) in XZ, with an age of 17.4 Ma (Figure 14). (c) Therefore, the end of STDS activity can be limited between 18.4 and 17.4 Ma. The Tsona north-south rift among the NSTR cuts the KJ and XZ rocks, and the youngest leucogranite is the tourmaline-bearing muscovite granite (KJ-2), whose age is 16.9–16.5 Ma. At the same time, the W-Sn ore bodies in the CND dome occur in the north-south rift system fault zone, and the U-Pb age of cassiterite is 14.3 Ma (Cao et al., submitted). Therefore, the starting time range of NSTR can be limited to 16.5–14.3 Ma.

5.2 | Southward thrust shearing along the STDS (Eo-Himalayan 45–28 Ma)

The north-south extension time of the STDS is mainly concentrated in the Miocene, namely, the Neo-Himalayan, but increasingly more

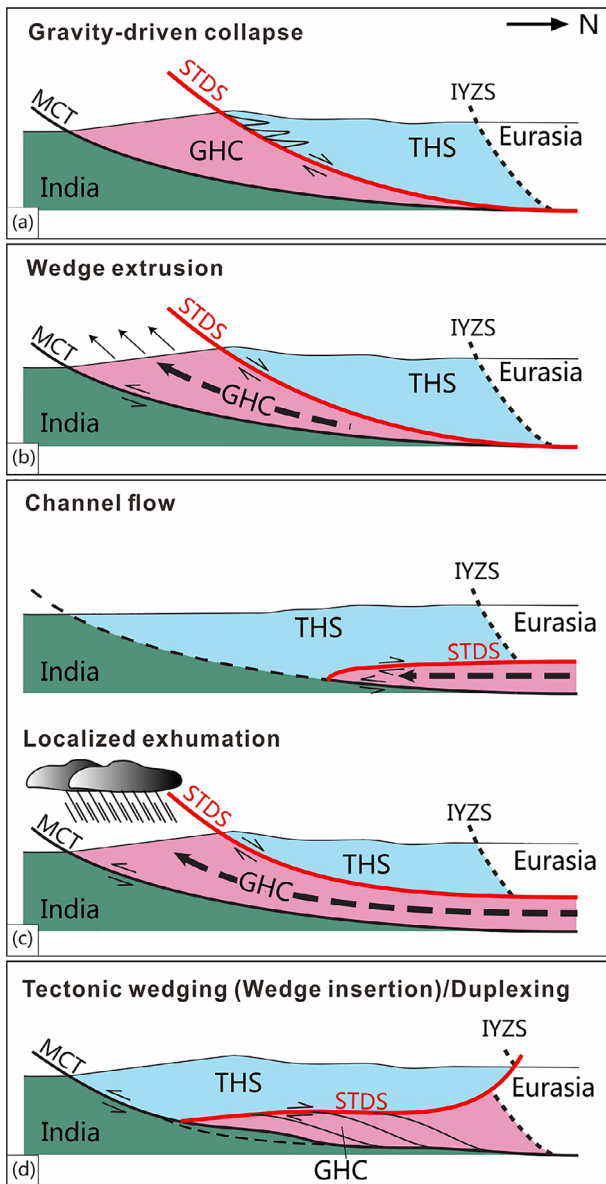


FIGURE 15 Tectonic models for the emplacement and exhumation of the GHC (Webb, 2013) [Color figure can be viewed at wileyonlinelibrary.com]

evidence shows that the predecessor of the STDS was a southward thrust shear zone in the Eocene–Oligocene (Eo-Himalayan; Vannay & Hodges, 1996; Hodges, 2000; Antolín et al., 2011; Finch, Hasalova, Weinberg, & Fanning, 2014; Goscombe et al., 2018; Yang, Liu, Wang, & Wu, 2019). To distinguish these activities easily, this paper names the activity of the south-vergent thrust as the South Tibet Thrust System (STTS) in the early stage and that of the northward extension as the STDS in the late stage. The metamorphism of the GHC includes kyanite-facies Barrovian metamorphism (M1) early in the Eo-Himalayan and sillimanite-facies metamorphism (M2) late in the Neo-Himalayan (Simpson, Parrish, Searle, & Waters, 2000; Viskupic, Hodges, & Bowring, 2005; Walker et al., 1999). The two stages of activity along the STTS and the STDS approximately correspond to the two stages of metamorphism (M1 and M2) in the GHC, respectively.

In the Eo-Himalayan (Eocene–Oligocene), the south-vergent thrust of the STTS resulted in (a) folding, faulting, and greenschist-facies metamorphism of the THS (locally high-pressure metamorphism); (b) northward subduction of the GHC, burial of the GHC, high amphibolite-facies prograde metamorphism (M1), and anatexis; and (c) formation of small amounts of Eocene–Oligocene leucogranite and pegmatite. In the following discussion, this paper summarizes the timing and characteristics of structure, metamorphism, and magmatism in the Eo-Himalayan.

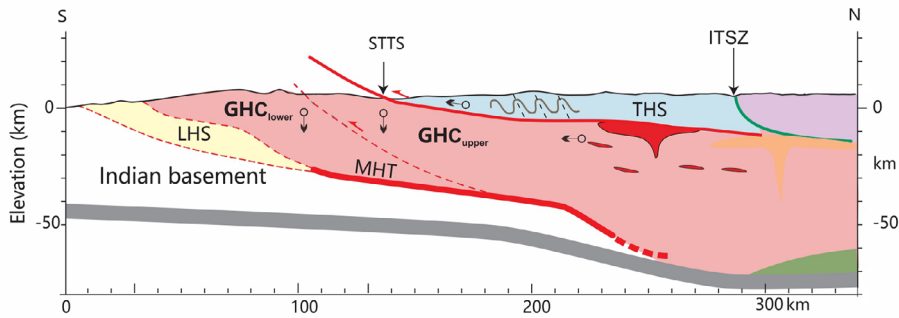
5.2.1 | The Eo-Himalayan metamorphism and deformation in the THS

Anticlines and synclines are widely developed in the THS. The axial traces of these folds are nearly east–west, and the axial planes incline to the north, which is generally interpreted as a result of the southward thrusting of the THS along the STTS (Dunkl et al., 2011; Montomoli et al., 2017). Sericite and muscovite Ar–Ar ages in the low-grade metamorphic strata of the THS record these structural events well. For example, the Ar–Ar ages of K-feldspar are 43, 39, and 32 Ma (Aikman, Harrison, & Lin, 2008) in the THS of Shannan municipality, China. The mica Ar–Ar ages in Gyaca County are 56 and 48 Ma (Zhao et al., 2019), and the U–Th/He age of zircon in southern Zedang town is 37 Ma (Li et al., 2015). The amphibole Ar–Ar age of mylonitic rocks at the bottom of the STDS in the Everest area of China is 33 Ma (Gébelin et al., 2017). The Ar–Ar ages of amphibole–biotite–phlogopite at the bottom of the THS in the Annapura–Manaslu area are 30–27 Ma (Coleman & Hodges, 1998). The K–Ar ages of illite in Dhaulagiri and Hidden Valley in Nepal are 30–25 Ma (Crouzet et al., 2007). The Ar–Ar ages in the Spiti region in India are 46–45 Ma (Wiesmayr & Grasemann, 2002). In the Lapukangri area of Saga County west of the IYZS, the THS strata underwent high-pressure metamorphism, and its Lu–Hf age is 40 Ma, which represents the time of prograde metamorphism (Ding, Paul, & Qiao, 2005; Laskowski, Kapp, Vervoort, & Ding, 2016).

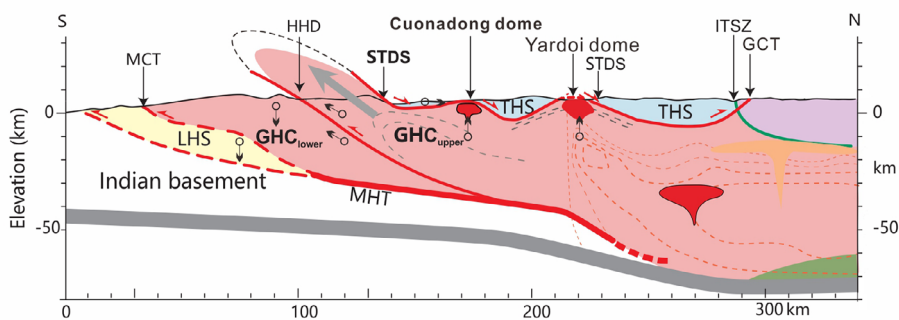
5.2.2 | The Eo-Himalayan metamorphism and deformation in the NHGD and GHS

In the eastern Himalayas, the zircon U–Pb ages of schist in the CNL dome are 47–29 Ma (Ding, Li, & Jiang, 2019). In this study, inherited zircon ages of late Eocene–early Oligocene are also obtained in the leucogranites (Figure 10). The zircon U–Pb ages of the metamorphic rocks of the Yardoi dome indicate that they underwent prograde metamorphism at 48–36 Ma (Ding et al., 2016; Ding et al., 2016; Gao, Zeng, & Xie, 2012). The zircon U–Pb ages of the two-mica granitic gneiss in the core of the Ramba dome are 44–43 Ma (Liu, Wu, Ji, Wang, & Liu, 2014). The earlier metamorphic ages of garnet Lu–Hf in the sillimanite–kyanite-bearing gneiss in the Mabjia and Kangmar domes are 54–52 and 51–49 Ma, respectively (Smit, Hacker, & Lee, 2014). The hornblende Ar–Ar age of the amphibolite in the Mabjia

(a) 45–28 Ma: STTS south-vergent ductile thrust



(b) 28–17 Ma: HDD south-vergent ductile thrust, North-South extension (STDS), doming of Cuonadong



(c) 17–9 Ma: MCT south-vergent ductile thrust, East-West extension (NSTR)

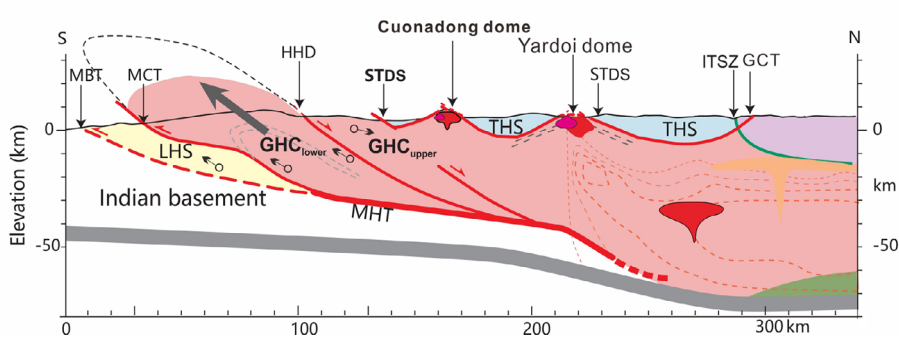


FIGURE 16 Diagrammatic summary of the in-sequence shearing tectonic model, evolution of the STDS and exhumation of the GHC in the Himalayan (Goscombe et al., 2018) [Color figure can be viewed at wileyonlinelibrary.com]

dome also shows the metamorphic activity of this period (Lee, McClelland, Wang, Blythe, & McWilliams, 2006). However, the U–Pb isotope record of the zircon rims of the sillimanite-bearing gneiss in the Mabjia dome shows a metamorphic age of 35 Ma (Lee & Whitehouse, 2007). The U–Pb zircon age of mylonitic augen gneiss in the Xiao Gurla area of the western Himalayas is 35 Ma (Pullen, Kapp, DeCelles, Gehrels, & Ding, 2011). According to the U–Pb age of the monazite from metamorphic rock in the core of the Leo Pargil dome, Langille, Jessup, Cottle, Lederer, and Ahmad (2012) proposed that the time of prograde Barrovian metamorphism of the GHC is 40–28 Ma. Garnet and whole-rock Sm–Nd ages are 33–28 Ma in the Zanskar Himalayas (Vance & Harris, 1999). Through further work, Horton, Lee, Hacker, Bowman-Kamaha'o, and Cosca (2015) found that the U–Th–Pb ages of monazite in the gneiss and pegmatite veins of the Gianbul dome are 37–33 Ma, representing the time of prograde Barrovian metamorphism (M1) of the GHC. Metamorphism at 36–28 Ma is also developed in the GHC in central and eastern Bhutan (Zeiger et al., 2015).

In addition, a large number of M1 metamorphism records have been preserved in the middle Himalaya. The monazite U–Th–Pb age

of limited Barrovian-type sillimanite-bearing metamorphic rocks in the Kala Patat of the Everest area from the GHC yields a peak metamorphic time of 32 Ma (Simpson et al., 2000), which is consistent with the 33-Ma metamorphic time reflected by the zircon U–Pb age in the Kharta area (Liu, Siebel, Massonne, & Xiao, 2007), and the U–Th–Pb ages of monazite in the Dudh Kosi Everest GHC are 46–34 Ma (Catlos et al., 2002). The whole-rock Rb–Sr age of the Yellow Band in the Everest area is 40 Ma, and the muscovite Ar–Ar age is 33 Ma (Sakai et al., 2005). The U–Th–Pb age of monazite from cordierite-bearing metamorphic rocks in the Makalu area is limited to 35 Ma (Street et al., 2010); the study of Kangshung Valley (Cottle, Searle, Horstwood, & Waters, 2009) advances the metamorphic age to 39 Ma. Therefore, the M1 metamorphic age in the Everest area is between 46 and 32 Ma. The Rb–Sr age of kyanite-bearing metamorphic rocks in the GHC of Langtang Valley is 34 Ma, indicating that the M1 metamorphism time is before 34 Ma (Inger & Harris, 1992). Zircon U–Pb ages of the sillimanite migmatitic gneiss are concentrated from 34 to 40 Ma in Nyalam, China (Wang, Zhang, & Wang, 2013). The U–Th–Pb ages of monazite and the Ar–Ar ages of amphibole from the GHC metamorphic rocks in the Annapurna area define the M1

metamorphic time as 36–32 Ma (Godin, Brown, Hanmer, & Parrish, 1999; Godin, Parrish, Brown, & Hodges, 2001; Hodges, Parrish, & Searle, 1996; Vannay & Hodges, 1996). More recently, Larson and Cottle (2015) showed that the monazite U–Th–Pb ages of kyanite gneiss in the GHC of Dhaulagiri Annapurna peak in southern Nepal reveal prograde metamorphism and crustal thickening at 48–30 Ma and melting at 28–18 Ma (Gibson, Godin, Kellett, Cottle, & Archibald, 2016). The results for the Kali Gandaki Valley (Carosi et al., 2015; Iaccarino et al., 2015; Mottram, Cottle, & Kylander-Clark, 2019) and Modi Khola Valley (Corrie & Kohn, 2011; Martin, Gehrels, & DeCelles, 2007) are almost consistent with the above ages. The dating results of monazite–sphene from the GHC metamorphic rocks in Kali Gandaki and Modi Khola show that the timing of M1 kyanite-facies metamorphism is 43–28 Ma and that of decompression melting is 25–18 Ma.

Monazites in kyanite-bearing gneisses from the Lower Dolpo area in the western Himalayas record prograde events from 43 to 33 Ma (Carosi, Montomoli, Rubatto, & Visonà, 2010). The U–Th–Pb ages of monazite in garnet are 44–36 Ma (Foster, Kinny, Vance, Prince, & Harris, 2000) of the Bhagirathi Valley in the Garhwal area, and the U–Pb ages of zircons from migmatite and in situ partial melt are 46–20 Ma (Singh, 2019). The garnet Sm–Nd ages of pegmatites in the Malana Parbati area are 41 and 29 Ma (Thöni, Miller, Hager, Grasemann, & Horschinegg, 2012). Stübner et al. (2014) dated the U–Pb ages of monazite and zircon, and the ages of Barrovian prograde metamorphism in the Himachal Pradesh area are 41–27 Ma, which are similar to the U–Pb ages of monazite in garnet from mica schist (34–28 Ma) at the bottom of the THS in the Morong area (Chambers et al., 2009).

There are not only many Eo-Himalayan metamorphic rocks in the NHGD and GHC but also much related information in the klippe. In the Bhutan area, the U–Th–Pb ages of monazite from the STTS shear zone of the Karnali klippe indicate that M1 prograde metamorphism occurred in the bottom of the THS at 36–30 Ma (Soucy La Roche, Godin, Cottle, & Kellett, 2016). The U–Th–Pb ages of monazite enclosed in kyanite and garnet in the lower part of the Karnali klippe are 47–30 Ma (Braden, Godin, & Cottle, 2017; Soucy La Roche, Godin, Cottle, & Kellett, 2018), indicating that M1 prograde metamorphism also occurred in the GHC at 47–30 Ma.

5.2.3 | The Eo-Himalayan leucogranite-pegmatite in the NHGD and GHS

The Eocene–Oligocene leucogranites and pegmatites are another manifestation of structural activity in the Eo-Himalayan period. Strongly deformed σ -type and lenticular leucogranite and pegmatite are developed in the detachment fault of the CND dome. The Yardo dome not only recorded late Eocene–early Oligocene metamorphism in schist and gneiss but also extensively developed contemporaneous (44–35 Ma) magmatic rocks (Aikman, Harrison, & Hermann, 2012; Zeng et al., 2015; Zeng, Gao, Xie, & Jing, 2011; Zeng, Liu, Gao, Xie, & Wen, 2009). The zircon and monazite U–Th–Pb ages of the deformed leucogranite in the Xiaoru dome are 36–34 Ma (Liu et al., 2016). The age of lenticular leucogranite in the detachment zone from the

Changgo dome is 35 Ma (Larson et al., 2010). The U–Th–Pb ages of monazite in schist and mylonite pegmatite in the Zanskar area are 37–29 Ma (Walker et al., 1999).

In conclusion, it is believed that shortly after the India–Lhasa collision, the south-vergent STTS occurred throughout the Himalayas from 45 to 28 Ma (Eo-Himalayan), which resulted in thrusts, folds, faults, and low-grade metamorphism in the hanging wall (THS), as well as subduction, crustal thickening, burial, melting, and M1 metamorphism in the footwall (GHC).

5.3 | Northward extension shearing along the STDS (Neo-Himalayan 28–17 Ma)

In addition to the development of the STDS between the northern GHC and the THS, a series of klippe developed in Nepal, central and western Bhutan, and northwest India. These klippe belong to the THS and are separated from the GHC by the STDS. For the convenience of distinction, the north side (or hinterland) of the STDS is defined as the inner STDS, and the south side (or foreland) is defined as the outer STDS at the bottoms of klippe (Kellett et al., 2009). Most researchers interpret the detachment shear zone in the NHGD as the northern continuation of the STDS (Larson et al., 2010). Compared with the typical NHGD dome in the THS, the Ama Massif, Gurla Mandhata, and Leo Pargil domes were exhumed during orogen-parallel extension in a later period, which formed with the NSTR and postdates the STDS (Jessup et al., 2019).

In this paper, we consider that the STDS in the Himalayas can be divided into three types: (a) the detachment zone of the NHGD on the north side of the THS, (b) the *strict sense* STDS or inner STDS between the GHC and the THS, and (c) the outer STDS at the bottoms of klippe on the south side of the GHC. In this paper, we review the previous research results on the time limits of the STDS (north–south extension) from the eastern to the western Himalaya.

5.3.1 | Detachment faults or shear zones (STDS) in the NHGD

CND dome (92°5'E)

The age of the deformed leucogranite in the core of the CND dome ranges from 24 to 18 Ma (Lin et al., 2016; Dong, Xu, Meng, & Yi, 2017; Gao, Gao, Zhao, Hou, & Tang, 2017; Huang et al., 2018; Zhang et al., 2018; this study), and the age of the undeformed leucogranite is 17–16 Ma (Fu et al., 2018; Xie et al., 2018; Zhang et al., 2018; Xie et al., 2020; This study). The muscovite Ar–Ar ages of leucogranite pegmatite are 19–14 Ma (Fu et al., 2018; Xie et al., 2017; Xie et al., 2018). Therefore, the activity time of the detachment zone of the dome is ~24–17 Ma (this study).

Yardo (Yalaxiangbo) dome (92°E)

The zircon and monazite U–Th–Pb ages of metamorphic rocks in the Yardo dome are 18–15 Ma (Chen et al., 2018; Wang et al., 2018).

The ages of synkinematic deformed leucogranite sills are 21–18 Ma (Wang et al., 2018; Yan et al., 2012), and the age of the undeformed two-mica granite is 17 Ma (Wang et al., 2018). The amphibole Ar–Ar age is 18 Ma, and the muscovite Ar–Ar ages of leucogranite and schist are 14–13 Ma (Yan et al., 2012). Recently, Dong et al. (2019) conducted a more detailed study on the deformation time of the detachment fault. The zircon U–Pb ages of the leucogranite lenses affected by the detachment fault in the Yardoi dome are 20–16 Ma, indicating that the activity time of the STDS is earlier than 20 Ma; the muscovite and biotite Ar–Ar ages are 14–13 Ma, indicating that the activity lasted until ~13 Ma. Therefore, the STDS activity time of the Yardoi dome is ~21–17 or until 13 Ma.

Ramba dome (90° 5'E)

The Ramba dome is close to the IYZS, and its east side is cut by the Yadong–Gulu rift fault (NSTR). The zircon rim U–Pb age of granitic gneiss representing the metamorphic age is 28 Ma; the zircon, monazite, and xenotime U–Pb ages of the undeformed mica granite are 8–7 Ma (Liu et al., 2014; Ratschbacher et al., 2011), and the muscovite and biotite Ar–Ar ages of granite are 6 Ma (Guo, Zhang, & Zhang, 2008). It is speculated that the metamorphic age (28 Ma) of the gneiss represents the initial age of doming (i.e., the STDS). However, its younger (8–7 Ma) undeformed leucogranite formed after STDS activity and is related to the NSTR activity under east–west extension (Ratschbacher et al., 2011).

Kangmar dome (89° 40'E)

The U–Th–Pb ages of monazite from metamorphic rocks in the Kangmar dome are 20–14 Ma (Stearns et al., 2013) and record the time of dome exhumation. The muscovite and biotite Ar–Ar ages in the Kangmar detachment zone are 15–11 Ma (Lee et al., 2000; Maluski, Matte, Brunal, & Xiao, 1988). Therefore, the STDS activity time represented by the Kangmar detachment fault is ~20–15 Ma.

Kampa dome (88° 50'E)

The U–Th–Pb ages of monazite and xenotime in granitic gneiss and deformed leucogranite in the Kampa dome are 29–23 Ma (Lin et al., 2020; Liu et al., 2016). The biotite and muscovite Ar–Ar ages of metamorphic rocks (pelite, marble, and slate) are 16–14 Ma (Quigley et al., 2006). Therefore, the activity time of the STDS in the Kampa dome may be ~27–14 Ma.

Mabja–Sakya–Kude domes (87° 50'E–88° 30'E)

The zircon U–Pb ages of metamorphic rocks in the Mabja–Sakya–Kude dome are 23–22 Ma (Lee & Whitehouse, 2007), and the monazite U–Th–Pb ages are 29–19 Ma (Stearns et al., 2013). Corresponding to the metamorphic ages of metamorphic rocks, the zircon and monazite U–Th–Pb ages of deformed leucogranites are 28–23 (King, Harris, Argles, Parrish, & Zhang, 2011), 28 (Zhang et al., 2004; Zhang, Harris, Parrish, Zhang, & Zhao, 2004), and 23 Ma (Lee et al., 2006).

The zircon–monazite–xenotime U–Pb ages of the undeformed leucogranites in the Mabja–Sakya–Kude dome are 16 (Lee & Whitehouse, 2007), 15–9 (King et al., 2007; King et al., 2011), 15–14 (Lee et al., 2006), 14 (Zhang, Harris, Parrish, Kelley, et al., 2004; Zhang,

Harris, Parrish, Zhang, & Zhao, 2004), and 11–10 Ma (Schärer, Xu, & Allègre, 1986).

The Ar–Ar ages of muscovite and biotite in the Mabja–Sakya–Kude dome are relatively young at 17–13 (Lee et al., 2006), 14–8 (King et al., 2011), 12–10 (Zhang, Harris, Parrish, Kelley, et al., 2004), and 9–6 Ma (Maluski et al., 1988). The Mabja dome area, located northeast of the Ama Drime Massif, is also cut by NSTR, so the late 15–8 Ma leucogranite veins and Ar–Ar ages of mica may be related to east–west extensional activity. In conclusion, the activity time of the STDS in the Mabja dome is 29–16 Ma.

Lagoi Kangri dome (87° 35'E)

Studies on the Lagoi Kangri dome are relatively rare. The monazite U–Th–Pb age of leucogranite is 16–15 Ma (Schärer et al., 1986), and the mica Ar–Ar age is 12–11 Ma (Maluski et al., 1988).

Ama Drime Massif (87° 30'E)

The Ar–Ar age of amphibolite in the GHC in the Ama Drime Massif is 25 Ma (Hodges et al., 1994), and the monazite U–Pb ages in the stage of isothermal decompression in the course of retrograde metamorphism are 30–19 Ma (Wang et al., 2017), which represent the beginning of exhumation and denudation of the GHC, that is, the time when the STDS may have started to be active is 30–19 Ma. The younger middle Miocene K-feldspar and mica Ar–Ar ages (15–10 Ma) and monazite and zircon U–Th–Pb ages (15–11 Ma) in this area (Cottle et al., 2009; Hodges et al., 1994; Kali et al., 2010; Kellett, Cottle, & Smit, 2014; Leloup et al., 2010; Liu et al., 2007; Wang, Zhang, Zhang, & Wei, 2017; Zhang & Guo, 2007) may be related to the activity of NSTR (Kharta and Dinggye rifts or Ama Drime and Nyönno Ri detachments). The late Miocene fast exhumation of the Ama Drime was affected by the east–west extension (Kali et al., 2010).

Xiaru dome (86° 15'E)

The Xiaru dome, like the Ramba dome, is close to the IYZS. However, research on the metamorphism and deformation of the Xiaru dome is very scarce, and only some studies on leucogranite have been published. The zircon and monazite U–Th–Pb ages of garnet–tourmaline-bearing leucogranite in the core of the Xiaoru dome are 36–34 Ma (Liu, Wu, Ding, et al., 2016), and the zircon U–Pb age of tourmaline-bearing leucogranite is 29 Ma (Gao et al., 2016).

Malashan–Cuobu–Paiku Co domes (85° 10'E–85° 50'E)

The leucogranite of the Malashan dome has been studied in detail, but the formation mechanism of the dome is relatively unknown. Some scholars thought that the metamorphic rocks in the Malashan dome represent the contact metasomatism associated with magma intrusion (Aoya et al., 2005). The zircon and monazite U–Th–Pb ages of the leucogranites in the Malashan–Cuobu–Paiku Co area are as follows: 28 (Gao et al., 2016), 28 and 20 (Gao et al., 2013), 22–16 (Kawakami et al., 2007), 19–18 (Aoya et al., 2005), 18–17 (Gao & Zeng, 2014), and 17 Ma (Zhang et al., 2012). The mica Ar–Ar ages are 17–16 (Zhang et al., 2012), 16 (Kawakami et al., 2007), and 16–15 (Aoya et al., 2005). According to the age of the leucogranite

mentioned above, the time of detachment fault activity in the Malashan dome area is estimated to be 28–15 Ma.

Changgo–Kuang Tang domes (84°20'E–85°E)

Larson et al. (2010) conducted a very detailed study on the Changgo–Kuang Tang dome. The zircon U–Pb age of the main body of the deformed leucogranite in Changgo dome is 24 Ma, and the mica Ar–Ar ages are 19–17 Ma. The main phase of the Changgo leucogranite is cut by undeformed aplite dikes, but the aplite dikes are strained within the STDS. The monazite U–Th–Pb age of the aplite dikes is 22 Ma, and the muscovite Ar–Ar age is 19 Ma in the STDS. The muscovite Ar–Ar age of pelitic schist is 18 Ma; the muscovite Ar–Ar age of a quartz vein at the bottom of the THS is 21 Ma. The zircon U–Pb age of the deformed leucogranite affected by the doming of Kuang Tang is 20 Ma and that of the undeformed leucogranite is 17–16 Ma. Therefore, the active time of the detachment zone in the Changgo–Kuang Tang dome is ~24–18 Ma.

Gurla Mandhata–Xiao Gurla domes (81°20'E)

The Gurla Mandhata dome separates the GHC and THS along with the Gurla Mandhata detachment system (GMDS), recording the early southward extended detachments related to STDS activity and the late orogen-parallel (west–east trending) extended deformation related to NSTR activity (Nagy, Godin, Antolín, Cottle, & Archibald, 2015).

The zircon U–Pb ages of leucogranites in the Gurla Mandhata–Xiao Gurla area are 20–15 Ma (Pullen et al., 2011). The monazite U–Th–Pb ages and muscovite Ar–Ar ages are 19–15 and 13–10 Ma, respectively. The early ages represent the activity of the STDS, and the late ages are NSTR; therefore, the transition time between them is 15–13 Ma (Nagy et al., 2015). Xu et al. (2013) analysed the metamorphic rocks in the dome affected by E–W strike-slip shear and obtained zircon U–Pb ages of 22–15 Ma. These ages may record the early activity of the GMDS (Nagy et al., 2015). Murphy et al. (2002) and Murphy and Copeland (2005) studied the deformation characteristics and ages of synkinematic dikes in the GMDS. The monazite Th–Pb ages are 15–7 Ma, and the muscovite Ar–Ar ages are 12–7 Ma. This interval (15–7 Ma) may be related to the late Karakoram strike-slip fault activity (McCallister, Taylor, Murphy, Styron, & Stockli, 2014). In conclusion, this study considers that the time range of detachment faults related to the STDS in the Gurla Mandhata–Xiao Gurla dome area is ~22–15 Ma.

Leo Pargil dome (78°40'E)

The GHC and THS of the Leo Pargil dome are separated by the Leo Pargil shear zone (LPSZ). The zircon U–Pb ages are 27–19 Ma (Leech, 2008), the garnet Sm–Nd age is 19 Ma (Thöni et al., 2012), and the monazite U–Th–Pb ages are 23–18 Ma (Langille et al., 2012) for the dome. More recently, a large number of U–Th–Pb ages of monazite in leucogranite from the Leo Pargil dome have been tested (Lederer, Cottle, Jessup, Langille, & Ahmad, 2013). The results show that the ages of foliated, boudinaged, and folded leucogranite sills in the dome are 30–23 Ma and that the ages of massive, crosscutting leucogranites in the dome are 23–18 Ma, which is consistent with the time of

decompression and melting (Jessup, Langille, Cottle, & Ahmad, 2016), showing that the initial extension time of the dome is 23 Ma. The age of synkinematic deformed leucogranites cutting the LPSZ at the edge of the dome is 20 Ma (Lederer et al., 2013), indicating that the LPSZ was still active at 20 Ma.

The muscovite Ar–Ar ages of the LPSZ from Thiede et al. (2006) and Hintersberger, Thiede, Strecker, and Hacker (2010) are 17–14 Ma, which are interpreted as the starting time of west–east extension. Therefore, it is suggested that the time range related to STDS extension in the Leo Pargil dome area may be ~23–18 Ma, and the starting time of NSTR extension may be 17–14 Ma.

Gianbul–Gumburanjon domes (77°E)

The GHC and THS in the Gianbul Gumburanjon dome are separated by the Miyar (or Khanjar) shear zone (MSZ) to the south and the Zanskar shear zone (ZSZ) to the north. The monazite U–Th–Pb age of migmatite at the bottom of the MSZ is 27 Ma (Robyr, Hacker, & Mattinson, 2006), which is interpreted as the starting time of extension for the detachment fault. The age of an undeformed leucogranite vein in the MSZ is 23 Ma (Robyr et al., 2006; Robyr, Epard, & El Korh, 2014), so the active time of the extensional detachment fault of the MSZ is 27–23 Ma. The ages of Gianbul dome migmatite and deformed pegmatite are 23–21 Ma, the age of undeformed pegmatite vein in ZSZ in the north is 21 Ma, and the mica Ar–Ar ages of leucogranite, schist, and gneiss in the Gianbul area are 22–20 Ma (Horton et al., 2015). The active time of extension and the detachment fault of the Gianbul dome can be limited to 27–20 Ma.

The ages of the metamorphosed leucogranites in Gumburanjon are 26–22 Ma (Finch et al., 2014), the U–Pb age of the undeformed leucogranite cutting the ZSZ is 22–21 Ma (Dézes, Vannay, Steck, Bussy, & Cosca, 1999; Finch et al., 2014; Walker et al., 1999), and the mica Ar–Ar ages of the undeformed leucogranites are 22–19 Ma (Dézes et al., 1999; Walker et al., 1999). The mica Ar–Ar age of the leucogranite is consistent with the zircon and monazite U–Pb ages, indicating that rapid uplift and denudation occurred shortly after the intrusion of leucogranite. Therefore, the extension and detachment time of ZSZ in the Gumburanjon dome is ~26–19 Ma. In conclusion, the extension and doming time of the Gianbul–Gumburanjon dome is 27–19 Ma.

5.3.2 | Inner STDS or the *strict sense* STDS between the GHC and THS

LZ–Khula Kangri–Gonto La (90–91°E)

In Gonto La valley–Khula Kangri mountain–LZ County, the 300-m-thick Gonto La detachment fault resulted in the deformation of the Khula Kangri leucogranite. The monazite $^{208}\text{Pb}/^{232}\text{Th}$ age of the granite under the Gonto La shear zone is 12.5 ± 0.4 Ma, which indicates that the activity of the STDS in this area lasted beyond 12.5 Ma (Edwards & Harrison, 1997). The mica Ar–Ar age of the Khula Kangri pluton is approximately 11–12 Ma (Guillot, Cosca, Allemand, & Le Fort, 1999; Maluski et al., 1988), which indicates that the rapid uplift and cooling age of the lower part of the STDS fault is 11 Ma.

However, this study considers that the age of the undeformed leucogranite cutting the bedding plane is approximately 13.6 Ma in LZ, so the ductile shear activity of the STDS in this area had ended before 13.6 Ma.

Wagya La–Masang Kang ($89^{\circ}50'E$)

The age of the deformed tourmaline-bearing leucogranite at the bottom of the Lingshi klippe is 14 Ma (Cooper, Hodges, Parrish, Roberts, & Horstwood, 2015). The GHC on the north side of the Lingshi klippe is intruded by 14 Ma deformed mylonitic two-mica granite (Montomoli, Carosi, Rubatto, Visonà, & Iaccarino, 2017). The monazite age of deformed leucogranite in Wagya La is 12–11 Ma (Kellett et al., 2009; Wu et al., 1998). The granulite-facies metamorphic age of eclogite on the south side of Masang Kang is 14 Ma (Grujic, Warren, & Wooden, 2011; Warren et al., 2011). These results show that there was obvious ductile deformation at approximately 14–11 Ma in the Lingshi area. However, the Lingshi area is affected not only by the activity of the inner STDS but also by the NE–SW-trending Yadong–Gulu rift and Lingshi–Masang Kang rift faults that formed after the STDS. Therefore, the ductile deformation of leucogranite and the rapid exhumation of eclogite in the inner STDS belt at 14–12 Ma in northern Bhutan (Gonto La–Khula Kangri–LZ–Wagya La–Masang Kang) may have been the result of the nearly east–west extension of NSTR (Carosi, Montomoli, Rubatto, & Visonà, 2006; Cooper et al., 2015; Xu et al., 2013). In addition, it may be the result of out-of-sequence thrusting along the later Kakhtang Fault (Kellett et al., 2009).

Yadong–Sikkim ($88^{\circ}E$ – $89^{\circ}30'E$)

The zircon U–Pb age of the Zherger-La high-pressure granulite in the north of Yadong is 17 Ma, which represents the age of exhumation and extrusion of the GHC (Gong et al., 2012). Liu et al. (2017) determined the zircon, monazite, and xenotime U–Pb geochronology of the undeformed leucogranite in the Yadong area, limiting the ductile shear activity along the STDS in the Yadong area to 20 Ma.

The zircon and monazite U–Th–Pb ages of the deformed leucogranite north of Sikkim are 17–15 Ma (Catlos, Dubey, Harrison, & Edwards, 2004), indicating that the deformation activity along the STDS in this area continued from 17 to approximately 15 Ma. Kellett, Grujic, Coutand, Cottle, and Mukul (2013) considered that the U–Th–Pb age of monazite enclosed by garnet in gneiss north of Sikkim (35–24 Ma) represents the prograde metamorphism (consistent with the prograde metamorphism of 26–23 Ma, Rubatto, Chakraborty, & Dasgupta, 2013); the U–Th–Pb ages of monazite in the matrix (24–13 Ma) indicate the retrograde stage. Combining zircon U–Pb ages (28.5–14 Ma) and the muscovite Ar–Ar age (13 Ma), Kellett et al. (2013) suggested that the activity time along the STDS north of Sikkim is 24–13 Ma.

Kharta–Ama Drime–Dinggye–Saer ($87^{\circ}30'E$ – $88^{\circ}E$)

The U–Th–Pb ages of monazites from the deformed and undeformed leucogranites in the Saer area on the east side of the Ama Drime Masif are 16 and 15 Ma, respectively (Leloup et al., 2010), representing the end of STDS activity between 16 and 15 Ma. According to the

interval of isothermal decompression (30–19 Ma, Wang, Wu, et al., 2017), it is speculated that the time of STDS ductile shear activity in the Saer area may have lasted from 30 to 16–15 Ma.

Rongbuk–Mount Everest–Makalu–Dzaka Chu ($86^{\circ}30'E$ – $87^{\circ}30'E$)

The research on the STDS in the Mount Everest area is more comprehensive (see review by Waters, Law, Searle, & Jessup, 2019), including the Qomolangma detachment at the top and the Lhotse detachment at the bottom. On Mount Everest and in Rongbuk Valley, the U–Th–Pb isotopes of zircon, monazite, and xenotime grains are used to define the age of the undeformed Rongbuk leucogranite as 22–19.5 Ma. The metamorphic age of the GHC during STDS activity is obtained from sphene U–Pb and hornblende Ar–Ar ages (20–19 Ma) for sillimanite-bearing metamorphic rocks, so Hodges et al. (1992) and Copeland, Parrish, and Harrison (1988) concluded that the time limits of STDS activity are 22–19 Ma. However, Hodges, Bowring, Davidek, Hawkins, and Krol (1998) suggested that Hodges et al. (1992) and Copeland et al. (1988) were wrong to obtain the age (22–19.5 Ma) of the Rongbuk leucogranite by analysing whole mineral U–Pb ages. The age of the undeformed Rongbuk leucogranite measured by mica Ar–Ar is 16.4 Ma (Hodges et al., 1998). Combined with the zircon, monazite, and xenotime U–Th–Pb ages of mylonitized granite sills (16.7 Ma), Hodges et al. (1998) limited the activity time along the STDS to 16.7–16.4 Ma.

All of the above researchers considered that the undeformed Rongbuk leucogranite cut the STDS, but new mapping results show that Hodges et al. (1992), Copeland et al. (1988), and Hodges et al. (1998) are all wrong. The Rongbuk leucogranite does not cut the STDS (Cottle et al., 2015; Murphy & Harrison, 1999). Under the STDS (top of the GHC) is a set of rocks containing a deformed mylonitic sill, a deflected dyke, and an undeformed crosscutting dyke. The monazite U–Th–Pb age of deformed leucogranites is 16.8–16.4 Ma, and the age of undeformed leucogranite is 15.6–15.4 Ma (Cottle et al., 2015; Murphy & Harrison, 1999; Searle, Simpson, Law, Parrish, & Waters, 2003).

The monazite U–Th–Pb ages of the deformed leucogranite sill and the undeformed leucogranite in the Kangshung valley area are 21 and 16.7 Ma, respectively (Cottle, Searle, et al., 2009); the monazite U–Th–Pb age of the undeformed granite dyke at the bottom of the STDS in the Dzaka Chu valley is 20 Ma (Cottle et al., 2007); the monazite U–Th–Pb age of the synkinematic to postkinematic leucogranite in Nuptse is 24 Ma (Jessup et al., 2008). The U–Pb and Ar–Ar ages of the late undeformed leucogranite in Namche Bazaar–Gokyo Ri–Fifth west of Everest indicate that its crystallization time is 18 Ma (Viskopic et al., 2005). In addition, Viskopic et al. (2005) thought that the isothermal decompression time of sillimanite-facies metamorphism (M2) in the Mount Everest area was 26.3–22.6 Ma. However, Cottle, Searle, et al. (2009) advanced the metamorphism time of the sillimanite stage to 28 Ma (28–22.6 Ma). The muscovite Ar–Ar ages in the Qomolangma Formation are 28–18 Ma (Corthouts, Lageson, & Shaw, 2016), which limit the time of STDS activity. The schist in the Rongbuk valley is affected by the activity along the STDS, and its monazite U–Th–Pb age (16.9 Ma) represents the ductile shear

time along the STDS (Searle et al., 2003). Therefore, the STDS activity time in Rongbuk–Mount Everest–Lhotse–Dzaka Chu should have been 28–17 Ma. This result is similar to that for Makalu, southeast of Mount Everest. In the Makalu area, the age of early deformed garnet tourmaline muscovite leucogranite is 24–21 Ma and that of late undeformed cordierite-bearing leucogranite is 16 Ma (Schärer et al., 1986; Streule, Searle, Waters, & Horstwood, 2010), implying that the initial age of STDS activity is greater than or equal to 24 Ma and that the end age is greater than 16 Ma.

It is worth noting that low-temperature chronology (such as AFT, AHe, and Ar–Ar) in the Mount Everest area suggests that the activity time of the STDS may have been as late as 13–12 Ma (Carrapa et al., 2016; Schultz, Hodges, Ehlers, van Soest, & Wartho, 2017), which may represent the time of brittle deformation along the STDS. The hydrogen isotopes of synkinematic biotite indicate that atmospheric precipitation had infiltrated into the footwall of the STDS along the porosity–permeability structure in Everest at 17–15 Ma (Gébelin et al., 2017). The Kung Co granite northwest of Everest is cut by NSTR while retaining the lineation of the east–west and north–south ductile shearing. Its zircon U–Pb age (Lee et al., 2011) indicates that it experienced the same period of E–W and N–S extension (Mitsuishi, Wallis, Aoya, Lee, & Wang, 2012) at 19 Ma. In conclusion, the transition time from ductile deformation (28–17 Ma) to brittle deformation (16–12 Ma) along the STDS in the Everest area is between 17 and 16 Ma.

Nyalam–Shisha Pangma–Gyirong (85°E–86°10'E)

According to Wang, Zhang, and Wang (2013) and Leloup et al. (2015), the M1 metamorphic interval of the GHC is 40–30 Ma. The ages of deformed leucogranites affected by ductile shear under the STDS are 27–17 Ma (Leloup et al., 2015; Liu et al., 2012; Schärer et al., 1986; Wang et al., 2016; Xu et al., 2013; Yang et al., 2019), and the ages of undeformed leucogranites are 16–14 Ma (Leloup et al., 2015; Wang, Zhang, & Wang, 2013). The initial fast denudation and cooling episode obtained by mica Ar–Ar ages from the GHC is 18–15 Ma (Leloup et al., 2015; Maluski et al., 1988; Wang et al., 2016; Wang, Li, & Qu, 2006). Therefore, the starting time of ductile shear along the STDS in Nyalam is 27–25 Ma, and the ending time of STDS activity is 17–15 Ma (Leloup et al., 2015; Wang et al., 2016).

The Shisha Pangma area lies 30 km to the west of Nyalam. The U–Pb age of the weakly foliated biotite granite under the STDS is 20 Ma, and the main body of the Shisha Pangma granite is undeformed. The U–Pb age and muscovite Ar–Ar age are both 17 Ma (Searle & Whitehouse, 1997), which indicates that rapid uplift and cooling occurred after the intrusion of the Shisha Pangma granite. At 17 Ma, the ductile shear activity along the STDS ended, and the starting age of STDS activity in the Shisha Pangma area was earlier than 20 Ma.

The crystallization ages of the deformed leucogranite affected by the STDS in the Gyirong area are 26–19 Ma (Wang, Zhang, Liu, Yan, & Wang, 2013; Yang et al., 2009; Zhang et al., 2012). The rapid exhumation obtained from the ages of detrital zircons and apatite fission-track dating in northern Gyirong is 18–15 Ma (Shen et al., 2016). In conclusion, 28–17 Ma can represent the time of ductile shear activity along the STDS in the Nyalam–Shisha Pangma–Gyirong area.

Dhaulagiri–Annapurna–Manaslu (83°30'E–84°E)

The monazite U–Th–Pb ages of the Manaslu leucogranite are 23–19 Ma (Copeland, Harrison, & Fort, 1990; Cottle, Lederer, & Larson, 2019; Harrison et al., 1999; Harrison, McKeegan, & LeFort, 1995), and the whole-rock Rb–Sr age of the Manaslu leucogranite is 18 Ma (Deniel, Vidal, Fernandez, Le Fort, & Peucat, 1987). The amphibole, muscovite, and biotite Ar–Ar ages of the Manaslu leucogranite and its surrounding metamorphic rocks are concentrated from 24 to 16 Ma (Copeland et al., 1990; Copeland et al., 1991; Godin, Gleeson, Searle, Ullrich, & Parrish, 2006; Guillot, Hodges, Fort, & Pêcher, 1994). These ages are interpreted as the cooling age after granite intrusion (Copeland et al., 1990), the denudation of normal faults on the north side of the Manaslu leucogranite (Guillot et al., 1994), or the fold age of the Annapurna Formation and the Chame detachment fault (Godin, Gleeson, et al., 2006). The monazite U–Th–Pb ages are 22 Ma for the deformed leucogranite and 18 Ma for the granite sill cutting the STDS (Coleman, 1998). According to the Ar–Ar ages in the Annapurna–Manaslu region (Coleman & Hodges, 1998), the activity time of the STDS is 22–18 Ma.

Walters and Kohn (2017) limited the activity of the STDS to 17 Ma by comparing the cooling rates and cooling times of the THS and GHC. Moreover, the Thakkhola rift on the west side of Annapurna cuts the STDS, and the muscovite Ar–Ar age in the north–south rift is 14 Ma (Coleman & Hodges, 1995), indicating that the STDS activity time is before 14 Ma.

In the lower Kali Gandaki Valley, the monazite U–Th–Pb ages of kyanite-bearing migmatitic paragneiss are 25–18 Ma (Iaccarino et al., 2015), and the sphene U–Pb age is 23 Ma (Mottram et al., 2019), which represents the time of decompressive melting of the GHC. In the Modi Khola valley (Corrie & Kohn, 2011; Martin et al., 2007), Budhi Gandaki (Larson, Cottle, & Godin, 2011) and Daraudi (Shrestha, Larson, Duesterhoeft, Soret, & Cottle, 2019) south of Manaslu, the GHC also has similar decompression melting ages (28–18 Ma, Larson & Cottle, 2015).

Therefore, the activity time of the STDS in the Dhaulagiri–Annapurna–Manaslu area is at least 22–17 Ma. It is worth noting that some researchers (Hodges et al., 1996) think that there were two alternations between shortening and extension in the Dhaulagiri–Annapurna–Manaslu area in the Miocene.

Bura Buri–Dolpo–Mugu (82°E–83°40'E)

The main body of the Bura Buri leucogranite is undeformed and intrudes into the top of the GHC and the bottom of the THS. Its zircon and monazite U–Th–Pb ages are 25–23 Ma. Carosi, Montomoli, Rubatto, and Visonà (2013) argued that the STDS activity in this area ended before 25–23 Ma. However, the margin of Bura Buri has weak deformation characteristics, and its age may be more representative of the starting time of the STDS. The Mugu leucogranite is located 20 km north of Bura Buri. The U–Th–Pb age of the Mugu leucogranite is 17.6 Ma (Harrison et al., 1999), and the mica Ar–Ar age is 17–15 Ma (Guillot et al., 1999). These results indicate that a cooling event of rapid uplift occurred after the Mugu granite intrusion, which may indicate that the STDS was still experiencing rapid activity at

文献作者名单有误。这段对原文理解有误。原文岩体的U–Pb和Ar–Ar年龄集中在19–17Ma，表明19–17Ma是快速折返或抬升的时间，因此STDS的活动时间为19–17Ma，更有可能持续到17之后？

17 Ma. The Mangri shear zone (i.e., the high Himalayan discontinuity, HHD) on the southwest side of the Mugu granite was thrust from 25 to 18 Ma (Montomoli, Iaccarino, Carosi, Langone, & Visonà, 2013). In conclusion, the activity time of the STDS in the Bura Buri-Dolpo-Mugu area may have been 25–17 Ma.

Shivling–Gangotri–Malari (79–80°E)

The Malari leucogranite is exposed at the top of the GHC and the bottom of the STDS in the Dhauliganga valley of the Garhwal area. Sachan, Kohn, Saxena, and Corrie (2010) believed that the Malari leucogranite has no deformation and that its zircon U–Pb age (19 Ma) can limit the end of STDS activity before 19 Ma. However, later geologists (Sen, Chaudhury, & Pfänder, 2015) found that the Malari leucogranite displays ductile deformation due to the influence of the STDS. The monazite U–Th–Pb age of this deformed leucogranite at the top of the GHC is 20–19 Ma (Iaccarino et al., 2017); the Ar–Ar ages of the Malari leucogranite and deformed and undeformed granite sills are 16.5–15 Ma (Montemagni et al., 2018; Sen et al., 2015). Therefore, the latest research results show that the activity time of the STDS in the Malari area is ~20–15 Ma.

Approximately 90 km northwest of Malari are the Shivling and Gango Tri deformed leucogranites, affected by STDS activity. The monazite U–Th–Pb age from the leucogranites is 23–22 Ma (Harrison, Lovera, & Grove, 1997; Searle, Noble, Hurford, & Rex, 1999). The results of fission-track dating of zircon and apatite and K–Ar and Ar–Ar ages of muscovite and biotite show that there is rapid cooling from 23 to 18 Ma and low cooling rates from 18 to 2 Ma (Searle et al., 1999; Sorkhabi, Stump, Foland, & Jain, 1996). These ages imply that the activity time of the STDS in Shivling and Gango Tri is ~23–18 Ma.

Manali–Sutlej–Peo (77°E–78°30'E)

The Kinnaur Kailash Early Ordovician (472 Ma) two-mica granite in the Peo area in the upper Sutlej valley, 100 km northwest of Gango Tri, has metamorphic ages of 26–21 Ma in zircon rims (Stübner et al., 2014), and the zircon age of deformed leucogranite is 18.5 Ma (Tripathi, Sen, & Dubey, 2012). The U–Pb ages of the matrix monazite in the metamorphic rocks at the bottom of the THS in the Morang area on the north side of Kinnaur Kailash are 30–22 Ma (Chambers et al., 2009). The muscovite Ar–Ar age at the bottom of the THS, 30 km northwest of Kinnaur Kailash and affected by ductile shear along the STDS, is 19–17 Ma (Vannay et al., 2004). The above information indicates that the time of STDS activity in this area is from 30 to 17 Ma.

In the Manali area in central Himachal Pradesh, the monazite U–Th–Pb ages in mica schist are 26–22 Ma, and the muscovite Ar–Ar age is 22 Ma (Stübner et al., 2014; Walker et al., 1999), which indicates that the high cooling rates of the GHC are related to the activity of the STDS in the early Miocene.

Umasi La–Haptal–Suru–Shafat (76°E–77°E)

The monazite U–Th–Pb ages from migmatitic schist in the Umasi La–Haptal–Suru–Shafat area at the bottom of the STDS (locally termed the Zanskar shear zone; Horton & Leech, 2013) are 27–17 Ma, and

the zircon and monazite U–Th–Pb ages of deformed leucogranite are 27–20 Ma (Horton & Leech, 2013; Noble & Searle, 1995). The activity time of the STDS is from 26 to 16 Ma (Inger, 1998) and 25–20 Ma (Searle, Waters, Rex, & Wilson, 1992; Vance, Ayres, Kelley, & Harris, 1998) by mica Rb–Sr and A–Ar dating of the GHC, respectively. In the Tapachan area southeast of the Zanskar shear zone, the activity time of the STDS defined by zircon and apatite fission-track dating is 22–19 Ma (Schlup et al., 2011). Therefore, the activity time of the STDS in the Zanskar area is 27–16 Ma.

5.3.3 | Outer STDS in klippe

Lingshi–Tang Chu–Shemgang–Ura–Sakteng klippe in Bhutan (89–92°E)

The prograde metamorphism and deformation times along the Main Central Thrust (MCT) in eastern Bhutan started at 22 Ma. And Daniel, Hollister, Parrish, and Grujic (2003) believed that channel flow occurred in the GHC in this area, so the northward extension and sliding of the STDS at the top of the GHC is consistent with the southward thrust timing of the MCT at the bottom of the GHC. That is, the prograde metamorphism age (22 Ma) of the MCT represents the initiation age of STDS extension.

There are obvious folds in the THS in the Tang Chu–Black Mountain (Shemgang) klippe in central Bhutan. Some undeformed leucogranites intrude and cut the THS stratigraphic foliation. Greenwood, Argles, Parrish, Harris, and Warren (2016) determined that the zircon U–Pb age of the undeformed granites is approximately 18 Ma. Therefore, the extension of STDS ended before 18 Ma.

The zircon U–Pb ages of the deformed leucogranite in the Lingshi klippe in western Bhutan and the Ura klippe in central Bhutan are 24.5–16.5 and 20.5–15.5 Ma, respectively (Kellett et al., 2009). Meanwhile, the monazite U–Th–Pb ages (27.2–15.9 Ma) in metamorphic rocks near the outer STDS zone in the Lingshi and Ura klippe are nearly the same as the zircon U–Pb age of the above-mentioned leucogranite (Kellett et al., 2010), indicating that the ductile shear associated with STDS extension lasted from 23 to approximately 16 Ma.

The deformation and metamorphism of the inner STDS in northern Bhutan were affected by the late Kakhtang out-of-sequence thrust, while the outer STDS at the bottom of the klippe in the front of the orogenic belt is representative of the early northward extension age of the whole Himalayan belt (Kellett & Grujic, 2012). Therefore, based on the above results, the starting and ending time range of STDS extension in Bhutan should be 25–16 Ma.

Kathmandu Klippe in Nepal (85–86°E)

He, Webb, Larson, Martin, and Schmitt (2015) considered that the strata in the Kathmandu klippe belong to the THS, and its south side is in contact with the LHS with the boundary along the STDS; the GHC is located between the THS and the LHS on the north side of the Kathmandu klippe. As a result, the STDS and the MCT merge at depth. The ages of the deformed granite affected by STDS extension

and the undeformed granite are 30.8–23.1 and 18.8–13.8 Ma, respectively, so the time range of STDS activity on the north side of Kathmandu is 23.1–18.8 Ma (He et al., 2015; Webb, Schmitt, He, & Weigand, 2011).

Dadeldhura–Karnali–Jajarkot Klippes in India And Nepal (80–83°E)

The Jajarkot klippe is located west of Nepal. The muscovite Ar–Ar ages of the THS formation in the upper part of the STDS are 28–19 Ma, and the monazite U–Th–Pb ages of the metamorphic rocks in the STDS ductile shear zone are 27–23 Ma (Soucy La Roche, Godin, Cottle, & Kellett, 2019). Therefore, the activity time of the outer STDS in the Jajarkot klippe area is 27–19 Ma.

The Karnali klippe is located on the west side of the Jajarkot klippe. The monazite U–Th–Pb age in the STDS shear zone indicates that the initiation time of ductile shear associated with northward extension is 30 Ma, and the muscovite Ar–Ar age is 19 Ma (Soucy La Roche et al., 2016). Meanwhile, the monazite U–Th–Pb age of the GHC at the bottom of the Karnali klippe indicates that retrograde metamorphism of the GHC began at 30 Ma (Soucy La Roche et al., 2018). Therefore, the extension time of the outer STDS ductile shear zone represented by the Karnali klippe is 30–19 Ma.

The Dadeldhura klippe is located on the west side of the Karnali klippe. Antolín, Godin, Wemmer, and Nagy (2013) analysed the muscovite Ar–Ar ages (23–17 Ma) of the metamorphic rocks affected by the ductile shear of the outer STDS. He, Webb, Larson, and Schmitt (2016) determined the zircon U–Pb age of a postkinematic granite sill cutting the outer STDS as 17–14 Ma. Therefore, the outer STDS extended northward under the Dadeldhura klippe at 22–17 Ma.

However, north of the Dadeldhura klippe, the muscovite Ar–Ar age of the inner STDS (hinterland) in the Chainpur area is 12–11 Ma (Robinson, DeCelles, & Copeland, 2006), which is nearly the same as the active age of the inner STDS in the Wagya La–Masang Kang–Gonto La–Khula Kangri–LZ area; both of these ages are younger than that of the outer STDS in the foreland area. The activity of the inner STDS at 12–11 Ma in the Chainpur area may be related to the out-of-sequence thrusting of the Ramgarh Fault (Robinson, 2008).

In this study, it is found that in LZ, KJ, and CND, the oldest granites affected by ductile shear along the STDS are 25–23 Ma (Table 1, Figure 7), indicating that by at least 25 Ma, the STDS in these three places had begun to move. Combining this information with the results from other regions mentioned above, the duration of STDS northward extension across the whole Himalaya region is approximately 28–17 Ma (Figure 14), which corresponds to the Neohimalayan sillimanite metamorphism (M2) of the GHC. However, in some areas, the timing of the end of STDS activity is slightly different; for example, the time of the end of activity along the inner STDS in the hinterland is 14–11 Ma. More evidence shows that the late Miocene activity of the inner STDS is related to the out-of-sequence thrusting of faults such as the Kakhtang and Ramgarh thrusts.

5.4 | Extrusion and exhumation of the GHC

5.4.1 | Model comparison of the extrusion and exhumation of the GHC

The GHC is surrounded by the STDS in the upper part and by the MCT in the lower part. Many different models have been proposed to explain the exhumation and extrusion of the GHC and the activity along the STDS and MCT. The main models are as follows.

Gravity-driven collapse

According to this model, the activity of the STDS is caused by the gravitational instability of thickened crust in the orogenic belt (Figure 15a). The slip surface is a pre-existing weak lithological surface. There are two triggering factors for the northward sliding of the STDS (Searle, 2010): One factor is the decrease in compressive stress, which is caused by a decrease in the convergence velocity or in the subduction angle; the other factor is the decrease in crustal strength, which is mainly caused by the remelting of thickened crust.

Wedge extrusion

This model considers that the thickened crust of the Qinghai–Tibetan Plateau produces gravity loading (Figure 15b), which results in the remelting of the thickened root zone (Indian crust) and the formation of plastic deformation bodies. Driven by gravity loading, the plastic body is wedge-shaped and extruded southward along the STDS and MCT (Burchfiel et al., 1992; Grujic et al., 1996). That is, the GHS is a downward-thinning wedge, extruding southward from two low-grade metamorphic rocks. However, the seismic interpretation of the INDEPTH project did not find the intersection of the MCT and the STDS at depth (Nelson et al., 1996).

Channel flow

In this model, continental collision and convergence lead to the thickening of the crust, the accumulation of radiative heat, and the addition of a large amount of fluids. At the same time, possible lithospheric mantle detachment leads to the rise of asthenospheric materials, coupled with the strain heat energy of large structures, resulting in the partial remelting of the thickened middle crust. The remelted crustal materials flow laterally through accumulation and compression, forming tunnel flow (Godin, Gleeson, et al., 2006; Godin, Grujic, et al., 2006; Figure 15c). At the edge of the plateau, the height difference is largest, and climatic denudation is strongest, which leads to the emergence and exhumation of the partially remelted middle crust. The upper and lower boundaries of the outcrops are the STDS and the MCT, respectively. The GHS is material from the middle lower crust in the melting orogenic belt, which flows southward under the gravity of doubly thickened crust. Due to the concentrated denudation caused by a large amount of precipitation on the southern slope of the Himalayas, the tunnel flow material moves out to the surface through two ductile shear zones (the STDS to the north and the MCT to the south).

Tectonic wedging (Wedge insertion)

This model suggests that the northward movement of the THS along the STDS does not represent north–south extension but is the result of reverse thrusting of the hanging wall of the MCT (Figure 15d). The STDS is connected to the GCT thrust system in the north and to the MCT in the south. The northward thrusting of the GCT pushes the THS rocks over the Lhasa Plate and IYZS in the north. This model is based on the discovery that the MCT and STDS merge into a fault at the front of the orogenic belt (Webb et al., 2011; Webb et al., 2017).

In-sequence shearing

This model considers that there are two tectono-metamorphic discontinuities between the MCT and the STDS (Carosi, Montomoli, & Iaccarino, 2018; Carosi, Montomoli, Iaccarino, & Visonà, 2018). The southward thrusting of the Himalayas starts from the STDS at the top (45–28 Ma), and a series of rocks gradually thrusts southward, that is, the thrusting moves towards the MCT at the bottom gradually. The thrusting activity of the STDS begins earlier than that of shear zone (41–30 Ma) with south-vergent thrusting in the middle-upper part of the GHC, and thrusting in the middle-upper part of the GHC occurs earlier than that along the HHD (26–18 Ma) in the middle to lower part of the GHC. The HHD is earlier than that of MCT (17–13 Ma) at the bottom of the GHC.

According to the regional research results for the STDS and this study, the activity time of the STDS is 28–17 Ma, which is earlier than that of the MCT (19.8–8.5 Ma; Goscombe et al., 2018). The channel flow, wedge extrusion, and tectonic wedging models all require that the activity times along the STDS and MCT be consistent (Montomoli et al., 2013). This requirement is not consistent with the results of this study. Increasingly more recent studies show that the GHC is not a complete whole but is divided into the GHC_{upper} and GHC_{lower} by the HHD (Goscombe et al., 2018; Waters, 2019). Previous studies on the activity time of the HHD have shown that the time of HHD activity is 28–17 (Carosi, Montomoli, & Iaccarino, 2018; Carosi, Montomoli, Iaccarino, & Visonà, 2018) or 25–16 Ma (Goscombe et al., 2018; Wang, Rubatto, & Zhang, 2015). The activity time of the STDS is identical to that of the HHD but earlier than that of the MCT. Therefore, this paper considers that a sequential shearing model can better explain the GHC exhumation process in the study area.

5.4.2 | In-sequence shearing tectonic model, evolution of the STDS and exhumation of the GHC in the Himalayas

In this study, it is outlined that the STDS has a two-stage evolution model, that is, from 45 to 28 Ma, the STTS (predecessor of the STDS) thrusts southward, and from 28 to 17 Ma, the STDS extends northward, corresponding to kyanite metamorphism (M1) and sillimanite metamorphism (M2) in the GHC, respectively. On the basis of previous studies (Carosi, Montomoli, & Iaccarino, 2018; Goscombe et al., 2018; Imayama et al., 2012), combined with the thrusting time and kinematic characteristics of the HHD and MCT in the south, as well as the dome formation time of the NHGD in the north and the stretching

time and structural kinematic characteristics of the STDS, this paper considers that the study area is dominated by in-sequence shearing or thrusting and that at a later time in the area, there was out-of-sequence thrusting. The extrusion evolution of the GHC in the study area is divided into three stages (Figure 16).

In the early stage (45–28 Ma), the STTS at the top of the GHC was thrust, the THS was folded and faulted, the $GHC_{upper + lower}$ was buried deep, and kyanite metamorphism (M1) occurred in the GHC (Figure 16a). In the middle stage (27–21 Ma), the HHD in the middle of the GHC was thrust, the STDS was extended in the north–south direction, the NHGD (such as the Yardoi and CND domes) was formed in the middle of the THS, the GHC_{upper} was exhumed, and the GHC_{lower} continued to be deeply buried. The sillimanite metamorphism (M2) occurred in the GHC (Figure 16b). In the later stage (20–9 Ma), the MCT thrust at the bottom of the GHC, resulting in the extension along the STDS and HHD, the east–west extension of the THS, the exhumation of the $GHC_{upper + lower}$, and the deep burial and shallow metamorphism of the LHS (Figure 16c). Out-of-sequence thrusting occurred in some areas, forming the klippe of the THS in the front zone.

6 | CONCLUSIONS

1. The oldest synkinematic leucogranite affected by the STDS is the Lz leucogranite, with an age of 24–25 Ma, so the initial activity time of the STDS is equivalent to or slightly earlier than 25 Ma.
2. The youngest synkinematic leucogranite affected by the STDS is the CND leucogranite with an age of 18.4 Ma; and the oldest postkinematic leucogranite unaffected by the STDS is the XZ leucogranite with an age of 17.4 Ma. Therefore, the end of STDS activity is between 18.4 and 17.4 Ma.
3. The eastern Himalayas are affected by the Tsona north–south rift among the NSTR. The youngest leucogranite affected by NSTR is the KJ leucogranite with an age of 16.9–16.5 Ma. Therefore, the starting time of NSTR can be limited to 16 Ma.
4. At 45–28 Ma, the THS is thrust southward along the STTS, and at 28–17 Ma, the THS extends northward along the STDS.
5. The GHC is exhumed southward by in-sequence thrusting. The first event is the STTS (predecessor of the STDS) thrusting southward at 45–28 Ma, the second episode is the HHD thrusting southward at 28–17 Ma, and the last occurrence is the MCT thrusting southward at 17–9 Ma.

ACKNOWLEDGEMENTS

We are grateful to the two anonymous reviewers and Executive Editor, Prof. M. Santosh for their constructive comments. This work is also benefited from discussions with Wu Jian-Yang, Dong Lei, Gao Ke, Li Ying-Xu, Qin Cheng-Shi, Huang Han-Xiao, Liu Hong and Lu Liu.

CONFLICT OF INTEREST

The authors declare that we have no financial interests and personal relationships with other people or organizations that can inappropriately influence the work reported in this paper.

ORCID

Hua-Wen Cao  <https://orcid.org/0000-0002-3703-5843>

Zhi Zhang  <https://orcid.org/0000-0002-0947-0290>

Yong Huang  <https://orcid.org/0000-0003-4939-3493>

Zuo-Wen Dai  <https://orcid.org/0000-0002-9231-241X>

Qiu-Ming Pei  <https://orcid.org/0000-0003-4600-1511>

REFERENCES

- Aikman, A. B., Harrison, T. M., & Hermann, J. (2012). Age and thermal history of Eo- and Neohimalayan granitoids, eastern Himalaya. *Journal of Asian Earth Sciences*, 51, 85–97. <https://doi.org/10.1016/j.jseaeas.2012.01.011>
- Aikman, A. B., Harrison, T. M., & Lin, D. (2008). Evidence for early (>44 Ma) Himalayan crustal thickening, Tethyan Himalaya, southeastern Tibet. *Earth and Planetary Science Letters*, 274(1–2), 14–23 <https://doi.org/10.1016/j.epsl.2008.06.038>
- Antolín, B., Appel, E., Montomoli, C., Dunkl, I., Ding, L., Gloaguen, R., & El Bay, R. (2011). Kinematic evolution of the eastern Tethyan Himalaya: Constraints from magnetic fabric and structural properties of the Triassic flysch in SE Tibet. *Geological Society, London, Special Publications*, 349(1), 99–121 <https://doi.org/10.1144/SP349.6>
- Antolín, B., Godin, L., Wemmer, K., & Nagy, C. (2013). Kinematics of the Dadeldhura klippe shear zones (W Nepal): Implications for the foreland evolution of the Himalayan metamorphic core. *Terra Nova*, 25(4), 282–291 <https://doi.org/10.1111/ter.12034>
- Aoya, M., Wallis, S. R., Terada, K., Lee, J., Kawakami, T., Wang, Y., & Heizler, M. (2005). North-south extension in the Tibetan crust triggered by granite emplacement. *Geology*, 33(11), 853–856 <https://doi.org/10.1130/g21806.1>
- Braden, Z., Godin, L., & Cottle, J. M. (2017). Segmentation and rejuvenation of the greater Himalayan sequence in western Nepal revealed by in situ U–Th/Pb monazite petrochronology. *Lithos*, 284–285, 751–765 <https://doi.org/10.1016/j.lithos.2017.04.023>
- Burchfiel, B. C., Chen, Z., Hodges, K. V., Liu, Y., Royden, L. H., Deng, C., & Xu, J. (1992). The south Tibetan detachment system, Himalayan orogen: Extension contemporaneous with and parallel to shortening in a collisional mountain belt. *Geological Society of America Special Papers*, 269, 1–41 <https://doi.org/10.1130/SPE269-p1>
- Burg, J.-P., & Bouilhol, P. (2019). Timeline of the South-Tibet–Himalayan belt: The geochronological record of subduction, collision, and underthrusting from zircon and monazite U–Pb ages. *Canadian Journal of Earth Sciences*, 56(12), 1318–1332 <https://doi.org/10.1139/cjes-2018-0174>
- Cao, H. W., Huang, Y., Li, G. M., Zhang, L. K., Wu, J. Y., Dong, L., ... Lu, L. (2018). Late Triassic sedimentary records in the northern Tethyan Himalaya: Tectonic link with greater India. *Geoscience Frontiers*, 9(1), 273–291 <https://doi.org/10.1016/j.gsf.2017.04.001>
- Cao, H.-W., Zhang, Y.-H., Santosh, M., Li, G.-M., Hollis, S. P., Zhang, L.-K., ... Duan, Z.-M. (2019). Petrogenesis and metallogenic implications of Cretaceous magmatism in Central Lhasa, Tibetan plateau: A case study from the Lunggar Fe skarn deposit and perspective review. *Geological Journal*, 54(4), 2323–2346 <https://doi.org/10.1002/gj.3299>
- Cao, H.-W., Zou, H., Bagas, L., Zhang, L.-K., Zhang, Z., & Li, Z.-Q. (2019). The Laqiong Sb–Au deposit: Implications for polymetallic mineral systems in the Tethys–Himalayan zone of southern Tibet, China. *Gondwana Research*, 72, 83–96 <https://doi.org/10.1016/j.gr.2019.02.010>
- Carosi, R., Montomoli, C., & Iaccarino, S. (2018). 20 years of geological mapping of the metamorphic core across Central and Eastern Himalayas. *Earth-Science Reviews*, 177, 124–138 <https://doi.org/10.1016/j.earscirev.2017.11.006>
- Carosi, R., Montomoli, C., Iaccarino, S., & Visonà, D. (2018). Structural evolution, metamorphism and melting in the Greater Himalayan Sequence in Central-Western Nepal. *Geological Society, London, Special Publications*, 483, 305–323 <https://doi.org/10.1144/sp483.3>
- Carosi, R., Montomoli, C., Langone, A., Turina, A., Cesare, B., Iaccarino, S., ... Rai, S. M. (2015). Eocene partial melting recorded in peritectic garnets from kyanite–gneiss, Greater Himalayan Sequence, Central Nepal. *Geological Society, London, Special Publications*, 412, 111–129 <https://doi.org/10.1144/sp412.1>
- Carosi, R., Montomoli, C., Rubatto, D., & Visonà, D. (2006). Normal-sense shear zones in the core of the higher Himalayan Crystallines (Bhutan Himalaya): Evidence for extrusion? *Geological Society, London, Special Publications*, 268, 425–444 <https://doi.org/10.1144/gsl.sp.2006.268.01.20>
- Carosi, R., Montomoli, C., Rubatto, D., & Visonà, D. (2010). Late Oligocene high-temperature shear zones in the core of the higher Himalayan Crystallines (lower Dolpo, western Nepal). *Tectonics*, 29(4), 509–530 <https://doi.org/10.1029/2008TC002400>
- Carosi, R., Montomoli, C., Rubatto, D., & Visonà, D. (2013). Leucogranite intruding the south Tibetan detachment in western Nepal: Implications for exhumation models in the Himalayas. *Terra Nova*, 25(6), 478–489 <https://doi.org/10.1111/ter.12062>
- Carrapa, B., Robert, X., DeCelles, P. G., Orme, D. A., Thomson, S. N., & Schoenbohm, L. M. (2016). Asymmetric exhumation of the Mount Everest region: Implications for the tectono-topographic evolution of the Himalaya. *Geology*, 44(8), 611–614 <https://doi.org/10.1130/g37756.1>
- Catlos, E. J., Dubey, C. S., Harrison, T. M., & Edwards, M. A. (2004). Late Miocene movement within the Himalayan Main central thrust shear zone, Sikkim, north-East India. *Journal of Metamorphic Geology*, 22(3), 207–226 <https://doi.org/10.1111/j.1525-1314.2004.00509.x>
- Catlos, E. J., Harrison, T. M., Manning, C. E., Grove, M., Rai, S. M., Hubbard, M. S., & Upreti, B. N. (2002). Records of the evolution of the Himalayan orogen from in situ Th–Pb ion microprobe dating of monazite: Eastern Nepal and western Garhwal. *Journal of Asian Earth Sciences*, 20(5), 459–479 [https://doi.org/10.1016/S1367-9120\(01\)00039-6](https://doi.org/10.1016/S1367-9120(01)00039-6)
- Chambers, J., Caddick, M., Argles, T., Horstwood, M., Sherlock, S., Harris, N., ... Ahmad, T. (2009). Empirical constraints on extrusion mechanisms from the upper margin of an exhumed high-grade orogenic core, Sutlej valley, NW India. *Tectonophysics*, 477(1–2), 77–92. <https://doi.org/10.1016/j.tecto.2008.10.013>
- Chambers, J., Parrish, R., Argles, T., Harris, N., & Horstwood, M. (2011). A short-duration pulse of ductile normal shear on the outer south Tibetan detachment in Bhutan: Alternating channel flow and critical taper mechanics of the eastern Himalaya. *Tectonics*, 30(2), TC2005 <https://doi.org/10.1029/2010TC002784>
- Chen, J., Carosi, R., Cao, H., Montomoli, C., Iaccarino, S., Langone, A., & Li, G. (2018). Structural setting of the yalaxiangbo dome, SE Tibet (China). *Italian Journal of Geosciences*, 137(2), 330–347 <https://doi.org/10.3301/IJG.2018.18>
- Coleman, M., & Hodges, K. (1995). Evidence for Tibetan plateau uplift before 14 Myr ago from a new minimum. *Nature*, 374, 49–52 <https://doi.org/10.1038/374049a0>
- Coleman, M. E. (1998). U–Pb constraints on Oligocene–Miocene deformation and anatexis within the Central Himalaya, Marsyandi Valley, Nepal. *American Journal of Science*, 298(7), 553–571 <https://doi.org/10.2475/ajs.298.7.553>
- Coleman, M. E., & Hodges, K. V. (1998). Contrasting Oligocene and Miocene thermal histories from the hanging wall and footwall of the south Tibetan detachment in the central Himalaya from ⁴⁰Ar/³⁹Ar thermochronology, Marsyandi Valley, Central Nepal. *Tectonics*, 17(5), 726–740 <https://doi.org/10.1029/98TC02777>
- Cooper, F. J., Hodges, K. V., Parrish, R. R., Roberts, N. M. W., & Horstwood, M. S. A. (2015). Synchronous N–S and E–W extension at the Tibet-to-Himalaya transition in NW Bhutan. *Tectonics*, 34(7), 1375–1395 <https://doi.org/10.1002/2014TC003712>

- Copeland, P., Harrison, T. M., & Fort, P. L. (1990). Age and cooling history of the Manaslu granite: Implications for Himalayan tectonics. *Journal of Volcanology and Geothermal Research*, 44(1–2), 33–50 [https://doi.org/10.1016/0377-0273\(90\)90010-D](https://doi.org/10.1016/0377-0273(90)90010-D)
- Copeland, P., Harrison, T. M., Hodges, K. V., Maruélol, P., Le Fort, P., & Pecher, A. (1991). An early Pliocene thermal disturbance of the main central thrust, Central Nepal: Implications for Himalayan tectonics. *Journal of Geophysical Research: Solid Earth*, 96(B5), 8475–8500 <https://doi.org/10.1029/91JB00178>
- Copeland, P., Parrish, R. R., & Harrison, T. M. (1988). Identification of inherited radiogenic Pb in monazite and its implications for U–Pb systematics. *Nature*, 333, 760 <https://doi.org/10.1038/333760a0>
- Corrie, S. L., & Kohn, M. J. (2011). Metamorphic history of the central Himalaya, Annapurna region, Nepal, and implications for tectonic models. *Geological Society of America Bulletin*, 123(123), 1863–1879 <https://doi.org/10.1130/B30376.1>
- Corthouts, T. L., Lageson, D. R., & Shaw, C. A. (2016). Polyphase deformation, dynamic metamorphism, and metasomatism of Mount Everest's summit limestone, east central Himalaya, Nepal/Tibet. *Lithosphere*, 8(1), 38–57 <https://doi.org/10.1130/L473.1>
- Cottle, J., Lederer, G., & Larson, K. (2019). The monazite record of pluton assembly: Mapping Manaslu using Petrochronology. *Chemical Geology*, 530, 119309 <https://doi.org/10.1016/j.chemgeo.2019.119309>
- Cottle, J. M., Jessup, M. J., Newell, D. L., Horstwood, M. S., Noble, S. R., Parrish, R. R., ... Searle, M. P. (2009). Geochronology of granulitized eclogite from the Ama Drime massif: Implications for the tectonic evolution of the south Tibetan Himalaya. *Tectonics*, 28(1), TC1002 <https://doi.org/10.1029/2008TC002256>
- Cottle, J. M., Jessup, M. J., Newell, D. L., Searle, M. P., Law, R. D., & Horstwood, M. S. A. (2007). Structural insights into the early stages of exhumation along an orogen-scale detachment: The south Tibetan detachment system, Dzakaa Chu section, Eastern Himalaya. *Journal of Structural Geology*, 29(11), 1781–1797 <https://doi.org/10.1016/j.jsg.2007.08.007>
- Cottle, J. M., Searle, M. P., Horstwood, M. S. A., & Waters, D. J. (2009). Timing of midcrustal metamorphism, melting, and deformation in the Mount Everest region of southern Tibet revealed by U (–Th)–Pb geochronology. *The Journal of Geology*, 117(6), 643–664 <https://doi.org/10.1086/605994>
- Cottle, J. M., Searle, M. P., Jessup, M. J., Crowley, J. L., & Law, R. D. (2015). Rongbuk re-visited: Geochronology of leucogranites in the footwall of the south Tibetan detachment system, Everest region, southern Tibet. *Lithos*, 227, 94–106 <https://doi.org/10.1016/j.lithos.2015.03.019>
- Crouzet, C., Dunkl, I., Paudel, L., Árkai, P., Rainer, T. M., Balogh, K., & Appel, E. (2007). Temperature and age constraints on the metamorphism of the Tethyan Himalaya in Central Nepal: A multidisciplinary approach. *Journal of Asian Earth Sciences*, 30(1), 113–130 <https://doi.org/10.1016/j.jseaes.2006.07.014>
- Dai, Z., Dong, L., Li, G., Huizenga, J.M., Ding, J., Zhang, L., ... Yan, G. (2020). Crustal thickening prior to 43 Ma in the Himalaya: Evidence from lower crust-derived adakitic magmatism in Dala, eastern Tethyan Himalaya, Tibet. *Geological Journal*, in press. <https://doi.org/10.1002/gj.3639>
- Daniel, C. G., Hollister, L. S., Parrish, R. R., & Grujic, D. (2003). Exhumation of the Main central thrust from lower crustal depths, eastern Bhutan Himalaya. *Journal of Metamorphic Geology*, 21(4), 317–334 <https://doi.org/10.1046/j.1525-1314.2003.00445.x>
- Deniel, C., Vidal, P., Fernandez, A., Le Fort, P., & Peucat, J.-J. (1987). Isotopic study of the Manaslu granite (Himalaya, Nepal): Inferences on the age and source of Himalayan leucogranites. *Contributions to Mineralogy and Petrology*, 96(1), 78–92 <https://doi.org/10.1007/BF00375529>
- Dézes, P. J., Vannay, J.-C., Steck, A., Bussy, F., & Cosca, M. (1999). Synorogenic extension: Quantitative constraints on the age and displacement of the Zaskar shear zone (northwest Himalaya). *GSA Bulletin*, 111(3), 364–374 [https://doi.org/10.1130/0016-7606\(1999\)111<0364:SEQCOT>2.3.CO;2](https://doi.org/10.1130/0016-7606(1999)111<0364:SEQCOT>2.3.CO;2)
- Ding, H. X., Li, W. T., & Jiang, Y. Y. (2019). The metamorphism and the tectonic implication of the Cuonadong dome, eastern Himalaya. *Acta Petrologica Sinica*, 35(2), 312–324 (in Chinese with English abstract).
- Ding, H. X., Zhang, Z. M., Dong, X., Tian, Z. L., Xiang, H., Mu, H. C., ... Mao, L. J. (2016). Early Eocene (c. 50 Ma) collision of the Indian and Asian continents: Constraints from the north Himalayan metamorphic rocks, southeastern Tibet. *Earth and Planetary Science Letters*, 435, 64–73 <https://doi.org/10.1016/j.epsl.2015.12.006>
- Ding, H. X., Zhang, Z. M., Hu, K. M., Dong, X., Xiang, H., & Mu, H. C. (2016). P–T–t–D paths of the north Himalayan metamorphic rocks: Implications for the Himalayan orogeny. *Tectonophysics*, 683, 393–404 <https://doi.org/10.1016/j.tecto.2016.06.035>
- Ding, L., Paul, K., & Qiao, W. X. (2005). Paleocene–Eocene record of ophiolite obduction and initial India–Asia collision, south Central Tibet. *Tectonics*, 24(3), TC3001. <https://doi.org/10.1029/2004tc001729>
- Dong, H., Meng, Y., Xu, Z., Cao, H., Yi, Z., & Ma, Z. (2019). Timing of displacement along the Yardoi detachment fault, southern Tibet: Insights from zircon U–Pb and mica ⁴⁰Ar–³⁹Ar geochronology. *Journal of Earth Science*, 30(3), 535–548 <https://doi.org/10.1007/s12583-019-1223-z>
- Dong, H. W., Xu, Z. Q., Meng, Y. K., & Yi, Z. Y. (2017). Geochronology of leucogranites in the Cuonadong dome, southern Tibet and limitation of the timing of the southern Tibet detachment system (STDS). *Acta Petrologica Sinica*, 33(12), 3741–3752 (in Chinese with English abstract).
- Dunkl, I., Antolín, B., Wemmer, K., Rantitsch, G., Kienast, M., Montomoli, C., ... El Bay, R. (2011). Metamorphic evolution of the Tethyan Himalayan flysch in SE Tibet. *Geological Society, London, Special Publications*, 353(1), 45–69 <https://doi.org/10.1144/SP353.4>
- Edwards, M. A., & Harrison, T. M. (1997). When did the roof collapse? Late Miocene north–south extension in the high Himalaya revealed by Th–Pb monazite dating of the Khula Kangri granite. *Geology*, 25(6), 543–546 [https://doi.org/10.1130/0091-7613\(1997\)025<0543:WDTRCL>2.3.CO;2](https://doi.org/10.1130/0091-7613(1997)025<0543:WDTRCL>2.3.CO;2)
- Finch, M., Hasalova, P., Weinberg, R. F., & Fanning, C. M. (2014). Switch from thrusting to normal shearing in the Zaskar shear zone, NW Himalaya: Implications for channel flow. *Geological Society of America Bulletin*, 126(7–8), 892–924 <https://doi.org/10.1130/b30817.1>
- Foster, G., Kinny, P., Vance, D., Prince, C., & Harris, N. (2000). The significance of monazite U–Th–Pb age data in metamorphic assemblages; a combined study of monazite and garnet chronometry. *Earth and Planetary Science Letters*, 181(3), 327–340 [https://doi.org/10.1016/S0012-821X\(00\)00212-0](https://doi.org/10.1016/S0012-821X(00)00212-0)
- Fu, J. G., Li, G. M., Wang, G. H., Zhang, L. K., Liang, W., Zhang, Z., ... Huang, Y. (2018). Synchronous granite intrusion and E–W extension in the Cuonadong dome, southern Tibet, China: Evidence from field observations and thermochronologic results. *International Journal of Earth Sciences*, 107(6), 2023–2041 <https://doi.org/10.1007/s00531-018-1585-y>
- Gao, L. E., Gao, J. H., Zhao, L. H., Hou, K. J., & Tang, S. H. (2017). The Miocene leucogranite in the Nariyongcuo gneiss dome, southern Tibet: Products from melting metapelite and fractional crystallization. *Acta Petrologica Sinica*, 33(8), 2395–2411 (in Chinese with English abstract).
- Gao, L.-E., Zeng, L., Hu, G., Wang, Y., Wang, Q., Guo, C., & Hou, K. (2019). Early Paleozoic magmatism along the northern margin of East Gondwana. *Lithos*, 334–335, 25–41 <https://doi.org/10.1016/j.lithos.2019.03.007>
- Gao, L. E., & Zeng, L. S. (2014). Fluxed melting of metapelite and the formation of Miocene high-CaO two-mica granites in the Malashan gneiss dome, southern Tibet. *Geochimica et Cosmochimica Acta*, 130, 136–155 <https://doi.org/10.1016/j.gca.2014.01.003>

- Gao, L. E., Zeng, L. S., Gao, J. H., Shang, Z., Hou, K. J., & Wang, Q. (2016). Oligocene crustal anatexis in the Tethyan Himalaya, southern Tibet. *Lithos*, 264, 201–209 <https://doi.org/10.1016/j.lithos.2016.08.038>
- Gao, L. E., Zeng, L. S., Hou, K. J., Guo, C. L., Tang, S. H., Xie, K. J., ... Wang, L. (2013). Episodic crustal anatexis and the formation of Paiku composite leucogranitic pluton in the Malashan gneiss dome, southern Tibet. *Chinese Science Bulletin*, 58(28–29), 3546–3563 <https://doi.org/10.1007/s11434-013-5792-4>
- Gao, L. E., Zeng, L. S., & Xie, K. J. (2012). Eocene high grade metamorphism and crustal anatexis in the north Himalaya gneiss domes, southern Tibet. *Chinese Science Bulletin*, 57(6), 639–650 <https://doi.org/10.1007/s11434-011-4805-4>
- Gébelin, A., Jessup, M. J., Teyssier, C., Cosca, M. A., Law, R. D., Brunel, M., & Mulch, A. (2017). Infiltration of meteoric water in the south Tibetan detachment (Mount Everest, Himalaya): When and why? *Tectonics*, 36(4), 690–713 <https://doi.org/10.1002/2016TC004399>
- Gibson, R., Godin, L., Kellett, D. A., Cottle, J. M., & Archibald, D. (2016). Diachronous deformation along the base of the Himalayan metamorphic core, west-central Nepal. *GSA Bulletin*, 128(5–6), 860–878 <https://doi.org/10.1130/B31328.1>
- Godin, L., Brown, R. L., Hanmer, S., & Parrish, R. (1999). Back folds in the core of the Himalayan orogen: An alternative interpretation. *Geology*, 27(2), 151–154 [https://doi.org/10.1130/0091-7613\(1999\)027<0151:BFITCO>2.3.CO;2](https://doi.org/10.1130/0091-7613(1999)027<0151:BFITCO>2.3.CO;2)
- Godin, L., Gleeson, T. P., Searle, M. P., Ullrich, T. D., & Parrish, R. R. (2006). Locking of southward extrusion in favour of rapid crustal-scale buckling of the greater Himalayan sequence, Nar valley, central Nepal. *Geological Society, London, Special Publications*, 268, 269–292 <https://doi.org/10.1144/gsl.sp.2006.268.01.13>
- Godin, L., Grujic, D., Law, R. D., & Searle, M. P. (2006). Channel flow, ductile extrusion and exhumation in continental collision zones: An introduction. *Geological Society, London, Special Publications*, 268, 1–23 <https://doi.org/10.1144/GSL.SP.2006.268.01.01>
- Godin, L., Parrish, R. R., Brown, R. L., & Hodges, K. V. (2001). Crustal thickening leading to exhumation of the Himalayan metamorphic core of Central Nepal: Insight from U–Pb geochronology and $^{40}\text{Ar}/^{39}\text{Ar}$ Thermochronology. *Tectonics*, 20(5), 729–747 <https://doi.org/10.1029/2000TC001204>
- Gong, J., Ji, J., Han, B., Chen, J., Sun, D., Li, B., ... Zhong, D. (2012). Early subduction–exhumation and late channel flow of the Greater Himalayan Sequence: Implications from the Yadong section in the eastern Himalaya. *International Geology Review*, 54(10), 1184–1202 <https://doi.org/10.1080/00206814.2011.626604>
- Goscombe, B., Gray, D., & Foster, D. A. (2018). Metamorphic response to collision in the central Himalayan Orogen. *Gondwana Research*, 57, 191–265 <https://doi.org/10.1016/j.gr.2018.02.002>
- Greenwood, L. V., Argles, T. W., Parrish, R. R., Harris, N. B. W., & Warren, C. (2016). The geology and tectonics of Central Bhutan. *Journal of the Geological Society*, 173, 352–369 <https://doi.org/10.1144/jgs2015-031>
- Grujic, D., Casey, M., Davidson, C., Hollister, L. S., Kündig, R., Pavlis, T., & Schmid, S. (1996). Ductile extrusion of the higher Himalayan crystalline in Bhutan: Evidence from quartz microfabrics. *Tectonophysics*, 260(1), 21–43 [https://doi.org/10.1016/0040-1951\(96\)00074-1](https://doi.org/10.1016/0040-1951(96)00074-1)
- Grujic, D., Warren, C. J., & Wooden, J. L. (2011). Rapid synconvergent exhumation of Miocene-aged lower orogenic crust in the eastern Himalaya. *Lithosphere*, 3(5), 346–366 <https://doi.org/10.1130/L154.1>
- Guillot, S., Cosca, M., Allemand, P., & Le Fort, P. (1999). Contrasting metamorphic and geochronologic evolution along the Himalayan belt. *Geological Society of America Special Papers*, 328, 117–128 <https://doi.org/10.1130/0-8137-2328-0.117>
- Guillot, S., Hodges, K., Fort, P. L., & Pêcher, A. (1994). New constraints on the age of the Manaslu leucogranite: Evidence for episodic tectonic denudation in the Central Himalayas. *Geology*, 22(1994), 559–562 [https://doi.org/10.1130/0091-7613\(1994\)022<0559:NCOTAO>2.3.CO;2](https://doi.org/10.1130/0091-7613(1994)022<0559:NCOTAO>2.3.CO;2)
- Guo, L., Zhang, J., & Zhang, B. (2008). Structures, kinematics, thermochronology and tectonic evolution of the Ramba gneiss dome in the northern Himalaya. *Progress in Natural Science*, 18(7), 851–860 <https://doi.org/10.1016/j.pnsc.2008.01.016>
- Guo, Z. F., & Wilson, M. (2012). The Himalayan leucogranites: Constraints on the nature of their crustal source region and geodynamic setting. *Gondwana Research*, 22(2), 360–376 <https://doi.org/10.1016/j.jgr.2011.07.027>
- Harris, N., & Massey, J. (1994). Decompression and anatexis of Himalayan metapelites. *Tectonics*, 13(6), 1537–1546 <https://doi.org/10.1029/94TC01611>
- Harrison, T. M., Grove, M., Mckeegan, K. D., Coath, C. D., Lovera, O. M., & Fort, P. L. (1999). Origin and episodic emplacement of the Manaslu intrusive complex, central Himalaya. *Journal of Petrology*, 40(1), 3–19 <https://doi.org/10.1093/ptro/40.1.3>
- Harrison, T. M., Lovera, O. M., & Grove, M. (1997). New insights into the origin of two contrasting Himalayan granite belts. *Geology*, 25(10), 899–902 [https://doi.org/10.1130/0091-7613\(1997\)025<0899:NIITOO>2.3.CO;2](https://doi.org/10.1130/0091-7613(1997)025<0899:NIITOO>2.3.CO;2)
- Harrison, T. M., Mckeegan, K. D., & LeFort, P. (1995). Detection of inherited monazite in the Manaslu leucogranite by $^{208}\text{Pb}/^{232}\text{Th}$ ion microprobe dating: Crystallization age and tectonic implications. *Earth and Planetary Science Letters*, 133(3), 271–282 [https://doi.org/10.1016/0012-821X\(95\)00091-P](https://doi.org/10.1016/0012-821X(95)00091-P)
- He, D., Webb, A. A. G., Larson, K. P., Martin, A. J., & Schmitt, A. K. (2015). Extrusion vs. duplexing models of Himalayan mountain building 3: Duplexing dominates from the Oligocene to present. *International Geology Review*, 57(1), 1–27 <https://doi.org/10.1080/00206814.2014.986669>
- He, D., Webb, A. A. G., Larson, K. P., & Schmitt, A. K. (2016). Extrusion vs. duplexing models of Himalayan mountain building 2: The South Tibet detachment at the Dadelhdura klippe. *Tectonophysics*, 667, 87–107 <https://doi.org/10.1016/j.tecto.2015.11.014>
- Hintersberger, E., Thiede, R. C., Strecker, M. R., & Hacker, B. R. (2010). East–west extension in the NW Indian Himalaya. *Geological Society of America Bulletin*, 122(9–10), 1499–1515 <https://doi.org/10.1130/B26589.1>
- Hodges, K., Bowring, S., Davidek, K., Hawkins, D., & Krol, M. (1998). Evidence for rapid displacement on Himalayan normal faults and the importance of tectonic denudation in the evolution of mountain ranges. *Geology*, 26(6), 483–486 [https://doi.org/10.1130/0091-7613\(1998\)026<0483:efrdoh>2.3.co;2](https://doi.org/10.1130/0091-7613(1998)026<0483:efrdoh>2.3.co;2)
- Hodges, K., Hames, W., Olszewski, W., Burchfiel, B., Royden, L., & Chen, Z. (1994). Thermobarometric and $^{40}\text{Ar}/^{39}\text{Ar}$ geochronologic constraints on Eohimalayan metamorphism in the Dinggye area, southern Tibet. *Contributions to Mineralogy and Petrology*, 117(2), 151–163 <https://doi.org/10.1007/BF00286839>
- Hodges, K. V. (2000). Tectonics of the Himalaya and southern Tibet from two perspectives. *Geological Society of America Bulletin*, 112(3), 324–350 [https://doi.org/10.1130/0016-7606\(2000\)112<324:TOTHAS>2.0.CO;2](https://doi.org/10.1130/0016-7606(2000)112<324:TOTHAS>2.0.CO;2)
- Hodges, K. V., Parrish, R. R., Housh, T. B., Lux, D. R., Burchfiel, B. C., Royden, L. H., & Chen, Z. (1992). Simultaneous Miocene extension and shortening in the Himalayan orogen. *Science*, 258(5087), 1466–1470 <https://doi.org/10.1126/science.258.5087.1466>
- Hodges, K. V., Parrish, R. R., & Searle, M. P. (1996). Tectonic evolution of the Central Annapurna range, Nepalese Himalayas. *Tectonics*, 15(6), 1264–1291 <https://doi.org/10.1029/96TC01791>
- Horton, F., Lee, J., Hacker, B., Bowman-Kamaha'o, M., & Cosca, M. (2015). Himalayan gneiss dome formation in the middle crust and exhumation by normal faulting: New geochronology of Gianbul dome, northwestern India. *Geological Society of America Bulletin*, 127(1–2), 162–180. <https://doi.org/10.1130/B31005.1>

- Horton, F., & Leech, M. L. (2013). Age and origin of granites in the Karakoram shear zone and Greater Himalaya Sequence, NW India. *Lithosphere*, 5(3), 300–320 <https://doi.org/10.1130/I213.1>
- Hu, Z., Zhang, W., Liu, Y., Gao, S., Li, M., Zong, K., ... Hu, S. (2015). “Wave” signal-smoothing and mercury-removing device for laser ablation Quadrupole and multiple collector ICPMS analysis: Application to Lead isotope analysis. *Analytical Chemistry*, 87(2), 1152–1157 <https://doi.org/10.1021/ac503749k>
- Huang, C., Zhao, Z., Li, G., Zhu, D.-C., Liu, D., & Shi, Q. (2017). Leucogranites in Lhozag, southern Tibet: Implications for the tectonic evolution of the eastern Himalaya. *Lithos*, 294–295, 246–262 <https://doi.org/10.1016/j.lithos.2017.09.014>
- Huang, C. M., Li, G. M., Zhang, Z., Liang, W., Huang, Y., Zhang, L. K., ... Fu, J. G. (2018). Petrogenesis of the Cuonadong leucogranite in South Tibet: Constraints from bulk-rock geochemistry and zircon U–Pb dating. *Earth Science Frontiers*, 25(6), 182–195 (in Chinese with English Abstract).
- Huang, Y., Zhang, L., Liang, W., Li, G., Dong, S., Wu, J., & Xia, X. (2019). Petrogenesis of the early Cretaceous Kada igneous rocks from Tethyan Himalaya: Implications for initial break-up of eastern Gondwana. *Geological Journal*, 54(3), 1294–1316 <https://doi.org/10.1002/gj.3227>
- Iaccarino, S., Montomoli, C., Carosi, R., Massonne, H.-J., Langone, A., & Visonà, D. (2015). Pressure–temperature–time–deformation path of kyanite-bearing migmatitic paragneiss in the Kali Gandaki valley (Central Nepal): Investigation of late Eocene–Early Oligocene melting processes. *Lithos*, 231, 103–121. <https://doi.org/10.1016/j.lithos.2015.06.005>
- Iaccarino, S., Montomoli, C., Carosi, R., Montemagni, C., Massonne, H. J., Langone, A., ... Visonà, D. (2017). Pressure-temperature-deformation-time constraints on the south Tibetan detachment system in the Garhwal Himalaya (NW India). *Tectonics*, 36(11), 2281–2304 <https://doi.org/10.1002/2017TC004566>
- Imayama, T., Takeshita, T., Yi, K., Cho, D.-L., Kitajima, K., Tsutsumi, Y., ... Sano, Y. (2012). Two-stage partial melting and contrasting cooling history within the higher Himalayan crystalline sequence in the far-eastern Nepal Himalaya. *Lithos*, 134–135, 1–22 <https://doi.org/10.1016/j.lithos.2011.12.004>
- Inger, S. (1998). Timing of an extensional detachment during convergent orogeny: New Rb–Sr geochronological data from the Zaskar shear zone, northwestern Himalaya. *Geology*, 26(3), 223–226 [https://doi.org/10.1130/0091-7613\(1998\)026<0223:TOAEDD>2.3.CO;2](https://doi.org/10.1130/0091-7613(1998)026<0223:TOAEDD>2.3.CO;2)
- Inger, S., & Harris, N. B. W. (1992). Tectonothermal evolution of the high Himalayan crystalline sequence, Langtang Valley, northern Nepal. *Journal of Metamorphic Geology*, 10(3), 439–452 <https://doi.org/10.1111/j.1525-1314.1992.tb00095.x>
- Jessup, M. J., Cottle, J. M., Searle, M. P., Law, R. D., Newell, D. L., Tracy, R. J., & Waters, D. J. (2008). P–T–t–D paths of Everest series schist, Nepal. *Journal of Metamorphic Geology*, 26(7), 717–739 <https://doi.org/10.1111/j.1525-1314.2008.00784.x>
- Jessup, M. J., Langille, J. M., Cottle, J. M., & Ahmad, T. (2016). Crustal thickening, Barrovian metamorphism, and exhumation of mid-crustal rocks during doming and extrusion: Insights from the Himalaya, NW India. *Tectonics*, 35(1), 160–186 <https://doi.org/10.1002/2015TC003962>
- Jessup, M. J., Langille, J. M., Diedesch, T. F., & Cottle, J. M. (2019). Gneiss dome formation in the Himalaya and southern Tibet. *Geological Society, London, Special Publications*, 483, 401–422 <https://doi.org/10.1144/sp483.15>
- Ji, W.-Q., Wu, F.-Y., Liu, X.-C., Liu, Z.-C., Zhang, C., Liu, T., ... Paterson, S. R. (2020). Pervasive Miocene melting of thickened crust from the Lhasa terrane to Himalaya, southern Tibet and its constraint on generation of Himalayan leucogranite. *Geochimica et Cosmochimica Acta*, in Press. <https://doi.org/10.1016/j.gca.2019.07.048>
- Kali, E., Leloup, P.H., Arnaud, N., Mahéo, G., Liu, D., Boutonnet, E., ... Li, H. (2010). Exhumation history of the deepest central Himalayan rocks, Ama Drime range: Key pressure-temperature-deformation-time constraints on orogenic models. *Tectonics*, 29(2), TC2014. <https://doi.org/10.1029/2009TC002551>
- Kawakami, T., Aoya, M., Wallis, S., Lee, J., Terada, K., Wang, Y., & Heizler, M. (2007). Contact metamorphism in the Malashan dome, north Himalayan gneiss domes, southern Tibet: An example of shallow extensional tectonics in the Tethys Himalaya. *Journal of Metamorphic Geology*, 25(8), 831–853 <https://doi.org/10.1111/j.1525-1314.2007.00731.x>
- Kellett, D. A., Cottle, J. M., & Larson, K. P. (2019). The south Tibetan detachment system: History, advances, definition and future directions. *Geological Society, London, Special Publications*, 483, 377–400 <https://doi.org/10.1144/sp483.2>
- Kellett, D. A., Cottle, J. M., & Smit, M. (2014). Eocene deep crust at Ama Drime, Tibet: Early evolution of the Himalayan orogen. *Lithosphere*, 6(4), 220–229 <https://doi.org/10.1130/L350.1>
- Kellett, D. A., & Grujic, D. (2012). New insight into the south Tibetan detachment system: Not a single progressive deformation. *Tectonics*, 31(2), TC2007 <https://doi.org/10.1029/2011tc002957>
- Kellett, D. A., Grujic, D., Coutand, I., Cottle, J., & Mukul, M. (2013). The south Tibetan detachment system facilitates ultra rapid cooling of granulite-facies rocks in Sikkim Himalaya. *Tectonics*, 32(2), 252–270 <https://doi.org/10.1002/tect.20014>
- Kellett, D. A., Grujic, D., & Erdmann, S. (2009). Miocene structural reorganization of the south Tibetan detachment, eastern Himalaya: Implications for continental collision. *Lithosphere*, 1(5), 259–281 <https://doi.org/10.1130/L56.1>
- Kellett, D. A., Grujic, D., Warren, C., Cottle, J., Jamieson, R., & Tenzin, T. (2010). Metamorphic history of a syn-convergent orogen-parallel detachment: The south Tibetan detachment system, Bhutan Himalaya. *Journal of Metamorphic Geology*, 28(8), 785–808 <https://doi.org/10.1111/j.1525-1314.2010.00893.x>
- King, J., Harris, N., Argles, T., Parrish, R., Charlier, B., Sherlock, S., & Zhang, H. F. (2007). First field evidence of southward ductile flow of Asian crust beneath southern Tibet. *Geology*, 35(8), 727–730 <https://doi.org/10.1130/G23630A.1>
- King, J., Harris, N., Argles, T., Parrish, R., & Zhang, H. F. (2011). Contribution of crustal anatexis to the tectonic evolution of Indian crust beneath southern Tibet. *Geological Society of America Bulletin*, 123(1), 218–239 <https://doi.org/10.1130/B30085.1>
- Langille, J. M., Jessup, M. J., Cottle, J. M., Lederer, G., & Ahmad, T. (2012). Timing of metamorphism, melting and exhumation of the Leo Pargil dome, Northwest India. *Journal of Metamorphic Geology*, 30(8), 769–791 <https://doi.org/10.1111/j.1525-1314.2012.00998.x>
- Larson, K. P., & Cottle, J. M. (2015). Initiation of crustal shortening in the Himalaya. *Terra Nova*, 27(3), 169–174 <https://doi.org/10.1111/ter.12145>
- Larson, K. P., Cottle, J. M., & Godin, L. (2011). Petrochronologic record of metamorphism and melting in the upper greater Himalayan sequence, Manaslu–Himal Chuli Himalaya, west-central Nepal. *Lithosphere*, 3(6), 379–392 <https://doi.org/10.1130/l149.1>
- Larson, K. P., Godin, L., Davis, W. J., & Davis, D. W. (2010). Out-of-sequence deformation and expansion of the Himalayan orogenic wedge: Insight from the Changgo culmination, south Central Tibet. *Tectonics*, 29(4), TC4013 <https://doi.org/10.1029/2008TC002393>
- Laskowski, A. K., Kapp, P., Vervoort, J. D., & Ding, L. (2016). High-pressure Tethyan Himalaya rocks along the India–Asia suture zone in southern Tibet. *Lithosphere*, 8(5), 574–682 <https://doi.org/10.1130/L544.1>
- Lederer, G. W., Cottle, J. M., Jessup, M. J., Langille, J. M., & Ahmad, T. (2013). Timescales of partial melting in the Himalayan middle crust: Insight from the Leo Pargil dome, Northwest India. *Contributions to Mineralogy and Petrology*, 166(5), 1415–1441 <https://doi.org/10.1007/s00410-013-0935-9>
- Lee, J., Hacker, B. R., Dinklage, W. S., Wang, Y., Gans, P., Calvert, A., ... McClelland, W. (2000). Evolution of the Kangmar dome, southern

- Tibet: Structural, petrologic, and thermochronologic constraints. *Tectonics*, 19(5), 872–895 <https://doi.org/10.1029/1999TC001147>
- Lee, J., Hager, C., Wallis, S. R., Stockli, D. F., Whitehouse, M. J., Aoya, M., & Wang, Y. (2011). Middle to late Miocene extremely rapid exhumation and thermal reequilibration in the Kung Co rift, southern Tibet. *Tectonics*, 30(2), TC2007 <https://doi.org/10.1029/2010tc002745>
- Lee, J., McClelland, W., Wang, Y., Blythe, A., & McWilliams, M. (2006). Oligocene–Miocene middle crustal flow in southern Tibet: Geochronology of Mabja dome. *Geological Society, London, Special Publications*, 268, 445–469 <https://doi.org/10.1144/GSL.SP.2006.268.01.21>
- Lee, J., & Whitehouse, M. J. (2007). Onset of mid-crustal extensional flow in southern Tibet: Evidence from U/Pb zircon ages. *Geology*, 35(1), 45–48 <https://doi.org/10.1130/g228424a.1>
- Leech, M. L. (2008). Does the Karakoram fault interrupt mid-crustal channel flow in the western Himalaya? *Earth and Planetary Science Letters*, 276(3), 314–322 <https://doi.org/10.1016/j.epsl.2008.10.006>
- Leloup, P. H., Liu, X., Mahéo, G., Paquette, J.-L., Arnaud, N., Aubray, A., & Liu, X. (2015). New constraints on the timing of partial melting and deformation along the Nyalam section (central Himalaya): Implications for extrusion models. *Geological Society, London, Special Publications*, 412, 131–175 <https://doi.org/10.1144/sp412.11>
- Leloup, P. H., Mahéo, G., Arnaud, N., Kali, E., Boutonnet, E., Liu, D., ... Haibing, L. (2010). The South Tibet detachment shear zone in the Dinggye area: Time constraints on extrusion models of the Himalayas. *Earth and Planetary Science Letters*, 292(1), 1–16 <https://doi.org/10.1016/j.epsl.2009.12.035>
- Li, G., Tian, Y., Kohn, B. P., Sandiford, M., Xu, Z., & Cai, Z. (2015). Cenozoic low temperature cooling history of the northern Tethyan Himalaya in Zedang, SE Tibet and its implications. *Tectonophysics*, 643, 80–93. <https://doi.org/10.1016/j.tecto.2014.12.014>
- Lin, B., Tang, J. X., Zheng, W. B., Leng, Q. F., Lin, X., Wang, Y. Y., ... Yuan, M. (2016). Geochemical characteristics, age and genesis of Cuonadong leucogranite, Tibet. *Acta Petrologica et Mineralogica*, 35(3), 391–406 (in Chinese with English abstract).
- Lin, C., Zhang, J., Wang, X., Putthapiban, P., Zhang, B., & Huang, T. (2020). Oligocene initiation of the south Tibetan detachment system: Constraints from syn-tectonic leucogranites in the Kampa dome, northern Himalaya. *Lithos*, 354–355, 105332 <https://doi.org/10.1016/j.lithos.2019.105332>
- Liu, X. B., Liu, X. H., Leloup, P. H., Maheo, G., Paquette, J. L., Zhang, X. G., & Zhou, X. J. (2012). Ductile deformation within upper Himalaya crystalline sequence and geological implications, in Nyalam area, southern Tibet. *Chinese Science Bulletin*, 57(26), 3469–3481 <https://doi.org/10.1007/s11434-012-5228-6>
- Liu, X. C., Wu, F. Y., Yu, L. J., Liu, Z. C., Ji, W. Q., & Wang, J. G. (2016). Emplacement age of leucogranite in the Kampa dome, southern Tibet. *Tectonophysics*, 667, 163–175 <https://doi.org/10.1016/j.tecto.2015.12.001>
- Liu, Y., Hu, Z., Zong, K., Gao, C., Gao, S., Xu, J., & Chen, H. (2010). Reappraisal and refinement of zircon U–Pb isotope and trace element analyses by LA–ICP–MS. *Chinese Science Bulletin*, 55(15), 1535–1546 <https://doi.org/10.1007/s11434-010-3052-4>
- Liu, Y., Siebel, W., Massonne, H. J., & Xiao, X. C. (2007). Geochronological and petrological constraints for tectonic evolution of the central Greater Himalayan Sequence in the Kharta area, southern Tibet. *The Journal of Geology*, 115(2), 215–230 <https://doi.org/10.1086/510806>
- Liu, Z. C., Wu, F. Y., Ding, L., Liu, X. C., Wang, J. G., & Ji, W. Q. (2016). Highly fractionated late Eocene (~35 Ma) leucogranite in the Xiaru dome, Tethyan Himalaya, South Tibet. *Lithos*, 240–243, 337–354 <https://doi.org/10.1016/j.lithos.2015.11.026>
- Liu, Z. C., Wu, F. Y., Ji, W. Q., Wang, J. G., & Liu, C. Z. (2014). Petrogenesis of the Ramba leucogranite in the Tethyan Himalaya and constraints on the channel flow model. *Lithos*, 208–209, 118–136 <https://doi.org/10.1016/j.lithos.2014.08.022>
- Liu, Z. C., Wu, F. Y., Qiu, Z. L., Wang, J. G., Liu, X. C., Ji, W. Q., & Liu, C. Z. (2017). Leucogranite geochronological constraints on the termination of the south Tibetan detachment in eastern Himalaya. *Tectonophysics*, 721, 106–122 <https://doi.org/10.1016/j.tecto.2017.08.019>
- Ludwig, K. R. (2012). *User's manual for Isoplot 3.75: A Geochronological toolkit for Microsoft excel* (pp. 1–76). Berkeley: Berkeley Geochronology Center.
- Maluski, H., Matte, P., Brunal, M., & Xiao, X. (1988). Argon 39–argon 40 dating of metamorphic and plutonic events in the north and high Himalaya belts (southern Tibet–China). *Tectonics*, 7(2), 299–326 <https://doi.org/10.1029/TC007i002p00299>
- Martin, A. J., Gehrels, G. E., & DeCelles, P. G. (2007). The tectonic significance of (U,Th)/Pb ages of monazite inclusions in garnet from the Himalaya of central Nepal. *Chemical Geology*, 244(1), 1–24 <https://doi.org/10.1016/j.chemgeo.2007.05.003>
- McCallister, A. T., Taylor, M. H., Murphy, M., Styron, R. H., & Stockli, D. F. (2014). Thermochronologic constraints on the late Cenozoic exhumation history of the Gurla Mandhata metamorphic core complex, Southwestern Tibet. *Tectonics*, 33(2), 27–52 <https://doi.org/10.1002/2013TC003302>
- Mitsuishi, M., Wallis, S. R., Aoya, M., Lee, J., & Wang, Y. (2012). E–W extension at 19 Ma in the Kung Co area, S. Tibet: Evidence for contemporaneous E–W and N–S extension in the Himalayan orogen. *Earth and Planetary Science Letters*, 325–326, 10–20. <https://doi.org/10.1016/j.epsl.2011.11.013>
- Montemagni, C., Iaccarino, S., Montomoli, C., Carosi, R. K., Jain Jain, A., & Villa, I. (2018). Age constraints on the deformation style of the south Tibetan detachment system in Garhwal Himalaya. *Italian Journal of Geosciences*, 137(2), 175–187 <https://doi.org/10.3301/IJG.2018.07>
- Montomoli, C., Carosi, R., Rubatto, D., Visonà, D., & Iaccarino, S. (2017). Tectonic activity along the inner margin of the south Tibetan detachment constrained by syntectonic leucogranite emplacement in Western Bhutan. *Italian Journal of Geosciences*, 136(1), 5–14 <https://doi.org/10.3301/ijg.2015.26>
- Montomoli, C., Iaccarino, S., Antolin, B., Appel, E., Carosi, R., Dunkl, I., ... Visonà, D. (2017). Tectono-metamorphic evolution of the Tethyan sedimentary sequence (Himalayas, SE Tibet). *Italian Journal of Geosciences*, 136(1), 73–88 <https://doi.org/10.3301/ijg.2015.42>
- Montomoli, C., Iaccarino, S., Carosi, R., Langone, A., & Visonà, D. (2013). Tectonometamorphic discontinuities within the Greater Himalayan Sequence in Western Nepal (central Himalaya): Insights on the exhumation of crystalline rocks. *Tectonophysics*, 608, 1349–1370. <https://doi.org/10.1016/j.tecto.2013.06.006>
- Mottram, C. M., Cottle, J., & Kylander-Clark, A. (2019). Campaign-style U–Pb titanite petrochronology; along-strike variations in timing of metamorphism in the Himalayan metamorphic Core. *Geoscience Frontiers*, 10(3), 827–847 <https://doi.org/10.1016/j.gsf.2018.09.007>
- Murphy, M. A., & Copeland, P. (2005). Transtensional deformation in the central Himalaya and its role in accommodating growth of the Himalayan orogen. *Tectonics*, 24(4), TC4012 <https://doi.org/10.1029/2004TC001659>
- Murphy, M. A., & Harrison, T. M. (1999). Relationship between leucogranites and the Qomolangma detachment in the Rongbuk Valley, South Tibet. *Geology*, 27(9), 831–834 [https://doi.org/10.1130/0091-7613\(1999\)027<0831:RBLATQ>2.3.CO;2](https://doi.org/10.1130/0091-7613(1999)027<0831:RBLATQ>2.3.CO;2)
- Murphy, M. A., Yin, A., Kapp, P., Harrison, T. M., Manning, C. E., Ryerson, F. J., ... Guo, J. (2002). Structural evolution of the Gurla Mandhata detachment system, Southwest Tibet: Implications for the eastward extent of the Karakoram fault system. *Geological Society of America Bulletin*, 114(4), 428–447 [https://doi.org/10.1130/0016-7606\(2002\)114<0428:SEOTGM>2.0.CO;2](https://doi.org/10.1130/0016-7606(2002)114<0428:SEOTGM>2.0.CO;2)

- Nagy, C., Godin, L., Antolín, B., Cottle, J., & Archibald, D. (2015). Mid-Miocene initiation of orogen-parallel extension, NW Nepal Himalaya. *Lithosphere*, 7(5), 483–502 <https://doi.org/10.1130/L425.1>
- Nelson, K. D., Zhao, W., Brown, L., Kuo, J., Che, J., Liu, X., ... Mechie, J. (1996). Partially molten middle crust beneath southern Tibet: Synthesis of project INDEPTH results. *Science*, 274(5293), 1684–1688 <https://doi.org/10.1126/science.274.5293.1684>
- Noble, S. R., & Searle, M. P. (1995). Age of crustal melting and leucogranite formation from U–Pb zircon and monazite dating in the western Himalaya, Zaskar, India. *Geology*, 23(12), 1135–1138 [https://doi.org/10.1130/0091-7613\(1995\)023<1135:AOCMAL>2.3.CO;2](https://doi.org/10.1130/0091-7613(1995)023<1135:AOCMAL>2.3.CO;2)
- Pullen, A., Kapp, P., DeCelles, P. G., Gehrels, G. E., & Ding, L. (2011). Cenozoic anatexis and exhumation of Tethyan sequence rocks in the Xiao Gurla range, Southwest Tibet. *Tectonophysics*, 501(1–4), 28–40. <https://doi.org/10.1016/j.tecto.2011.01.008>
- Quigley, M., Liangjun, Y., Xiaohan, L., Wilson, C. J. L., Sandiford, M., & Phillips, D. (2006). $^{40}\text{Ar}/^{39}\text{Ar}$ thermochronology of the Kampa dome, southern Tibet: Implications for tectonic evolution of the north Himalayan gneiss domes. *Tectonophysics*, 421(3–4), 269–297. <https://doi.org/10.1016/j.tecto.2006.05.002>
- Ratschbacher, L., Krumrei, I., Blumenwitz, M., Staiger, M., Gloaguen, R., Miller, B. V., ... Appel, E. (2011). Rifting and strike-slip shear in Central Tibet and the geometry, age and kinematics of upper crustal extension in Tibet. *Geological Society, London, Special Publications*, 353, 127–163 <https://doi.org/10.1144/SP353.8>
- Robinson, D. M. (2008). Forward modeling the kinematic sequence of the central Himalayan thrust belt, western Nepal. *Geosphere*, 4(5), 785–801 <https://doi.org/10.1130/ges00163.1>
- Robinson, D. M., DeCelles, P. G., & Copeland, P. (2006). Tectonic evolution of the Himalayan thrust belt in western Nepal: Implications for channel flow models. *GSA Bulletin*, 118(7–8), 865–885 <https://doi.org/10.1130/B25911.1>
- Robyr, M., Epard, J.-L., & El Korh, A. (2014). Structural, metamorphic and geochronological relations between the Zaskar shear zone and the Miyar shear zone (NW Indian Himalaya): Evidence for two distinct tectonic structures and implications for the evolution of the high Himalayan crystalline of Zaskar. *Journal of Asian Earth Sciences*, 79, 1–15 <https://doi.org/10.1016/j.jseae.2013.09.007>
- Robyr, M., Hacker, B. R., & Mattinson, J. M. (2006). Doming in compressional orogenic settings: New geochronological constraints from the NW Himalaya. *Tectonics*, 25(2), TC2007 <https://doi.org/10.1029/2004TC001774>
- Rubatto, D., Chakraborty, S., & Dasgupta, S. (2013). Timescales of crustal melting in the higher Himalayan Crystallines (Sikkim, eastern Himalaya) inferred from trace element-constrained monazite and zircon chronology. *Contributions to Mineralogy and Petrology*, 165(2), 349–372 <https://doi.org/10.1007/s00410-012-0812-y>
- Sachan, H. K., Kohn, M. J., Saxena, A., & Corrie, S. L. (2010). The Malari leucogranite, Garhwal Himalaya, northern India: Chemistry, age, and tectonic implications. *Geological Society of America Bulletin*, 122(11–12), 1865–1876 <https://doi.org/10.1130/B30153.1>
- Sakai, H., Sawada, M., Takigami, Y., Orihashi, Y., Danhara, T., Iwano, H., ... Li, J. (2005). Geology of the summit limestone of Mount Qomolangma (Everest) and cooling history of the yellow band under the Qomolangma detachment. *Island Arc*, 14(4), 297–310 <https://doi.org/10.1111/j.1440-1738.2005.00499.x>
- Schärer, U., Xu, R.-H., & Allègre, C. J. (1986). U–(Th)–Pb systematics and ages of Himalayan leucogranites, South Tibet. *Earth and Planetary Science Letters*, 77(1), 35–48 [https://doi.org/10.1016/0012-821X\(86\)90130-5](https://doi.org/10.1016/0012-821X(86)90130-5)
- Schlup, M., Steck, A., Carter, A., Cosca, M., Epard, J.-L., & Hunziker, J. (2011). Exhumation history of the NW Indian Himalaya revealed by fission track and $^{40}\text{Ar}/^{39}\text{Ar}$ ages. *Journal of Asian Earth Sciences*, 40(1), 334–350. <https://doi.org/10.1016/j.jseae.2010.06.008>
- Schultz, M. H., Hodges, K. V., Ehlers, T. A., van Soest, M., & Wartho, J.-A. (2017). Thermochronologic constraints on the slip history of the south Tibetan detachment system in the Everest region, southern Tibet. *Earth and Planetary Science Letters*, 459, 105–117 <https://doi.org/10.1016/j.epsl.2016.11.022>
- Searle, M. (2013). Crustal melting, ductile flow, and deformation in mountain belts: Cause and effect relationships. *Lithosphere*, 5(5), 547–554 <https://doi.org/10.1130/RF.L006.1>
- Searle, M. P. (2010). Low-angle normal faults in the compressional Himalayan orogen; evidence from the Annapurna–Dhaulagiri Himalaya, Nepal. *Geosphere*, 6(4), 296–315 <https://doi.org/10.1130/ges00549.1>
- Searle, M. P., Noble, S. R., Hurford, A. J., & Rex, D. C. (1999). Age of crustal melting, emplacement and exhumation history of the Shivling leucogranite, Garhwal Himalaya. *Geological Magazine*, 136(5), 513–525 <https://doi.org/10.1017/S0016756899002885>
- Searle, M. P., Simpson, R. L., Law, R. D., Parrish, R. R., & Waters, D. J. (2003). The structural geometry, metamorphic and magmatic evolution of the Everest massif, high Himalaya of Nepal–South Tibet. *Journal of the Geological Society*, 160(3), 345–366 <https://doi.org/10.1144/0016-764902-126>
- Searle, M. P., Waters, D. J., Rex, D. C., & Wilson, R. N. (1992). Pressure, temperature and time constraints on Himalayan metamorphism from eastern Kashmir and western Zaskar. *Journal of the Geological Society*, 149(5), 753–773 <https://doi.org/10.1144/gsjgs.149.5.0753>
- Searle, M. P., & Whitehouse, M. J. (1997). Shisha Pangma leucogranite, south Tibetan Himalaya; field relations, geochemistry, age, origin, and emplacement. *Journal of Geology*, 105(3), 295–317 <https://doi.org/10.1086/515924>
- Sen, K., Chaudhury, R., & Pfänder, J. (2015). ^{40}Ar – ^{39}Ar age constraint on deformation and brittle–ductile transition of the Main central thrust and the south Tibetan detachment zone from Dhauliganga valley, Garhwal Himalaya, India. *Journal of Geodynamics*, 88, 1–13 <https://doi.org/10.1016/j.jog.2015.04.004>
- Shen, T., Wang, G., Leloup, P. H., van der Beek, P., Bernet, M., Cao, K., ... Zhang, K. (2016). Controls on Cenozoic exhumation of the Tethyan Himalaya from fission-track thermochronology and detrital zircon U–Pb geochronology in the Gyirong basin area, southern Tibet. *Tectonics*, 35(7), 1713–1734 <https://doi.org/10.1002/2016TC004149>
- Shi, Q. S., Huang, C. M., Lei, H. S., Qi, N. Y., Tong, X., & Zhao, Z. D. (2017). Geochronology, geochemistry, and petrogenesis of Yamarong leucogranite in Tsona area, eastern Himalaya, Tibet. *Acta Petrologica Sinica*, 33(8), 2454–2466 (in Chinese with English abstract).
- Shrestha, S., Larson, K. P., Duesterhoeft, E., Soret, M., & Cottle, J. M. (2019). Thermodynamic modelling of phosphate minerals and its implications for the development of P–T–t histories: A case study in garnet–monazite bearing metapelites. *Lithos*, 334–335, 141–160 <https://doi.org/10.1016/j.lithos.2019.03.021>
- Simpson, R. L., Parrish, R. R., Searle, M. P., & Waters, D. J. (2000). Two episodes of monazite crystallization during metamorphism and crustal melting in the Everest region of the Nepalese Himalaya. *Geology*, 28(5), 403–406 [https://doi.org/10.1130/0091-7613\(2000\)28<403:teomcd>2.0.co;2](https://doi.org/10.1130/0091-7613(2000)28<403:teomcd>2.0.co;2)
- Singh, S. (2019). Protracted zircon growth in migmatites and in situ melt of higher Himalayan Crystallines: U–Pb ages from Bhagirathi valley, NW Himalaya, India. *Geoscience Frontiers*, 10, 793–809 <https://doi.org/10.1016/j.gsf.2017.12.014>
- Smit, M. A., Hacker, B. R., & Lee, J. (2014). Tibetan garnet records early Eocene initiation of thickening in the Himalaya. *Geology*, 42(7), 591–594 <https://doi.org/10.1130/g35524.1>
- Sorkhabi, R. B., Stump, E., Foland, K. A., & Jain, A. K. (1996). Fission-track and $^{40}\text{Ar}/^{39}\text{Ar}$ evidence for episodic denudation of the Gangotri granites in the Garhwal higher Himalaya, India. *Tectonophysics*, 260(1), 187–199 [https://doi.org/10.1016/0040-1951\(96\)00083-2](https://doi.org/10.1016/0040-1951(96)00083-2)
- Soucy La Roche, R., Godin, L., Cottle, J. M., & Kellett, D. A. (2016). Direct shear fabric dating constrains early Oligocene onset of the south Tibetan detachment in the western Nepal Himalaya. *Geology*, 44(6), 403–406 <https://doi.org/10.1130/G37754.1>

- Soucy La Roche, R., Godin, L., Cottle, J. M., & Kellett, D. A. (2018). Preservation of the early evolution of the Himalayan middle crust in foreland klippen: Insights from the Karnali klippe, West Nepal. *Tectonics*, 37(5), 1161–1193 <https://doi.org/10.1002/2017tc004847>
- Soucy La Roche, R., Godin, L., Cottle, J. M., & Kellett, D. A. (2019). Tectonometamorphic evolution of the tip of the Himalayan metamorphic core in the Jajarkot klippe, West Nepal. *Journal of Metamorphic Geology*, 37(2), 239–269 <https://doi.org/10.1111/jmg.12459>
- Spencer, C. J., Dyck, B., Mottram, C. M., Roberts, N. M. W., Yao, W., & Marin, E. L. (2019). Deconvolving the pre-Himalayan Indian margintales of crustal growth and destruction. *Geoscience Frontiers*, 10, 863–872 <https://doi.org/10.1016/j.gsf.2018.02.007>
- Spencer, C. J., Kirkland, C. L., Prave, A. R., Strachan, R. A., & Pease, V. (2019). Crustal reworking and orogenic styles inferred from zircon Hf isotopes: Proterozoic examples from the North Atlantic region. *Geoscience Frontiers*, 10(2), 417–424 <https://doi.org/10.1016/j.gsf.2018.09.008>
- Spencer, C. J., Kirkland, C. L., Roberts, N. M. W., Evans, N. J., & Liebmann, J. (2020). Strategies towards robust interpretations of in situ zircon Lu-Hf isotope analyses. *Geoscience Frontiers*, in press. <https://doi.org/10.1016/j.gsf.2019.09.004>
- Stearns, M. A., Hacker, B. R., Ratschbacher, L., Lee, J., Cottle, J. M., & Kylander-Clark, A. (2013). Synchronous Oligocene–Miocene metamorphism of the Pamir and the north Himalaya driven by plate-scale dynamics. *Geology*, 41(10), 1071–1074 <https://doi.org/10.1130/g34451.1>
- Streule, M. J., Searle, M. P., Waters, D. J., & Horstwood, M. S. A. (2010). Metamorphism, melting, and channel flow in the Greater Himalayan Sequence and Makalu leucogranite: Constraints from thermobarometry, metamorphic modeling, and U–Pb geochronology. *Tectonics*, 29(5), TC5011 <https://doi.org/10.1029/2009TC002533>
- Stübner, K., Grujic, D., Parrish, R. R., Roberts, N. M. W., Kronz, A., Wooden, J., & Ahmad, T. (2014). Monazite geochronology unravels the timing of crustal thickening in NW Himalaya. *Lithos*, 210–211, 111–128 <https://doi.org/10.1016/j.lithos.2014.09.024>
- Thiede, R. C., Arrowsmith, J. R. N., Bookhagen, B., McWilliams, M., Sobel, E. R., & Strecker, M. R. (2006). Dome formation and extension in the Tethyan Himalaya, Leo Pargil, Northwest India. *GSA Bulletin*, 118(5–6), 635–650 <https://doi.org/10.1130/B25872.1>
- Thöni, M., Miller, C., Hager, C., Grasemann, B., & Horschneegg, M. (2012). New geochronological constraints on the thermal and exhumation history of the lesser and higher Himalayan crystalline units in the Kullu–Kinnaur area of Himachal Pradesh (India). *Journal of Asian Earth Sciences*, 52, 98–116. <https://doi.org/10.1016/j.jseas.2012.02.015>
- Tripathi, K., Sen, K., & Dubey, A. K. (2012). Modification of fabric in pre-Himalayan granitic rocks by post-emplacment ductile deformation: Insights from microstructures, AMS, and U–Pb geochronology of the Paleozoic Kinnaur Kailash granite and associated Cenozoic leucogranites of the south Tibetan detachment zone, Himachal high Himalaya. *International Journal of Earth Sciences*, 101(3), 761–772 <https://doi.org/10.1007/s00531-011-0657-z>
- Vance, D., Ayres, M., Kelley, S., & Harris, N. (1998). The thermal response of a metamorphic belt to extension: Constraints from laser Ar data on metamorphic micas. *Earth and Planetary Science Letters*, 162(1), 153–164 [https://doi.org/10.1016/S0012-821X\(98\)00163-0](https://doi.org/10.1016/S0012-821X(98)00163-0)
- Vance, D., & Harris, N. (1999). Timing of prograde metamorphism in the Zaskar Himalaya. *Geology*, 27(5), 395–398 [https://doi.org/10.1130/0091-7613\(1999\)027<0395:topmit>2.3.co;2](https://doi.org/10.1130/0091-7613(1999)027<0395:topmit>2.3.co;2)
- Vannay, J.-C., Grasemann, B., Rahn, M., Frank, W., Carter, A., Baudraz, V., & Cosca, M. (2004). Miocene to Holocene exhumation of metamorphic crustal wedges in the NW Himalaya: Evidence for tectonic extrusion coupled to fluvial erosion. *Tectonics*, 23(1), TC1014 <https://doi.org/10.1029/2002TC001429>
- Vannay, J.-C., & Hodges, K. V. (1996). Tectonometamorphic evolution of the Himalayan metamorphic core between the Annapurna and Dhaulagiri, Central Nepal. *Journal of Metamorphic Geology*, 14(5), 635–656 <https://doi.org/10.1046/j.1525-1314.1996.00426.x>
- Viskopic, K., Hodges, K. V., & Bowring, S. A. (2005). Timescales of melt generation and the thermal evolution of the Himalayan metamorphic core, Everest region, eastern Nepal. *Contributions to Mineralogy and Petrology*, 149(1), 1–21 <https://doi.org/10.1007/s00410-004-0628-5>
- Walker, B. M., Martin, M. W., Bowring, S. A., Searle, M. P., Waters, D. J., & Hodges, K. V. (1999). Metamorphism, melting, and extension: Age constraints from the high Himalayan slab of southeast Zaskar and northwest Lahaul. *The Journal of Geology*, 107(4), 473–495 <https://doi.org/10.1086/314360>
- Walters, J. B., & Kohn, M. J. (2017). Protracted thrusting followed by late rapid cooling of the greater Himalayan sequence, Annapurna Himalaya, Central Nepal: Insights from titanite petrochronology. *Journal of Metamorphic Geology*, 35(8), 897–917 <https://doi.org/10.1111/jmg.12260>
- Wang, J.-M., Rubatto, D., & Zhang, J.-J. (2015). Timing of partial melting and cooling across the greater Himalayan crystalline complex (Nyalam, central Himalaya): In-sequence thrusting and its implications. *Journal of Petrology*, 56(9), 1677–1702 <https://doi.org/10.1093/petrology/egv050>
- Wang, J.-M., Wu, F.-Y., Rubatto, D., Liu, K., Zhang, J.-J., & Liu, X.-C. (2018). Early Miocene rapid exhumation in southern Tibet: Insights from P–T–t–D–magmatism path of Yardoi dome. *Lithos*, 304–307, 38–56 <https://doi.org/10.1016/j.lithos.2018.02.003>
- Wang, J.-M., Wu, F.-Y., Rubatto, D., Liu, S.-R., Zhang, J.-J., Liu, X.-C., & Yang, L. (2017). Monazite behaviour during isothermal decompression in pelitic granulites: A case study from Dinggye, Tibetan Himalaya. *Contributions to Mineralogy and Petrology*, 172, 81 <https://doi.org/10.1007/s00410-017-1400-y>
- Wang, J.-M., Zhang, J.-J., Liu, K., Zhang, B., Wang, X.-X., Rai, S., & Scheltens, M. (2016). Spatial and temporal evolution of tectonometamorphic discontinuities in the central Himalaya: Constraints from P–T paths and geochronology. *Tectonophysics*, 679, 41–60 <https://doi.org/10.1016/j.tecto.2016.04.035>
- Wang, J. M., Zhang, J. J., & Wang, X. X. (2013). Structural kinematics, metamorphic P–T profiles and zircon geochronology across the greater Himalayan crystalline complex in south-central Tibet: Implication for a revised channel flow. *Journal of Metamorphic Geology*, 31(6), 607–628 <https://doi.org/10.1111/jmg.12036>
- Wang, X. X., Zhang, J. J., Liu, J., Yan, S. Y., & Wang, J. M. (2013). Middle-Miocene transformation of tectonic regime in the Himalayan orogen. *Chinese Science Bulletin*, 58(1), 108–117 <https://doi.org/10.1007/s11434-012-5414-6>
- Wang, Y., Li, Q., & Qu, G. (2006). ⁴⁰Ar/³⁹Ar thermochronological constraints on the cooling and exhumation history of the south Tibetan detachment system, Nyalam area, southern Tibet. *Geological Society, London, Special Publications*, 268, 327–354 <https://doi.org/10.1144/GSL.SP.2006.268.01.16>
- Wang, Y., Zhang, L., Zhang, J., & Wei, C. (2017). The youngest eclogite in central Himalaya: P–T path, U–Pb zircon age and its tectonic implication. *Gondwana Research*, 41, 188–206. <https://doi.org/10.1016/j.gr.2015.10.013>
- Warren, C. J., Grujic, D., Kellett, D. A., Cottle, J., Jamieson, R. A., & Ghalley, K. S. (2011). Probing the depths of the India–Asia collision: U–Th–Pb monazite chronology of granulites from NW Bhutan. *Tectonics*, 30(2), TC2004 <https://doi.org/10.1029/2010TC002738>
- Waters, D. J. (2019). Metamorphic constraints on the tectonic evolution of the high Himalaya in Nepal: The art of the possible. *Geological Society, London, Special Publications*, 483, 325–375 <https://doi.org/10.1144/sp483-2018-187>
- Waters, D. J., Law, R. D., Searle, M. P., & Jessup, M. J. (2019). Structural and thermal evolution of the south Tibetan detachment shear zone in the Mt Everest region, from the 1933 sample collection of L. R. Wager.

- Geological Society, London, Special Publications*, 478, 335–372 <https://doi.org/10.1144/sp478.17>
- Webb, A. A. G. (2013). Preliminary balanced palinspastic reconstruction of Cenozoic deformation across the Himachal Himalaya (northwestern India). *Geosphere*, 9(3), 572–587 <https://doi.org/10.1130/GES00787.1>
- Webb, A. A. G., Guo, H., Clift, P. D., Husson, L., Müller, T., Costantino, D., ... Wang, Q. (2017). The Himalaya in 3D: Slab dynamics controlled mountain building and monsoon intensification. *Lithosphere*, 9(4), 637–651 <https://doi.org/10.1130/l636.1>
- Webb, A. A. G., Schmitt, A. K., He, D., & Weigand, E. L. (2011). Structural and geochronological evidence for the leading edge of the greater Himalayan crystalline complex in the Central Nepal Himalaya. *Earth and Planetary Science Letters*, 304(3–4), 483–495 <https://doi.org/10.1016/j.epsl.2011.02.024>
- Weinberg, R. F. (2016). Himalayan leucogranites and migmatites: Nature, timing and duration of anatexis. *Journal of Metamorphic Geology*, 34, 821–843 <https://doi.org/10.1111/jmg.12204>
- Wiesmayr, G., & Grasmann, B. (2002). Eohimalayan fold and thrust belt: Implications for the geodynamic evolution of the NW-Himalaya (India). *Tectonics*, 21(6), 8–1–8–18. <https://doi.org/10.1029/2002TC001363>
- Wu, C., Nelson, K. D., Wortman, G., Samson, S. D., Yue, Y., Li, J., ... Edwards, M. A. (1998). Yadong cross structure and south Tibetan detachment in the east central Himalaya (89°–90°E). *Tectonics*, 17(1), 28–45 <https://doi.org/10.1029/97TC03386>
- Xie, J., Qiu, H., Bai, X., Zhang, W., Wang, Q., & Xia, X. (2018). Geochronological and geochemical constraints on the Cuonadong leucogranite, eastern Himalaya. *Acta Geochimica*, 37(3), 347–359 <https://doi.org/10.1007/s11631-018-0273-8>
- Xie, L., Tao, X., Wang, R., Wu, F., Liu, C., Liu, X., ... Zhang, R. (2020). Highly fractionated leucogranites in the eastern Himalayan Cuonadong dome and related magmatic Be–Nb–Ta and hydrothermal Be–W–Sn mineralization. *Lithos*, in press., 105286. <https://doi.org/10.1016/j.lithos.2019.105286>
- Xie, Y. L., Li, L. M., Wang, B. G., Li, G. M., Liu, H. F., Li, Y. X., ... Zhou, J. J. (2017). Genesis of the Zhaxikang epithermal Pb–Zn–Sb deposit in southern Tibet, China: Evidence for a magmatic link. *Ore Geology Reviews*, 80, 891–909 <https://doi.org/10.1016/j.oregeorev.2016.08.007>
- Xu, Z. Q., Wang, Q., Pêcher, A., Liang, F. H., Qi, X. X., Cai, Z. H., ... Cao, H. (2013). Orogen-parallel ductile extension and extrusion of the greater Himalaya in the late Oligocene and Miocene. *Tectonics*, 32(2), 191–215 <https://doi.org/10.1002/tect.20021>
- Yan, D. P., Zhou, M. F., Robinson, P. T., Grujic, D., Malpas, J., Kennedy, A., & Reynolds, P. H. (2012). Constraining the mid-crustal channel flow beneath the Tibetan plateau: Data from the Nielaxiongbo gneiss dome, SE Tibet. *International Geology Review*, 54(6), 615–632 <https://doi.org/10.1080/00206814.2010.548153>
- Yang, L., Liu, X.-C., Wang, J.-M., & Wu, F.-Y. (2019). Is Himalayan leucogranite a product by in situ partial melting of the greater Himalayan crystalline? A comparative study of leucosome and leucogranite from Nyalam, southern Tibet. *Lithos*, 342–343, 542–556 <https://doi.org/10.1016/j.lithos.2019.06.007>
- Yang, X. Y., Zhang, J. J., Qi, G. W., Wang, D. C., Guo, L., Li, P. Y., & Liu, J. (2009). Structure and deformation around the Gyirong basin, north Himalaya, and onset of the south Tibetan detachment system. *Science in China Series D: Earth Sciences*, 52(8), 1046–1058 <https://doi.org/10.1007/s11430-009-0111-2>
- Yin, A., & Harrison, T. M. (2000). Geologic evolution of the Himalayan–Tibetan orogen. *Annual Review of Earth and Planetary Sciences*, 28(1), 211–280 <https://doi.org/10.1146/annurev.earth.28.1.211>
- Zeiger, K., Gordon, S., Long, S., Kylander-Clark, A., Agustsson, K., & Penfold, M. (2015). Timing and conditions of metamorphism and melt crystallization in greater Himalayan rocks, eastern and Central Bhutan: Insight from U–Pb zircon and monazite geochronology and trace-element analyses. *Contributions to Mineralogy and Petrology*, 169(5), 1–19 <https://doi.org/10.1007/s00410-015-1143-6>
- Zeng, L. S., Gao, L. E., Tang, S. H., Hou, K. J., Guo, C. L., & Hu, G. Y. (2015). Eocene magmatism in the Tethyan Himalaya, southern Tibet. *Geological Society, London, Special Publications*, 412, 287–316 <https://doi.org/10.1144/SP412.8>
- Zeng, L. S., Gao, L. E., Xie, K. J., & Jing, L. Z. (2011). Mid-Eocene high Sr/Y granites in the northern Himalayan gneiss domes: Melting thickened lower continental crust. *Earth and Planetary Science Letters*, 303(3–4), 251–266 <https://doi.org/10.1016/j.epsl.2011.01.005>
- Zeng, L. S., Liu, J., Gao, L. E., Xie, K. J., & Wen, L. (2009). Early Oligocene anatexis in the Yardoi gneiss dome, southern Tibet and geological implications. *Chinese Science Bulletin*, 54(1), 104–112 <https://doi.org/10.1007/s11434-008-0362-x>
- Zhang, H., Harris, N., Parrish, R., Kelley, S., Zhang, L., Rogers, N., ... King, J. (2004). Causes and consequences of protracted melting of the mid-crust exposed in the north Himalayan antiform. *Earth and Planetary Science Letters*, 228(1–2), 195–212 <https://doi.org/10.1016/j.epsl.2004.09.031>
- Zhang, H. F., Harris, N., Parrish, R., Zhang, L., & Zhao, Z. D. (2004). U–Pb ages of Kude and Sajia leucogranites in Sajia dome from north Himalaya and their geological implications. *Chinese Science Bulletin*, 49(19), 2087–2092 <https://doi.org/10.1360/04wd0198>
- Zhang, J., & Guo, L. (2007). Structure and geochronology of the southern Xainza-Dinggye rift and its relationship to the south Tibetan detachment system. *Journal of Asian Earth Sciences*, 29(5), 722–736 <https://doi.org/10.1016/j.jseae.2006.05.003>
- Zhang, J. J., Santosh, M., Wang, X. X., Guo, L., Yang, X. Y., & Zhang, B. (2012). Tectonics of the northern Himalaya since the India–Asia collision. *Gondwana Research*, 21, 939–960 <https://doi.org/10.1016/j.gr.2011.11.004>
- Zhang, L. K., Li, G. M., Santosh, M., Cao, H. W., Dong, S. L., Zhang, Z., ... Zhang, S. T. (2019). Cambrian magmatism in the Tethys Himalaya and implications for the evolution of the proto-Tethys along the northern Gondwana margin: A case study and overview. *Geological Journal*, 54(4), 2545–2565 <https://doi.org/10.1002/gj.3311>
- Zhang, L. K., Zhang, Z., Li, G. M., Dong, S. L., Xia, X. B., Liang, W., ... Cao, H. W. (2018). Rock assemblage, structural characteristics and genesis mechanism of the Cuonadong dome, Tethys Himalaya. *Earth Science*, 43(8), 2664–2683 (in Chinese with English Abstract).
- Zhang, Z., Li, G.M., Cao, H.W., Zhang, L.K., Huang, Y., Dong, S.L., ... Liu, Y. Q. (2020). Miocene potassic and adakitic intrusions in eastern Central Lhasa terrane, Tibet: Implications for origin and tectonic of postcollisional magmatism. *Geological Journal*, in press. <https://doi.org/10.1002/gj.3559>
- Zhao, X., Yang, Z., Hou, Z., Zhang, X., Li, Y., Pei, Y., ... Li, S. (2019). The structural deformation characteristics and the control of gold mineralization of the upper Triassic flysch (Langjiexue Group) in Tibetan Plateau. *Geological Journal*, 54(3), 1331–1342 <https://doi.org/10.1002/gj.3230>
- Zong, K., Klemd, R., Yuan, Y., He, Z., Guo, J., Shi, X., ... Zhang, Z. (2017). The assembly of Rodinia: The correlation of early Neoproterozoic (ca. 900Ma) high-grade metamorphism and continental arc formation in the southern Beishan Orogen, southern central Asian Orogenic Belt (CAOB). *Precambrian Research*, 290, 32–48 <https://doi.org/10.1016/j.precamres.2016.12.010>

SUPPORTING INFORMATION

Additional supporting information may be found online in the Supporting Information section at the end of this article.

How to cite this article: Zhang L-K, Li G-M, Cao H-W, et al. Activity of the south Tibetan detachment system: Constraints from leucogranite ages in the eastern Himalayas. *Geological Journal*. 2020;1–34. <https://doi.org/10.1002/gj.3756>